

Internal Report
DESY FCE-90-01
August 1990

Production of η , η' and $f_1(1285)$ -Mesons in Tagged and Untagged Two-Photon Reactions

von

J. H. Peters



DESY behält sich alle Rechte für den Fall der Schutzrechtserteilung und für die wirtschaftliche Verwertung der in diesem Bericht enthaltenen Informationen vor.

DESY reserves all rights for commercial use of information included in this report, especially in case of filing application for or grant of patents.

**“Die Verantwortung für den Inhalt dieses
Internen Berichtes liegt ausschließlich beim Verfasser”**

Production of η , η' and $f_1(1285)$ -Mesons
in Tagged and Untagged Two-Photon Reactions

Schick

Dissertation
zur Erlangung des Doktorgrades
des Fachbereichs Physik
der Universität Hamburg

Vorgelegt von:
Jan Hendrik Peters
aus Hamburg

Hamburg
1990

Kurzfassung

In dieser Arbeit wird die Produktion von η , η' und $f_1(1285)$ Resonanzen in Zwei-Photon-Reaktionen untersucht. Die zugrunde liegenden Daten wurden mit dem CELLO Detektor am $\epsilon^+\epsilon^-$ Speicherring PETRA bei DESY bei einer Strahlenergie von 17.5 GeV aufgenommen. Eine Datenmenge entsprechend einer integrierten Luminosität von 86 pb^{-1} stand für die Analyse zur Verfügung.

In den Daten ohne *tag* wird die Produktion von η' -Mesonen im Endzustand $\pi^+\pi^-\gamma$ beobachtet. Die radiative Breite des η' wird zu $\Gamma_{\gamma\gamma} = 3.62 \pm 0.15 \pm 0.47 \text{ keV}$ bestimmt. Eine Messung der Formfaktoren des η und η' wurde für mehrere Endzustände im *single tag mode* durchgeführt. Zum ersten Mal wurde die Q^2 -Abhängigkeit dieser Größe in der Reaktion $\gamma\gamma^* \rightarrow \eta' \rightarrow \eta\pi^+\pi^-$ mit $\eta \rightarrow \pi^+\pi^- (\gamma/\pi^0)$ bestimmt. Die Q^2 -Abhängigkeit der Formfaktoren läßt sich gut durch einen Polansatz mit Massen von $\Lambda_\eta = 839 \pm 63 \text{ MeV}$ bzw. $\Lambda_{\eta'} = 794 \pm 44 \text{ MeV}$ beschreiben. Die Kopplung des Spin-1-Mesons $f_1(1285)$ an zwei Photonen läßt sich nur in Reaktionen mit mindestens einem *tag* bestimmen. Die Kopplungsstärke $\tilde{\Gamma}$ ergibt sich im Endzustand $\eta\pi^+\pi^-$ dabei zu $\tilde{\Gamma} = 4.4 \pm 2.1 \pm 1.2 \text{ keV}$.

Abstract

In this thesis the formation of the η , η' and $f_1(1285)$ resonances in tagged and untagged two-photon reactions is studied. The data were taken with the CELLO detector at the PETRA $\epsilon^+\epsilon^-$ storage ring with a beam energy of 17.5 GeV corresponding to an integrated luminosity of 86 pb^{-1} .

In the untagged data the production of the η' -meson is observed in the $\pi^+\pi^-\gamma$ -final state. The radiative width of the η' is determined to be $\Gamma_{\gamma\gamma} = 3.62 \pm 0.15 \pm 0.47 \text{ keV}$. Form factor measurements for the η and η' are conducted in the single tag mode for various final states. For the first time the Q^2 -development of this quantity is studied in the reaction $\gamma\gamma^* \rightarrow \eta' \rightarrow \eta\pi^+\pi^-$ with $\eta \rightarrow \pi^+\pi^- (\gamma/\pi^0)$. The Q^2 -dependence of the form factor is well described by a pole ansatz with masses $\Lambda_\eta = 839 \pm 63 \text{ MeV}$ and $\Lambda_{\eta'} = 794 \pm 44 \text{ MeV}$ for the η and η' respectively. The coupling of the spin-1 meson $f_1(1285)$ to two photons can only be determined in a tagged reaction. The coupling strength $\tilde{\Gamma}$ is determined in the $\eta\pi^+\pi^-$ -final state to $\tilde{\Gamma} = 4.4 \pm 2.1 \pm 1.2 \text{ keV}$.

Contents

1	Introduction	7
2	The Physics of Two-Photon Reactions	10
2.1	Kinematics	10
2.2	The Exact Cross Section for the Two-Photon Process	12
2.3	Approximations and General Features	14
2.4	Creation of Single Resonances	15
2.4.1	Pseudoscalar Resonances	17
2.4.2	Axial Vector Resonances	18
2.4.3	Transition Form Factors	20
2.5	Description of the Decay $\eta' \rightarrow \rho\gamma$	21
3	The Experiment	23
3.1	The CELLO Detector	23
3.1.1	Overview	24
3.1.2	Central Track Detector	26
3.1.3	Lead Liquid Argon Calorimeter	28
3.1.4	Forward Calorimeter	30
3.2	Data Acquisition and Event Reconstruction	30
3.2.1	Trigger System	30
3.2.2	Data Acquisition	32
3.2.3	Filter	33
3.2.4	Event Reconstruction	34
3.2.5	Data Reduction	35
4	Monte Carlo Simulation	36
4.1	Event Simulation	36
4.1.1	Event Generation	36
4.1.2	Preselection Cuts	38
4.2	Detector Simulation	39
4.3	Trigger Simulation	40
4.4	Evaluation of the Radiative Width of Resonances	40
5	Event Selection and Improvements of the Reconstruction Software	42
5.1	Selection of $\pi^+\pi^-N\gamma$ events	42
5.2	Selection of $\pi^+\pi^-\pi^+\pi^-N\gamma$ events	45
5.3	Photon Selection Criteria	45
5.4	Recalibration of the Forward Calorimeter	46

6	Analysis of the Reaction $\gamma\gamma \rightarrow \eta' \rightarrow \rho\gamma$	48
6.1	Determination of the Radiative Width of the η'	48
6.2	The ρ -Mass Spectrum and Decay Angular Distribution	57
6.3	Discussion of the Results and Comparison to Other Experiments	57
7	η'-Form Factor Measurement	64
7.1	The Reaction $\gamma\gamma^* \rightarrow \eta' \rightarrow \rho\gamma$	64
7.2	The Reaction $\gamma\gamma^* \rightarrow \eta' \rightarrow \eta\pi^+\pi^-, \eta \rightarrow \gamma\gamma$	69
7.3	The Reaction $\gamma\gamma^* \rightarrow \eta' \rightarrow \eta\pi^+\pi^-, \eta \rightarrow \pi^+\pi^-(\pi^0/\gamma)$	72
7.4	Conclusions and Discussion	76
8	η-Form Factor Measurement	80
8.1	The Reaction $\gamma\gamma^* \rightarrow \eta \rightarrow \pi^+\pi^-\pi^0$	80
8.2	The $\pi^+\pi^-\gamma$ final state	82
8.3	Conclusions and Discussion	84
9	Coupling Strength of the Spin-1 Meson $f_1(1285)$	87
10	Summary	91
	References	93

List of Figures

2.1	Kinematics of the two-photon process	11
3.1	Sideview of the CELLO detector	25
3.2	Geometrical acceptance of the CELLO detector	26
3.3	Structure of the lead liquid argon calorimeter	29
3.4	$r\varphi$ -sectors for the trigger logic	31
5.1	$\cos\vartheta_{\pi\pi}$ -distribution between charged tracks.	43
5.2	Result of the recalibration on the φ -resolution of tags.	47
6.1	Invariant $\pi^+\pi^-\gamma$ -mass spectrum after SF correction	49
6.2	p_t^2 -spectrum after recalculation of the photon energy.	50
6.3	Invariant $\pi^+\pi^-$ -spectrum of events after SF-correction	50
6.4	Invariant $\pi^+\pi^-\gamma$ -mass spectrum	52
6.5	Photon energy spectrum after background subtraction	52
6.6	Effect of lower photon energy cut on the radiative width $\Gamma_{\gamma\gamma}$	53
6.7	Invariant $m(\pi^+\pi^-\gamma)$ -spectrum with $p_t^2 < 0.01\text{GeV}^2$	55
6.8	Dependence of the radiative width on the fit range	56
6.9	$ \cos\vartheta_\pi^* $ -distribution	58
6.10	ρ -shape	58
6.11	Ideogram with statistical errors	61
6.12	Ideogram with statistical and systematic errors added	62
6.13	Dependence of the numerical integration on ϑ	62
6.14	Dependence of the numerical integration on the beam energy	63
7.1	Q^2 -resolution of tagged events	65
7.2	Invariant $m(\pi\pi\gamma)$ -spectrum for tagged events	66
7.3	Photon energy spectrum for data and MC events in the ρ -band	66
7.4	Decay angle of the π in the ρ -helicity frame	67
7.5	Q^2 -evolution of the η' -form factor in $\eta' \rightarrow \rho\gamma$	68
7.6	Invariant $\gamma\gamma$ -mass	70
7.7	Invariant $\pi^+\pi^-\eta$ -mass spectrum	71
7.8	Correlation between invariant $\pi^+\pi^-\eta$ -mass and Q^2	72
7.9	Q^2 -evolution of the η' -form factor in $\eta' \rightarrow \eta\pi^+\pi^-$	73
7.10	Angle between tag and 4π -system	74
7.11	Invariant 4π -mass	74
7.12	Q^2 -evolution of the η' -form factor in $\eta' \rightarrow 4\pi(\pi^0/\gamma)$	75
7.13	Q^2 -evolution of the η' - γ transition form factor, all measured reactions combined	77
7.14	Comparison of η' - γ -transition form factors	78

8.1	Invariant $\pi^+\pi^-\pi^0$ -mass	81
8.2	Q^2 -evolution of the η -form factor in $\eta \rightarrow \pi^+\pi^-\pi^0$	82
8.3	Invariant $\pi^+\pi^-\gamma$ -mass spectrum	83
8.4	Q^2 -evolution of the η -form factor in the final state $\pi^+\pi^-\gamma$	84
8.5	Q^2 -evolution of the η - γ -transition form factor	85
8.6	Comparison of η - γ -transition form factors	86
9.1	Invariant $\pi^+\pi^-\eta$ -mass spectrum	88
9.2	Q^2 -distribution of $f_1(1285)$ -events	89

List of Tables

3.1	Geometrical and electrical parameters of the central tracking detector.	27
3.2	Technical data of the liquid argon calorimeters.	28
3.3	Trigger conditions	32
4.1	MC generated events on the four vector level	37
4.2	Generated and preselected numbers of events	39
5.1	Selection cuts for charged particles.	43
6.1	Compilation of published values for $\Gamma_{\gamma\gamma}(\eta')$	59
6.2	η' , η and π^0 branching ratios from the <i>Review of Particle Properties</i> , 1988 . .	60
7.1	Values of the form factor in 5 bins of Q^2	67
7.2	Values for the form factor in the restricted region of the forward calorimeter (50 – 85 mrad) for a photon energy above 200 MeV	68
7.3	Values of the form factor for the reaction $\eta' \rightarrow \pi^+ \pi^- \gamma \gamma$	71
7.4	Values of the form factor for the reaction $\eta' \rightarrow \pi^+ \pi^- \pi^+ \pi^- (\pi^0/\gamma)$	76
7.5	Combined values for the η' - γ -transition form factor	77
7.6	Overview over tagging parameters of various experiments	78
8.1	Values of the form factor for the reaction $\eta \rightarrow \pi^+ \pi^- \pi^0$	81
8.2	Values of the form factor for the reaction $\eta \rightarrow \pi^+ \pi^- \gamma$	83
8.3	Combined values for the η - γ -transition form factor	84

Chapter 1

Introduction

This thesis studies the formation of the pseudoscalar mesons η and η' and of the axial vector meson $f_1(1285)$ in a two-photon fusion process.

Classically, two photons do not interact with each other: in Maxwell's theory the total electromagnetic field is a linear superposition of the individual fields of the two waves in their overlapping region. Thus, two light rays can cross each other without changing their direction, frequency or polarisation. Only interference effects can be observed.

With the development of quantum field theories in the 1930's this picture has changed considerably. Heisenberg's uncertainty principle allows a photon to become, for a short time, a pair of virtual charged particles, which can then interact with the other photon. The scattering of light by light is thus a feasible process.

The cross section for the elastic scattering of two photons was first calculated by Euler and Kockel in 1935 [1]. However, the cross section for visible light was found to be extremely small and thus this reaction is experimentally inaccessible. Inelastic $\gamma\gamma$ -scattering, i.e. the production of massive particles in two-photon reactions, is another process predicted by quantum theory. To observe such a reaction much higher photon energies are needed than can be produced by ordinary light sources.

A suitable source of high energetic photons became only available when e^+e^- -colliders came into operation. Two-photon reactions occur at an e^+e^- -collider when the two leptons do not annihilate but rather scatter on each other. This process can be understood as the interaction of the two electromagnetic fields accompanying the leptons. Both, the electron and the positron, radiate off space-like virtual photons which then react with each other. This radiation is well understood in quantum electrodynamics, and thus the inelastic reaction of the two photons $\gamma\gamma \rightarrow X$ can be separated from the full process $e^+e^- \rightarrow e^+e^-\gamma\gamma \rightarrow e^+e^-X$.

The investigation of two-photon interactions is a relatively young field of experimental particle physics and today a flourishing one. Two-photon reactions have mainly been studied at the e^+e^- -colliders DORIS, PEP and PETRA. Far more than 100 experimental analyses have been published in the last 10 years and many review articles exist which cover the theoretical and experimental aspects of this field [2]. In the recent years the CELLO collaboration has taken an active part in this study with an increasing number of contributions to all aspects of hadron resonance production (for an overview see e.g. [3]).

The intentions for studying two-photon reactions are twofold. On the one hand virtual photons can be used as a high resolution probe to study for instance the internal structure of hadrons, on the other hand the photon itself can be studied more closely. One of the unsolved theoretical questions in this field is the coupling of photons to hadrons in the regime between the direct coupling to the charge of the hadron and the pointlike coupling to its constituents.

For neutral hadrons this question is even more striking. Empirical models like VDM (Vector Meson Dominance Model) exist which try to explain this coupling by a conversion of the photon to a vector meson which then hadronically interacts with the neutral hadron. These models predict a strong dependence of the coupling strength on the virtual mass of the probing photon. Its size and form can be measured in two-photon reactions for the case where one of the photons is almost real and the other is highly virtual (*single tag mode*). The virtual mass of the photon hereby is calculated from the measured scattering angles and energies of the outgoing leptons.

In this thesis the coupling strength of photons to the pseudoscalar mesons η and η' and to the axial vector meson $f_1(1285)$ is studied in the single tag mode. For the η' meson also the coupling to two almost real photons is determined.

The data were taken with the CELLO detector at the PETRA storage ring in 1986. With an integrated luminosity of 86 pb^{-1} various decay channels of these mesons have been observed and the coupling has been studied in each of them.

This thesis is organized as follows. In the next chapter the relevant formulas for the description of the two-photon process will be presented. General features of the reaction can then be derived from approximations of the exactly calculable QED part of the cross section. The formation of single resonances will be presented for pseudoscalar and axial vector mesons. Special sections are devoted to the description of electromagnetic form factors governing the transition from the photon to the produced meson (here the standard approach for a two-photon reaction will be compared to descriptions used in the time-like region) and to the decay of the η' into $\rho\gamma$ which does not proceed as a simple phase space decay.

The third chapter describes the detector with an emphasis on the inner track detector and the liquid argon calorimeter, those components which are extensively used in the analysis. This is followed by a description of the data acquisition and standard reconstruction chain.

The determination of the detector acceptance for the analysed reactions requires a detailed knowledge of the detector response. This is achieved by a Monte Carlo simulation of the physical processes in the interaction region and in the detector. The generation of Monte Carlo events and their way through the simulated detector is presented in chapter 4. Using the detector acceptance the coupling strength of resonances to the two photons can be calculated.

In chapter 5 the selection of the various final states which have been investigated for the production of single resonances is described. Here, the criteria for identifying energy clusters in the calorimeter with photons and the distinction from noise plays an important role in the selection of exclusive final states. The observation of resonances like η and η' produced in a two-photon reaction poses an experimental challenge in a detector which was optimized for high energy $\epsilon^+\epsilon^-$ annihilation reactions. The typical energy of photons is 200 MeV and below for the decay modes studied. Considerable effort had to be put into the correct understanding of detector effects and physical processes to lower the threshold for the detection of these photons. This way, the acceptance e.g. for the reaction $\eta' \rightarrow \rho\gamma$ had been increased by a factor of 2.3. A similar effort for low momentum tracks increased the statistics for events with four charged particles by 50%. For the determination of the transition form factors a precise determination of position and energy of the scattered leptons is essential. An improved calibration of the forward calorimeter to achieve this goal is presented at the end of the chapter.

The last four chapters present the analyses of the various processes studied. In chapter 6 the radiative width of the η' is determined in its decay into $\rho\gamma$. Various studies have been conducted to reduce and precisely determine the systematical errors present in such an

analysis. With the result obtained for the radiative width a new world average is calculated. Hereby, sizeable discrepancies in the available world data are uncovered. An attempt has been made to locate their sources and to point out a way to a consistent description of the data.

The development of the two-photon coupling of the η' with increasing values of the squared momentum transfer Q^2 of one of the photons is studied in chapter 7 in three different final states. Due to the limited acceptance of tagged reactions, previously existing data were not able to distinguish between different models describing the form factor development. The measurement of the form factor in the decay $\eta' \rightarrow \eta_{\rightarrow \pi^+ \pi^- (\gamma/\pi^0)} \pi^+ \pi^-$ constitutes the first observation of this channel in a tagged two-photon reaction. The combined result of all three measured final states is compared to data of other experiments and to model calculations and can rule out one of the simple form factor models.

Chapter 8 gives a similar analysis for the η -meson. The form factor for the η is determined in two different final states. Until the beginning of 1990 the only measurements of the η -form factor were performed in the time-like region in leptonic conversion decays. There, measurements of the slope of the form factor at $Q^2 = 0$ in the decay $\eta \rightarrow e^+ e^- \gamma$ gave inconclusive results and a different sign of the slope from the one found in the decay $\eta \rightarrow \mu^+ \mu^- \gamma$. Thus, a considerable interest exists in repeating this measurement in the space-like region where a much bigger Q^2 -range is accessible.

The last chapter describes the determination of the coupling strength $\tilde{\Gamma}$ of the spin-1 meson $f_1(1285)$ to two photons. This meson is observed in the same $\eta\pi\pi$ final state also studied for the form factor development of the η' . Since this meson can only be produced in a tagged reaction statistical and systematical errors of existing data are still quite large. The two published results on the coupling strength differ by a factor of 2 and more data from other experiments are needed.

A short summary of all the results can be found at the end of this thesis.

Chapter 2

The Physics of Two-Photon Reactions

At an e^+e^- collider there are two major types of reactions. The first is the *annihilation* of the electron and positron into one time-like virtual photon. The final state has negative C-parity. The cross section of this reaction is suppressed by the photon propagator $1/q^2 = 1/s$, where s is the square of the centre of mass energy of the two leptons. The second reaction is the so called *two-photon process*. Here both leptons radiate off space-like virtual photons which then in turn collide and create final states of positive C-parity. The spectrum of the photons emitted is bremsstrahlung-like and predominantly leads to small lepton scattering angles with respect to the beam axis and to low photon energies E_γ . The e^+e^- cross section for this process is not suppressed by photon propagators with increasing centre of mass energy s , but, although of higher order in α , rather dominates over the corresponding annihilation cross section at PETRA energies.

This chapter describes the physics of the two-photon process at an e^+e^- collider. The kinematics of the reaction will be introduced in the following sections. The exact formula connecting the e^+e^- cross section of the full process $e^+e^- \rightarrow e^+e^-X$ with the cross section of the subprocess $\gamma\gamma \rightarrow X$ will be given in section 2.2. Some qualitative features of the reaction are then derived from an approximation of the full formula. Following is a description of the creation of single resonances focusing on the production of pseudoscalar and axialvector mesons analysed in this thesis. Various approaches to the form factor, the deviation of the two-photon coupling of mesons from point-like behaviour, will be presented. The last section of this chapter describes the decay characteristics of the η' into $\rho\gamma$ which cannot be modelled as a simple phase space decay.

2.1 Kinematics

The kinematic variables of the two-photon reaction $e^+e^- \rightarrow e^+e^-X$ are shown in fig 2.1, all particles are described by four-vectors.¹ $p_1 = (E, \vec{p}_1)$ and $p_2 = (E, \vec{p}_2)$ are the four-momenta of the incoming electron and positron respectively, the outgoing leptons are described by the corresponding primed variables p'_1 and p'_2 . The four-vectors of the photons are denoted by $q_i = (E_{\gamma_i}, \vec{q}_i) = p_i - p'_i$.

If the lepton beams are unpolarized and the polarisation of the outgoing leptons is unobserved, there remain five observables in the laboratory system: the energies E'_1, E'_2 of the

¹The letters p, q, k denote the four-momenta p^μ, q^μ, k^μ with the components $p^\mu = (E, \vec{p})$. The metric is given by $g_{\mu\nu} = \begin{pmatrix} 1 & & & \\ & -1 & & \\ & & -1 & \\ & & & -1 \end{pmatrix}$, such that $p^2 = p_\mu p^\mu = p^\mu g_{\mu\nu} p^\nu = E^2 - \vec{p}^2 = m^2$.

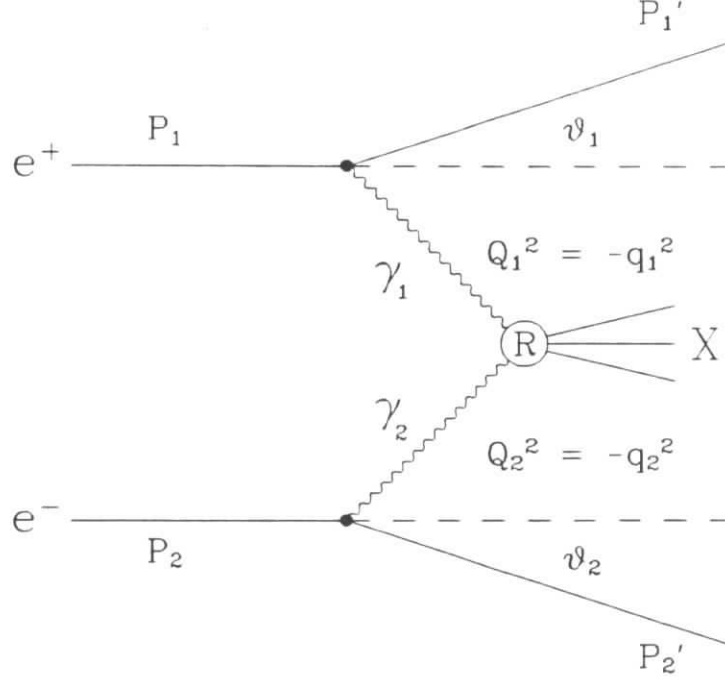


Figure 2.1: Kinematics of the two-photon process

scattered leptons, their scattering angles $\cos \vartheta_1$, $\cos \vartheta_2$ and the angle φ between the lepton scattering planes. From these various Lorentz scalars can be constructed.

The sum of the virtual photon momenta q_1 and q_2 yields the four-momentum k of the final system X . Its invariant mass W is given by $W_{\gamma\gamma}^2 := W^2 = k^2 = (q_1 + q_2)^2$:

$$\begin{aligned} W^2 &= \{(p_1 - p_1') + (p_2 - p_2')\}^2 \\ &= 4E - 4E(E_1' + E_2') + 2E_1'E_2' + 2m_\epsilon^2 - 2\vec{p}_1 \cdot \vec{p}_2' \end{aligned} \quad (2.1)$$

$$\approx 4E_{\gamma_1}E_{\gamma_2} - 2E_1'E_2'(1 - \cos \vartheta_1 \cos \vartheta_2 + \sin \vartheta_1 \sin \vartheta_2 \cos \varphi) \quad (2.2)$$

$$\approx 4E_{\gamma_1}E_{\gamma_2} - E_1'E_2'(\vartheta_1^2 + \vartheta_2^2 + 2\vartheta_1\vartheta_2 \cos \varphi) \quad (2.3)$$

The last term in the above equation can only be neglected when all polar angles are small, i.e. when both scattered leptons escape detection (*notag condition*). If the four-momentum of one or both leptons is measured (*tagging* the lepton) the reaction is said to be in the *single tag* or *double tag* mode. The kinematics of the reaction is totally determined in the double tag mode, however, as will be shown later this mode experimentally is the exception and thus, the kinematics of the process and the invariant mass of the final state have to be determined by measuring all final state particles.

The photons are space-like and, hence, the square of their four-momentum is negative (i.e. the mass of the photon $m_i = \sqrt{q_i^2}$ is imaginary) and it is common to define a positive quantity $Q^2 := -q^2$ with

$$Q_i^2 = 2EE_i'(1 - \sqrt{1 - m_\epsilon^2/E^2}\sqrt{1 - m_\epsilon^2/E_i'^2}\cos \vartheta_i) - 2m_\epsilon^2 \quad (2.4)$$

For large energies ($m_\epsilon^2 \ll E^2, E_i'^2$) this expression can be simplified to

$$Q_i^2 = 2EE_i'(1 - \cos \vartheta_i)(1 - \frac{m_\epsilon^2}{EE_i'}) + E_{\gamma_i}^2 \frac{m_\epsilon^2}{EE_i'} \cos \vartheta_i + \mathcal{O}(m_\epsilon^4) \quad (2.5)$$

which for all cases except $\cos \vartheta_i = 1$ yields

$$Q_i^2 = 2EE'_i(1 - \cos \vartheta_i). \quad (2.6)$$

For zero degree scattering energy and momentum conservation forbid the emittance of a real photon giving rise to a minimum Q^2 :

$$Q_{i\min}^2 = E_i^2 \frac{m_\epsilon^2}{EE'_i} \quad (2.7)$$

The minimum Q^2 for fixed centre of mass energy \sqrt{s} and fixed invariant mass W of the final state, both of them large in comparison to the lepton masses, is given by

$$Q_{\min}^2 = m_\epsilon^2 \frac{W^4}{s(s - W^2)} \quad (2.8)$$

To describe the two-photon process it is quite useful to divide the Feynman graph of the full reaction $e^+e^- \rightarrow e^+e^-X$ into two parts. The first one describes the radiation of the two virtual photons off the leptons. This part is a pure QED process and as such can be calculated exactly. The second part is the one of interest, describing the formation of a final state X by two virtual photons. For a fixed final state X the cross section can only depend on Lorentz invariant quantities. In the case of the formation by two *real* photons it only depends on the invariant $\gamma\gamma$ -mass W , for reactions at an e^+e^- collider it also depends on the virtuality Q_i^2 of the photons : $\sigma_{\gamma\gamma} = \sigma_{\gamma\gamma}(W^2, Q_1^2, Q_2^2)$. In the limit of $Q_1^2 \rightarrow 0$ and $Q_2^2 \rightarrow 0$ this formula describes the cross section for two real photons. (Note however, that due to the kinematics of the reaction, photons cannot reach the limiting case $Q_i^2 = 0$ but rather take the minimum value $Q_{i\min}^2$ as described by equation 2.7. For photons with very low Q^2 the term *quasi real* is used.)

2.2 The Exact Cross Section for the Two-Photon Process

Following the Feynman rules, the cross section for the full process can be written down immediately. The transition matrix element consists of electron and positron vertices $i(\pm e)\gamma_\mu$, two photon propagators $-ig^{\mu\nu}/q_i^2$ and the matrix element $T_{\alpha\beta}$ describing the formation of the final state X by two photons. Hence, the full amplitude can be written as

$$M = -e^2 \cdot \{\bar{u}(p'_1, s'_1)\gamma_\mu u(p_1, s_1)\} \frac{g^{\mu\alpha}}{q_1^2} T_{\alpha\beta} \frac{g^{\beta\nu}}{q_2^2} \{\bar{v}(p'_2, s'_2)\gamma_\nu v(p_2, s_2)\} \quad (2.9)$$

where the arguments of the spinors are the four-momenta p_i and spins s_i of the leptons. By introducing an unnormalized photon density flux

$$\rho_i^{\mu\nu} := -\frac{1}{q_i^2} \sum_{\text{spins}} \bar{u}(p'_i, s'_i)\gamma^\mu u(p_i, s_i)\bar{v}(p'_i, s'_i)\gamma^\nu v(p_i, s_i) \quad (2.10)$$

the cross section takes the form

$$\sigma = \frac{4\pi\alpha^2}{q_1^2 q_2^2} \rho_1^{\mu\mu'} \rho_1^{\nu\nu'} T_{\mu'\nu'}^* T_{\mu\nu} \frac{d\text{Lips}}{4\{(p_1 p_2)^2 - m_1^2 m_2^2\}^{1/2}} \cdot \frac{d^3 p'_1}{2E'_1(2\pi)^3} \cdot \frac{d^3 p'_2}{2E'_2(2\pi)^3} \quad (2.11)$$

where $d\text{Lips}$ is the Lorentz invariant phase space of the final state X

$$d\text{Lips} = (2\pi)^4 \delta^4(q_1 + q_2 - k) \prod_i \frac{d^3k_i}{2E_i(2\pi)^3}. \quad (2.12)$$

The summation $\rho_1^{\mu\mu'} \rho_1^{\nu\nu'} T_{\mu'\nu'}^* T_{\mu\nu}$ over the four indices (256 terms) can considerably be simplified by a transformation into the photon helicity frame. The transformation is defined by

$$M_{ab} = \epsilon_{1a}^\mu \epsilon_{2b}^\nu T_{\mu\nu} \quad (2.13)$$

The indices a and b take the values $+$, $-$ and 0 corresponding to the photon polarisation vectors $\epsilon_{i\pm}$ and ϵ_{i0} for transversely polarized photons (T) with helicity ± 1 and longitudinally polarized photons (L) with helicity 0 . A corresponding transformation is carried out for the photon flux factors $\rho_i^{\mu\nu}$. Integrating over the phase space of the final state X the resulting hadronic tensor

$$W_{a'b',ab} = \frac{1}{2} \int M_{a'b'}^* M_{ab} d\text{Lips} \quad (2.14)$$

can easily be interpreted in terms of the above transformation. Combining terms for helicity ± 1 the following equations define the $\gamma\gamma$ - cross sections and interference terms for photons which are in a definite polarisation state [7,6]:

$$\begin{aligned} W_{TT} &= \frac{1}{2}(W_{++,++} + W_{+,-,+}) = 2\sqrt{X}\sigma_{TT} \\ W_{TL} &= W_{+0,+0} = 2\sqrt{X}\sigma_{TL} \\ W_{LT} &= W_{0+,0+} = 2\sqrt{X}\sigma_{LT} \\ W_{LL} &= W_{00,00} = 2\sqrt{X}\sigma_{LL} \\ W_{TT}^\tau &= W_{+,-,-} = 2\sqrt{X}\tau_{TT} \\ W_{TL}^\tau &= \frac{1}{2}(W_{++,00} + W_{0+,-0}) = 2\sqrt{X}\tau_{TL} \\ W_{TT}^a &= \frac{1}{2}(W_{++,++} - W_{+,-,+}) = 2\sqrt{X}\tau_{TT}^a \\ W_{TL}^a &= \frac{1}{2}(W_{++,00} - W_{0+,-0}) = 2\sqrt{X}\tau_{TL}^a \end{aligned} \quad (2.15)$$

where X is the Møller flux factor $X = (q_1 q_2)^2 - q_1^2 q_2^2$. Using the above relations the cross section for the process $\epsilon^+ \epsilon^- \rightarrow \epsilon^+ \epsilon^- X$ can then be expressed in terms of two-photon cross sections σ_{ab} and interference terms τ_{ab} :

$$\begin{aligned} d\sigma_{\epsilon^+ \epsilon^- \rightarrow \epsilon^+ \epsilon^- X} &= \frac{\alpha^2}{16\pi^4 Q_1^2 Q_2^2} \cdot \left[\frac{(q_1 q_2)^2 - q_1^2 q_2^2}{(p_1 p_2)^2 - m_1^2 m_2^2} \right]^{1/2} \cdot \\ &\left\{ 4\rho_1^{++} \rho_2^{++} \cdot \sigma_{TT} + 2\rho_1^{++} \rho_2^{00} \cdot \sigma_{LT} + 2\rho_1^{00} \rho_2^{++} \cdot \sigma_{TL} + \rho_1^{00} \rho_2^{00} \cdot \sigma_{LL} \right. \\ &+ 2|\rho_1^{+-} \rho_2^{+-}| \cos 2\bar{\varphi} \cdot \tau_{TT} - 8|\rho_1^{+0} \rho_2^{+0}| \cos \bar{\varphi} \cdot \tau_{TL} + A \cdot \tau_{TT}^a + B \cdot \tau_{TL}^a \left. \right\} \cdot \\ &\frac{d^3p'_1}{E'_1} \cdot \frac{d^3p'_2}{E'_2} \end{aligned} \quad (2.16)$$

Here $\bar{\varphi}$ is the azimuthal angle between the lepton scattering plane in the $\gamma\gamma$ -centre of mass system. If this angle is not observed, the interference terms vanish due to the implicit integration over $\bar{\varphi}$. The parameters² A and B are nonzero only for the case of polarized leptons beams, and hence, at the PETRA storage ring the interference terms τ_{TT}^a and τ_{TL}^a

²The exact form of the photon flux factors ρ_i^{ab} and the parameters A and B can for instance be found in the review article by Budnev et al. [7].

do not contribute. Due to symmetry arguments only three cross sections σ_{TT} , σ_{LT} and σ_{LL} remain, since $\sigma_{LT}(Q_1^2, Q_2^2, W) = \sigma_{TL}(Q_2^2, Q_1^2, W)$. Depending on the four-momentum of the photons some or all of the above terms contribute to the cross section for a specific process. For the case of e.g. quasi real photons colliding, only the term σ_{TT} has to be taken into account.

2.3 Approximations and General Features

Some interesting limits can be derived³ from equation 2.16 which display some general features of two photon reactions. The most well-known approximation is the EPA (*Equivalent Photon Approximation*) which was derived by Weizsäcker and Williams already in 1934 [8]. It is based on a division of the reaction $e^+e^- \rightarrow e^+e^-X$ into a part describing the creation of two independent beams of transversely polarized photons and a part that describes the reaction $\gamma\gamma \rightarrow X$. The properties of the two photon beams are expressed by a luminosity function $\mathcal{L}_{\gamma\gamma}$ which is a product of two independent density functions dn for the photons, the two-photon reaction is characterized by its cross section $\sigma_{\gamma\gamma}$, such that the full e^+e^- -cross section reads

$$\sigma_{e^+e^- \rightarrow e^+e^-X} = \int \sigma_{\gamma\gamma}(\hat{s}) d\mathcal{L}(\hat{s}), \text{ with } d\mathcal{L} = dn_1 dn_2 \quad (2.17)$$

with \hat{s} being the scaled invariant $\gamma\gamma$ -mass of the final state $\hat{s} = W^2/s$, and s the square of the total e^+e^- centre of mass energy. These photon density functions dn show a bremsstrahlung like behaviour

$$dn \propto dQ^2/Q^2 dE_\gamma/E_\gamma \quad (2.18)$$

which consequently leads to a spectrum of predominantly low energetic photons with small invariant masses Q^2 . This at the same time translates by virtue of equation 2.6 into small lepton scattering angles. Since leptons with very small scattering angles (below 40 mrad at CELLO) escape detection in most detectors, the rate of tagged events is drastically reduced in comparison to the rate of untagged events. Typically the number of single tag events is one order of magnitude smaller than for untagged events, double tag events are another factor of ten more scarce.

By transforming the variables with the relation $W^2 = 4E_{\gamma 1}E_{\gamma 2}$ and integrating over the remaining, one yields in *leading log approximation* a luminosity function that is solely dependent on the invariant $\gamma\gamma$ -mass W of the final system

$$d\mathcal{L}(\hat{s}) = \left(\frac{2\alpha}{\pi}\right)^2 \ln^2\left(\frac{E}{m_e}\right) f(\hat{s}) \frac{d\hat{s}}{\hat{s}} \quad (2.19)$$

with

$$f(\hat{s}) = \left(1 + \frac{\hat{s}}{2}\right)^2 \ln \frac{1}{\hat{s}} - \frac{1}{2}(1 - \hat{s})(3 + \hat{s}) \quad (2.20)$$

The function f sometimes is called Low's function⁴. The functional dependence on \hat{s} for the luminosity function translates into a W dependence of the cross section for small invariant

³A derivation of the formulas used in this section can be found in some of the reviews (e.g. [4,5,7]) or can easily be calculated from the formulas given in these articles.

⁴Note, that the exact form of this function depends on the definition of the scaled invariant mass \hat{s} . Most of the functions published are identical to the one quoted here, but some authors, unfortunately, do not use these formulas in a consistent way.

$\gamma\gamma$ -masses of the following form:

$$\frac{d\sigma(W^*)}{dW} \propto \frac{1}{W} \ln \frac{s}{W^2} \sigma_{\gamma\gamma}(W^*) \quad (2.21)$$

which shows the dominance of final states with small invariant masses to the cross section. Systems with small invariant masses always have low particle multiplicities, which thus is a pronounced feature of two-photon reactions.

Another feature is the boost of the final state particles in the laboratory frame. Due to the possible big difference in momentum of the photons, the final state is not created at rest but rather has a strong momentum component along the beam axis. Together with the small transfer of transverse momentum by two quasi real photons colliding, the final state particles are concentrated around the beam axis. This effect of small production angles is enhanced by the strong forward scattering amplitude in the $\gamma\gamma$ -cross section for many reactions.

2.4 Creation of Single Resonances

Final states of low multiplicity can be formed in different ways in two-photon reactions, like phase space creation of the final state particles, pair creation of leptons, mesons or baryons, or the formation can proceed via the production and decay of a single resonance. This latter case will be described in more detail in this section. The $\gamma\gamma$ -coupling of a single resonance is essentially determined by its spin J and parity P . If this resonance is formed in a two-photon reaction its C -parity has to be $+1$, since it is created by a pair of identical particles (the photons themselves have a negative C -parity). Further restrictions follow from general principles and a set of rules known as Yang's theorems [9]. They e.g. do not allow the creation of a spin-1 resonance by two real photons. A complete set of matrix elements, form factors and $\gamma\gamma$ -cross sections for all J^{PC} combinations can be found in the review article by Poppe [6] from which most of the equations in this section have been taken.

The hadronic tensor for production and decay of a resonance R is

$$W_{abab} = \frac{1}{2} \int \left| \frac{M_{ab}(\gamma\gamma \rightarrow R) \delta_{a-b}^{Jz} D^{Jz}(R \rightarrow X)}{W^2 - m_R^2 + im_R \Gamma_R} \right|^2 d\text{Lips}(X) \quad (2.22)$$

where m_R and Γ_R are the mass and width of the resonance, M_{ab} the production amplitude and D^{Jz} the decay amplitude for the decay of the resonance R into the final state X . The size of the decay amplitude is connected to the decay width of the resonance by the *Golden Rule*:

$$\Gamma_R(W) B(R \rightarrow X) = \frac{1}{2m_R} \int |D^{Jz}|^2 d\text{Lips}(X) \quad (2.23)$$

and hence

$$W_{abab} = \frac{1}{2} |M_{ab}|^2 \frac{2m_R \Gamma_R(W) B(R \rightarrow X)}{(W^2 - m_R^2)^2 + m_R^2 \Gamma_R^2} \quad (2.24)$$

The resonance width Γ_R can be taken as constant for narrow resonances (i.e. $\Gamma_R \ll m_R$). If the width however is large (say above 50 MeV), the (with W) increasing phase space available for the decay and dynamical effects have to be taken into account. Since none of the analysed resonances has a sizeable width, the decay width Γ_R will be taken as constant in the following⁵.

⁵A discussion of the W dependence of the decay width can be found in references [6,11,12,13].

In the limit of $Q_1^2 = Q_2^2 = 0$, the formation of a resonance by two real photon is the inverse process of the radiative decay of the resonance. Therefore, the production cross section is a measure for the radiative decay width of the resonance. For a specific polarisation state J_Z of the resonance it reads:

$$\Gamma_{\gamma\gamma}^{J_Z} = \frac{1}{2m_R} \int \sum_{a,b} |M_{ab}|^2 \delta_{a-b}^{J_Z} d\text{Lips} \quad (2.25)$$

Since the final state can only consist of two real photons the summation over the photon polarisation states a and b is only to be taken over the transverse helicity states $+$ and $-$. The phase space element has only half its usual value due to the indistinguishable nature of the two bosons:

$$d\text{Lips}(\gamma\gamma) = \frac{1}{64\pi^2} d\Omega. \quad (2.26)$$

By averaging over the possible polarisation states of the resonance and integrating over the phase space of the photons the total radiative decay width is obtained:

$$\begin{aligned} \Gamma_{\gamma\gamma} &= \frac{1}{2J+1} \sum_{J_Z} \Gamma_{\gamma\gamma}^{J_Z} \\ &= \frac{1}{2J+1} \frac{1}{2m_R} \int \sum_{J_Z} |M_{ab}|^2 d\text{Lips} \\ &= \frac{1}{32\pi(2J+1)m_R} \sum_{a,b=+,-} |M_{ab}|^2 \delta_{a-b}^{J_Z} \end{aligned} \quad (2.27)$$

The above formulas all describe the coupling of two *real* photons to a meson. As already mentioned two *real* photons can not couple to a spin 1 state. This is no longer true if one of the photon is highly *virtual*. In the following we consider the single tag case where one of the photons (say photon number 1) is highly virtual (denoted by the symbol γ^* in the following) and the corresponding lepton is tagged in the detector. The virtuality of the other photon (denoted by γ) is kept small by requiring the second lepton not to be detected. Although the reverse process, the decay of a resonance into one real and one virtual photon, does not occur in nature, it is quite useful to introduce a coupling strength $\Gamma_{\gamma\gamma^*}$ analogous to the radiative decay width in equation 2.25. This allows us to write the cross section formulas in the same fashion as for regular $J = 0$ or $J = 2$ resonances. The creation of a spin 1 resonance proceeds either via the collision of two transverse photons (TT) or one longitudinal and one transverse photon (LT). For abbreviation the polarisation components $J_Z = \pm 1$ will be combined to $\Gamma_{\gamma\gamma^*}^{LT}$, the $J_Z = 0$ component will be denoted by $\Gamma_{\gamma\gamma^*}^{TT}$. Following Cahn [14] the full phase space for the two photons will be taken since they are no longer indistinguishable as in the previous case. The partial widths $\Gamma_{\gamma\gamma^*}^{LT}$ and $\Gamma_{\gamma\gamma^*}^{TT}$ then read:

$$\Gamma_{\gamma\gamma^*}^{TT}(Q^2) = \frac{1}{8\pi(2J+1)m_R} \frac{k^*}{W} (|M_{++}|^2 + |M_{--}|^2) \quad (2.28)$$

$$\Gamma_{\gamma\gamma^*}^{LT}(Q^2) = \frac{1}{8\pi(2J+1)m_R} \frac{k^*}{W} (|M_{0+}|^2 + |M_{0-}|^2) \quad (2.29)$$

where k^* is the momentum of the photons in the centre of mass system of the resonance. The sum $\Gamma_{\gamma\gamma^*} = \Gamma_{\gamma\gamma^*}^{LT} + \Gamma_{\gamma\gamma^*}^{TT}$ in the following will often be called a radiative width, although, literally taken it is not a physical decay width. Rather it will vanish in the limit $Q^2 \rightarrow 0$. The Q^2 dependence of these quantities will be discussed in the next but one section.

2.4.1 Pseudoscalar Resonances

For the production of pseudoscalar resonances ($J^{PC} = 0^{-+}$ like π^0 , η , η' , etc.) the amplitudes in the helicity base are [6]:

$$\begin{aligned} M_{-+} &= \sqrt{X} \cdot F_{TT0}(Q_1^2, Q_2^2) \\ M_{--} &= -M_{++} \\ M_{ab} &= 0 \quad \text{for all other helicity combinations} \end{aligned} \quad (2.30)$$

Thus, the coupling is described by a single form factor F_{TT0} for two transverse photons polarized in the same direction. All other helicity combinations cannot create a state with $J^P = 0^-$.

With equation 2.24 we now have:

$$\begin{aligned} W_{++++} &= F_{TT0}^2(Q_1^2, Q_2^2) \cdot X \cdot \frac{m_R \Gamma_R}{(W^2 - m_R^2)^2 + m_R^2 \Gamma_R^2} \\ W_{++--} &= -W_{++++} \\ W_{ab,cd} &= 0 \quad \text{for all other } ab, cd \text{ combinations} \end{aligned} \quad (2.31)$$

and for the cross sections:

$$\begin{aligned} \sigma_{TT} &= \frac{1}{4} F_{TT0}^2 \cdot \sqrt{X} \cdot \frac{m_R \Gamma_R}{(W^2 - m_R^2)^2 + m_R^2 \Gamma_R^2} \\ \tau_{TT} &= -2\sigma_{TT} \\ \sigma_{ab}, \tau_{ab} &= 0 \quad \text{for all other } ab \text{ combinations} \end{aligned} \quad (2.32)$$

Since in the analysis of single tag and notag events an implicit integration over the angle $\tilde{\varphi}$ between the lepton scattering planes is unavoidable, the contribution from the interference term τ_{TT} vanishes in the total cross section of this process (cf. equation 2.16)

$$d\sigma_{e^+\epsilon^- \rightarrow e^+\epsilon^- X} = \frac{\alpha^2}{32\pi^2 E_{beam}^2} \frac{\sqrt{X}}{Q_1^2 Q_2^2} 4\rho_1^{++} \rho_2^{++} \sigma_{TT} \frac{d^3 p'_1}{E'_1} \frac{d^3 p'_2}{E'_2} \quad (2.33)$$

The photon density matrices have the form [7]

$$\rho_1^{++} = \frac{(2p_1 q_2 - q_1 q_2)^2}{2X} + \frac{1}{2} + \frac{2m_\epsilon}{q_1^2} \quad (2.34)$$

$$\rho_2^{++} = \frac{(2p_2 q_1 - q_1 q_2)^2}{2X} + \frac{1}{2} + \frac{2m_\epsilon}{q_2^2} \quad (2.35)$$

The radiative width of a pseudoscalar resonance is given by equation 2.27

$$\Gamma_{\gamma\gamma}(W) = \frac{W^4}{64\pi m_R} F_{TT0}^2(0, 0) \quad (2.36)$$

The W -dependence of the radiative width is normally neglected, since $\Gamma_R \ll m_R$ for most pseudoscalar resonances. Instead, W is approximated by m_R , which leads to

$$\Gamma_{\gamma\gamma} = \frac{m_R^3}{64\pi} F_{TT0}^2(0, 0) \quad (2.37)$$

This last equation can be viewed upon as the definition of the nominal radiative width of the resonance, the W dependent width $\Gamma_{\gamma\gamma}(W)$ then is

$$\Gamma_{\gamma\gamma}(W) = \frac{W^4}{m_R^4} \Gamma_{\gamma\gamma} \quad (2.38)$$

For the measurement of the Q^2 -dependence of the cross section it is quite useful to divide the form factor into one part that contains the Q^2 -dependence and is equal to 1 for $Q_1^2 = Q_2^2 = 0$, and another part that describes the normalization. With the above formulae the form factor can then be written as

$$F_{TT0}^2(Q_1^2, Q_2^2) = F_{TT0}^2(0, 0) \cdot f^2(Q_1^2, Q_2^2) = \frac{64\pi\Gamma_{\gamma\gamma}}{m_R^3} \cdot f^2(Q_1^2, Q_2^2) \quad (2.39)$$

The term $f(Q_1^2, Q_2^2)$ is not known from first principles but rather has to be taken from models or from measurements (see below for a discussion about form factors). The cross section expressed in terms of form factors and radiative widths for the reaction $\epsilon^+\epsilon^- \rightarrow \epsilon^+\epsilon^- R$, $R =$ pseudoscalar resonance, is given by

$$d\sigma_{\epsilon^+\epsilon^- \rightarrow \epsilon^+\epsilon^- X} = \frac{2\alpha^2}{\pi^3 E_{beam}^2} \frac{X}{Q_1^2 Q_2^2 m_R^2} f^2(Q_1^2, Q_2^2) \rho_1^{++} \rho_2^{++} \frac{\Gamma_R \Gamma_{\gamma\gamma} B(R \rightarrow X)}{(W^2 - m_R^2)^2 + m_R^2 \Gamma_R^2} \frac{d^3 p_1'}{E_1'} \frac{d^3 p_2'}{E_2'} \quad (2.40)$$

2.4.2 Axial Vector Resonances

Axial vector states ($J^{PC} = 1^{++}$) like the $f_1(1285)$ and $f_1(1420)$ (previously called D(1285) and E(1420)) due to Yang's theorem can only be created if at least one of the photons is highly virtual. A necessary criterion for their identification is an observation of a signal in the single tag or double tag mode and at the same time the absence of the signal in the untagged case ($Q^2 \rightarrow 0$). In the following again the assumption is made that the final state is observed in the single tag mode and as before we assign photon 1 to be the highly virtual one. Then the production amplitudes in the helicity frame are [6]:

$$\begin{aligned} M_{++} &= -\frac{(q_2^2 - q_1^2)}{W} \cdot F_{TT0}(Q_1^2, Q_2^2) \\ M_{0+} &= \frac{\sqrt{-q_1^2}}{q_1 \cdot q_2} \sqrt{X} \cdot F_{LTeff}(Q_1^2, Q_2^2) \\ M_{--} &= -M_{++} \\ M_{0-} &= -M_{0+} \\ M_{ab} &= 0 \text{ for all other helicity combinations} \end{aligned} \quad (2.41)$$

The coupling thus is characterized by two different form factors. F_{TT0} describes the coupling of two transversely polarized photons to a spin-1-state, orientated perpendicular to the $\gamma\gamma$ -axis. The effective form factor $F_{LTeff} = F_{LT} + (Q_2^2 - Q_1^2)F'_{LT}$ describes the coupling of one longitudinal and one transverse photon to $J_z = \pm 1$.

The corresponding cross sections vanish for low Q^2 with $\sigma_{TT} \propto Q_1^4$ and $\sigma_{LT} \propto Q_1^2$. Thus, a dominance of σ_{LT} over σ_{TT} at low Q^2 is expected. The cross sections expressed in terms of these form factors read:

$$\begin{aligned} \sigma_{TT} &= \frac{1}{4\sqrt{X}} \frac{m_R \Gamma_R}{(W^2 - m_R^2)^2 + m_R^2 \Gamma_R^2} \cdot \frac{(q_1^2 - q_2^2)^2}{W^2} F_{TT0}^2(Q_1^2, Q_2^2) \\ \sigma_{LT} &= \frac{\sqrt{X}}{2} \frac{m_R \Gamma_R}{(W^2 - m_R^2)^2 + m_R^2 \Gamma_R^2} \cdot \frac{-q_1^2}{(q_1 q_2)^2} F_{LTeff}^2(Q_1^2, Q_2^2) \end{aligned} \quad (2.42)$$

As in the case of the pseudoscalar mesons the form factors are not known from first principles but have to be determined experimentally. A direct measurement, however, is not possible in this case, since the total cross section is sensitive only to the sum of both parts. In principle a separation of both parts is possible due to the different spin orientation J_z in both processes by analysing decay angular distributions. Due to the small number of events expected in single tag experiments, the result of such an analysis will, however, have huge statistical errors.

The cross section, alternatively, can be expressed in terms of the coupling strength $\Gamma_{\gamma\gamma^*}$ defined at the beginning of this section (cf. eqs. 2.28). Again it would be useful to split up the form factor into a part for $Q^2 = 0$ giving the normalization and into another part describing the Q^2 -development. Unlike the case of pseudoscalar resonances, here the coupling constants $\Gamma_{\gamma\gamma^*}$ are 0 for $Q^2 = 0$. Following Renard [16] a Q^2 -independent strength $\bar{\Gamma}$ can be defined exploiting the known Q^2 -dependence of the form factors (cf. eq. 2.41)

$$\lim_{Q_1^2 \rightarrow 0} \frac{m_R^2}{Q_1^2} \cdot \Gamma_{\gamma\gamma^*}(Q_1^2) = \bar{\Gamma} \quad (2.43)$$

Since the region of very low Q^2 cannot be accessed by most detectors (CELLO $Q_{min}^2 \approx 0.3 GeV^2$) and furthermore since the relative strength of F_{TT0} to F_{LTeff} is not known, a model is needed to describe this relative strength and the Q^2 -evolution of the form factors. Such a model for axial vector mesons has been developed by Cahn [15] in the framework of the non-relativistic quark model. The result is valid for $Q_2^2 \approx 0$ and small Q_1^2 and yields the following expressions:

$$\begin{aligned} F_{TT0}^2 &= 32\pi(2J+1) \frac{X}{m_R^5} f^2(Q_1^2, 0) \bar{\Gamma} \\ F_{LTeff}^2 &= 32\pi(2J+1) \frac{(q_1 q_2)^2}{m_R^5} f^2(Q_1^2, 0) \bar{\Gamma} \end{aligned} \quad (2.44)$$

where $f(Q_1^2, 0)$ again is a vector meson form factor. The two expressions have the same Q^2 -development and are nearly identical, since $X \approx (q_1 q_2)^2$ for $Q_2^2 \approx 0$. The calculations by Cahn are based on the assumption of a narrow resonance and explicitly use $W = m_R$, which is certainly a good approximation for a resonance like the $f_1(1285)$ which has a total width of 25 MeV, considering all other theoretical uncertainties and the statistical precision that can be achieved. Using the above formulae, the coupling strengths of a spin 1 resonance can be reduced to a single number $\bar{\Gamma}$ which still has to be determined by experiment:

$$\begin{aligned} \Gamma_{\gamma\gamma^*}^{TT}(Q^2) &= \frac{8X^{3/2}}{m_R^6} \frac{Q_1^4}{m_R^4} f^2(Q_1^2, 0) \bar{\Gamma} \\ \Gamma_{\gamma\gamma^*}^{LT}(Q^2) &= \frac{8X^{3/2}}{m_R^6} \frac{Q_1^2}{m_R^2} f^2(Q_1^2, 0) \bar{\Gamma} \end{aligned} \quad (2.45)$$

The definitions presented here follow the suggestion of Cahn [14,15] and are used by the MarkII and CELLO collaborations in their analysis of the $f_1(1420)$ resonance. The definition used by TPC/2 γ and JADE differ by a factor $4\sqrt{X}/m_R^2$, the cross section in both cases are however defined in the same way (see references [18]).

The cross sections then are :

$$\sigma_{TT} = 24\pi \frac{\sqrt{X}}{W^2} \frac{\Gamma_R}{(W^2 - m_R^2)^2 + m_R^2 \Gamma_R^2} \frac{(q_1^2 - q_2^2)^2}{W^4} f^2(Q_1^2, 0) \bar{\Gamma} \quad (2.46)$$

$$\sigma_{LT} = 48\pi \frac{\sqrt{X}}{W^2} \frac{\Gamma_R}{(W^2 - m_R^2)^2 + m_R^2 \Gamma_R^2} \frac{Q_1^2}{W^2} f^2(Q_1^2, 0) \hat{\Gamma} \quad (2.47)$$

2.4.3 Transition Form Factors

The form factors introduced in the cross section formulae for the pseudoscalar and axial vector meson resonances describe the deviation from the point like cross section for increasing values of the squared momentum transfer q^2 :

$$\frac{d\sigma}{dq^2} = \left. \frac{d\sigma}{dq^2} \right|_{point} \cdot f^2(q^2) \quad (2.48)$$

Classically, the electromagnetic structure of charged hadrons is probed by particles which scatter with different impact parameters on the hadron under study. Large (small) impact parameters hereby correspond to small (large) momentum transfers q . Assuming a uniformly distributed charge within a sphere of radius a , the form factor is determined to be [19]

$$f(q^2) = 1 - \frac{1}{6} a^2 q^2 \quad (2.49)$$

for low momentum transfers. The slope of the form factor $b = df(q^2)/dq^2|_{q^2=0}$ determined at zero momentum transfer is thus a measure for the charge radius of the object: $b = -\frac{1}{6}a^2$.

This concept can be transferred to neutral hadrons where the slope b is not a measure for charge radius of the hadron but rather the size of the interaction region with the probing particle. For large values of the four momentum transferred usually a pole form for the form factor formula is taken rather than the linear form presented above:

$$f(q^2) = \frac{1}{1 - q^2/m^2 - i\Gamma/m} \quad (2.50)$$

Here the parameter m denotes the mass of the pole and Γ its width. While in the time-like region ($q^2 > 0$) the width of the pole has to be taken into account it can be dropped in the space-like region ($q^2 < 0$). Assuming a ρ -pole (see discussion below) the maximum influence of the width-term is only of the order of 4%. Moreover, an energy dependent width $\Gamma(m_{\pi\pi})$ would be 0 or even imaginary outside the physical region.

A measurement of the pole behaviour in the time-like region is obtained from the analysis of leptonic conversion decays of neutral mesons. For the pseudoscalar resonances η and η' the decay into $\mu^+\mu^-\gamma$ has been studied (see [19] for a review on this subject). Here, the resonances decay into one real and one virtual photon which internally converts into a pair of leptons. The invariant mass of this lepton pair is identical to the mass q^2 of the virtual photon. The form factor determined from this reaction shows the characteristics of a ρ -Breit-Wigner. While for the η -decay the ρ -pole can never be reached it can in principle be observed in η' -decays.

The space-like region is accessible in two-photon reactions studied in this thesis. The amplitude of the reaction $T_{\mu\nu} = i\epsilon_{\mu\nu\alpha\beta} \cdot q_1^\alpha \cdot q_2^\beta \cdot F(Q_1^2, Q_2^2)$ contains a form factor F which is a function of the four-momenta squared of both photons $Q_i^2 = -q_i^2$. Usually it is assumed that F factorizes into $F(Q_1^2) \cdot F(Q_2^2)$, which is certainly a good approximation if only one of the photon four-momenta deviates substantially from zero. In such a single tag reaction the mesons are formed by one quasi real and one highly virtual photon. The form factor shows a

fall-off with increasing $|q^2| = Q^2$ which should be the continuation of the pole curve observed in the time-like region.

Various models exist which explain this pole behaviour. In vector meson dominance models (VDM) [20] the mass of the pole is the mass of a vector meson having the same quantum numbers as the photon and the form factor f takes the form:

$$f(Q_1^2, Q_2^2) = \frac{1}{(1 + Q_1^2/m_V^2)(1 + Q_2^2/m_V^2)} \quad (2.51)$$

An illustrative interpretation of the VDM ansatz is that the photons convert into virtual vector-mesons before they interact with each other. Usually a simple ρ -pole is taken as a form factor and $m_V = m_\rho$. If one considers mesons with a strong u and d -quark content, the ρ -assignment is obvious. If, however, the mesons created in a two-photon reaction are primarily composed of s -quarks, a ϕ -assignment might be more appropriate. Depending on the actual quark contents of the mesons combinations of these assignments are possible. For the leptonic conversion decays definite predictions exist for the slopes of the form factors in the reactions $\eta \rightarrow \mu^+ \mu^- \gamma$, $\eta' \rightarrow \mu^+ \mu^- \gamma$ (see ref.[61] in [19]). These can be translated into predictions for the pole masses of $m(\eta) = 734$ MeV and $m(\eta') = 820$ MeV.

A totally different approach leads to a similar behaviour for the form factor. Brodsky and Lepage [21] have performed a leading-order QCD calculation which interpolates between the $Q^2 = 0$ and $Q^2 = \infty$ limits using a monopole form. For the single tag reaction $\gamma\gamma^* \rightarrow \pi^0$ they get⁶:

$$f(Q_1^2, 0) = \frac{1}{1 + Q_1^2/4\pi^2 f_\pi^2} \quad (2.52)$$

which is equivalent to formula 2.51, when the mass m_V is identified with $2\pi f_\pi$. Assuming that the decay constants of all pseudoscalar particles are about equal ($f_\pi = 131.69$ MeV [17]), a mass dependence of $m_V = 827$ MeV, somewhat between a ρ and ϕ -form factor, is expected. If the pseudoscalar mesons have different decay constants the pole masses will take other values.

All the above approaches try to describe the same behaviour but use a different language for it. However, the descriptions in terms of pole masses, decay constants, slopes or interaction region radii are all equivalent to each other.

2.5 Description of the Decay $\eta' \rightarrow \rho\gamma$

The decay of a pseudoscalar resonance P into three other pseudoscalar resonances P_1, P_2, P_3 , e.g. $\eta' \rightarrow \eta\pi\pi$ or $\eta \rightarrow \pi\pi\pi$, may be described by a three-body phase space model (see [17]). The decay matrix element is constant, the decay angular distributions are flat and the partial decay rate $d\Gamma/dm_{12}$ is just proportional to $p_1^* \cdot k_3^*$, where p_1^* is the momentum of particle 1 in the m_{12} -rest frame, and k_3^* the momentum of particle 3 in the rest frame of the decaying resonance. Deviations from the phase space model have been measured. The slope of the Dalitz plot for $\eta' \rightarrow \eta\pi\pi$ of -0.06 [17] is however small and can be neglected.

The description of the electromagnetic decay into $\pi^+\pi^-\gamma$ is not as simple as in the above case. Due to the conservation of C -parity in the decay, the positive G -parity of the two-pion system and Bose symmetry, the $\pi\pi$ -system recoiling against the photon is essentially

⁶N.B. In the quoted article like in many other theoretical papers $f_P/\sqrt{2}$ is denoted f_P and called the pseudoscalar decay constant. Here the notation from the particle data group (*Note on Decay Constants of Pseudoscalar Mesons* [17], page 165) is adopted.

restricted to be in a $I^G(J^{PC}) = 1^+(1^{--})$ state [22]. Due to Watson's Theorem [23] this $\pi\pi$ -system is a ρ in the accessible energy range. The matrix element for such a decay into two vector particles is proportional to k^* , the momentum of the ρ or γ in the rest frame of the decaying resonance. Since the photon is massless the helicity of the ρ is restricted to ± 1 . The decay angular distribution of the pions in the ρ -rest frame relative to the photon therefore follows a $\sin^2 \vartheta$ distribution. The phase space decay is further modified by the intermediate ρ -pole, taking into account the correct value for the width $\Gamma(\pi\pi)$ for those $\pi\pi$ -pairs deviating from the nominal ρ -mass [24]

$$\Gamma(\pi\pi) = \Gamma_\rho \cdot p_\pi^3 \frac{2}{p_0(p_0^2 + p_\pi^2)} \quad (2.53)$$

where p_0 is the pion momentum for $m_{\pi\pi} = m_\rho$. The partial decay rate for the magnetic dipole transition $\eta' \rightarrow \rho\gamma$ described above hence is

$$\frac{d\Gamma}{dm_{\pi\pi} d\cos\vartheta} \propto k^{*3} \sin^2\vartheta \frac{\Gamma(\pi\pi)}{(m_\rho^2 - m_{\pi\pi}^2)^2 + m_\rho^2 \Gamma(\pi\pi)}. \quad (2.54)$$

Chapter 3

The Experiment

The data studied in this paper were taken in the year 1986 with the CELLO detector at the e^+e^- storage ring PETRA at DESY in Hamburg. Since 1978 five collaborations conducted experiments with centre of mass energies up to 46.8 GeV in the four interaction regions at PETRA [25]. After 1986 data taking was stopped and PETRA was modified for its future role as an injector for the HERA storage ring. In 1986 measurements were performed at a centre of mass energy of 35 GeV. For CELLO this last year yielded data corresponding to an integrated luminosity of $86pb^{-1}$.

The first section of this chapter describes the main features of the CELLO detector which are relevant for the analyses presented in this paper. A description of the storage ring PETRA and the other experiments can for instance be found in ref.[26]. The subsequent sections describe the data flow through the chain trigger – data acquisition – filter – event reconstruction – data reduction.

3.1 The CELLO Detector

Due to the relatively low event rate most detectors at e^+e^- machines are designed as general purpose detectors. In contrast to detectors at fixed target machines, which select one or more particular processes to be studied, these are built to record all types of events of interest.

CELLO was constructed as such a general purpose detector in 1978 by a group of French and German institutes [27]. The main requirements are a full coverage of the solid angle to measure and possibly identify charged and neutral particles. A special technical feature of the CELLO detector is the superconducting coil of an at that time novel design with an overall thickness of only 0.5 radiation lengths including the cryostat and insulating material. This design allows an undistorted energy measurement of photons and electrons in the lead liquid argon calorimeter surrounding the coil. Due to the fine segmentation of the calorimeter shower topologies are easily reconstructed and photons and electrons can be identified and separated from hadrons [28]. The above components surround the cylindrically symmetric central tracking chamber which has a length of 2.2 m and thus allows to measure charged particles over a large solid angle (97 % of 4π). Together with good hermeticity of the calorimeters (coverage down to an angle of 45 mrad with respect to the beam axis) CELLO has a large efficiency for reconstructing truly exclusive events, i.e. events where all final state particles are detected.

3.1.1 Overview

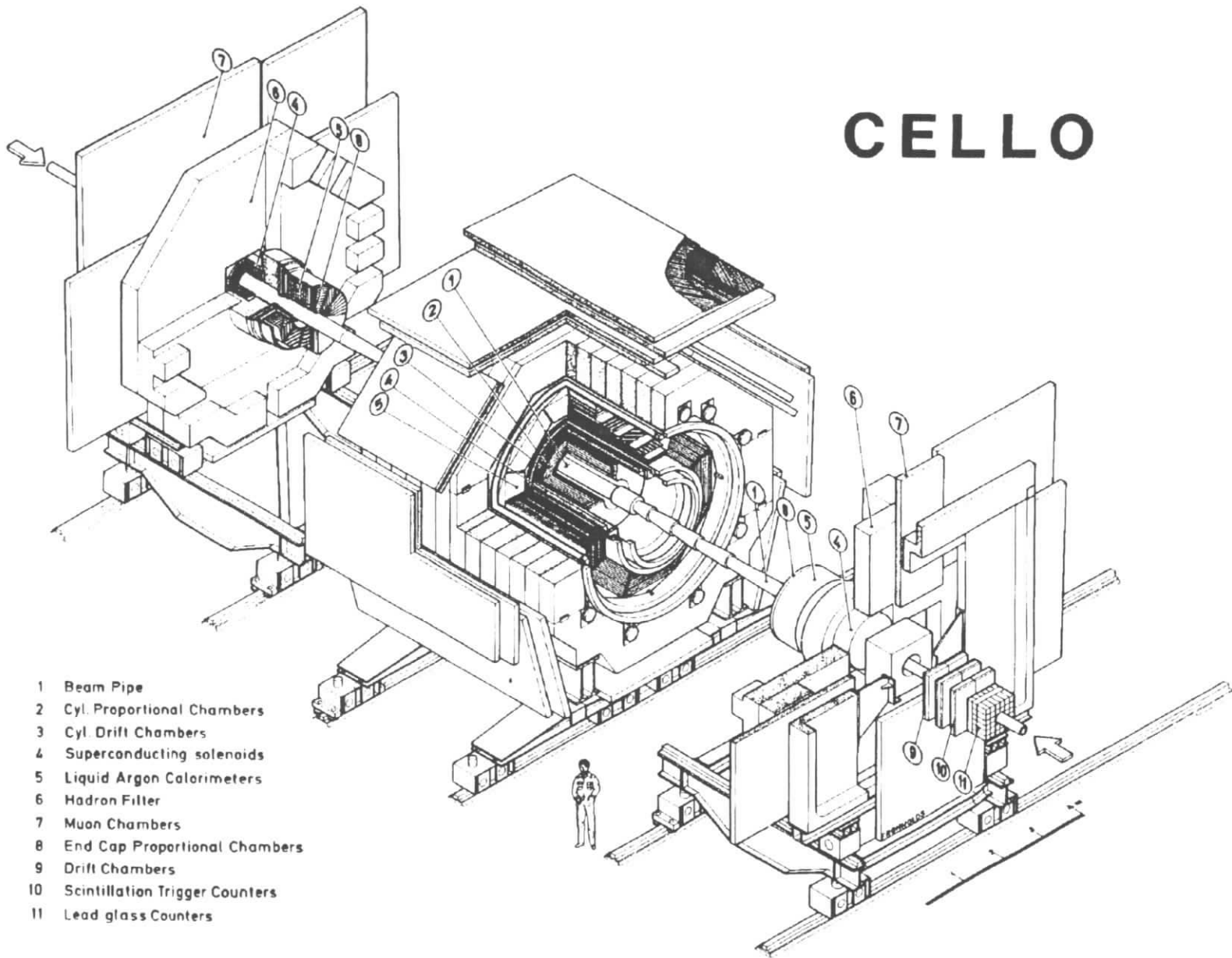
Figure 3.1 shows a schematic view of the detector at the time of construction. Various components have later been added or modified. The following list gives an overview of the detector parts at the time of the last run period in 1986. Those parts which are relevant for the analysis will be described below. A detailed description of the other components can be found in reference [27]. Going from the inner parts to the outer parts of the detector one will find the following components:

- **beam pipe.** The aluminium vacuum pipe surrounds the beam axis at a distance $r = 7.8 \text{ cm}$. The wall thickness is 0.03 radiation lengths (X_0) (before 1982 $0.07 X_0$).
- **beam pipe chambers.** Since 1982 two staggered layers of drift tubes with a length of 1 m surround the beam pipe. Their thickness amounts to $0.01 X_0$. These chambers were added in order to improve the vertex reconstruction [29].
- **central detector.** The central detector consists of a system of cylindrical drift and proportional chambers that measure track coordinates of charged particles between $r = 17 \text{ cm}$ and $r = 70 \text{ cm}$. The amount of matter in these components sums up to $0.02 X_0$.
- **superconducting solenoid.** The aluminium coil with a wall thickness of $0.5 X_0$ creates a solenoidal field of 1.32 T .
- **barrel calorimeter.** The central barrel shaped lead liquid argon calorimeter consists of 16 identical modules with a depth of $20 X_0$. Their distance from the beam axis is $r = 106.7 \text{ cm}$.
- **return yoke.** The 80 cm thick iron construction not only serves as a return yoke for the magnetic flux but also as a hadron filter of 5-8 absorption lengths.
- **muon chambers.** Muons with momenta $p > 1.2 \text{ GeV}$ traverse the hadron filter and are subsequently detected in the muon chambers. These large area chambers with a drift cell structure are read out as proportional chambers and cover approximately 90 % of the solid angle.

In the forward region the detector is completed by:

- **end cap calorimeter.** This lead liquid argon calorimeter consists of four modules of $21 X_0$ complementing the barrel calorimeter in the forward region.
- **hole tagger.** A set of scintillation counters with $4 X_0$ material in between was added in 1982 to close the acceptance hole for neutral particles between the barrel and end cap calorimeters.
- **end cap proportional chambers.** Two crossed layers of proportional chambers in front of the end cap calorimeter improve the reconstruction of forward going tracks.
- **forward calorimeter.** Due to the installation of mini beta quadrupoles in 1982, the forward detector was totally remodeled and now consists of a set of scintillator strips and lead glass blocks to measure the position and energy of scattered electrons and positrons.

CELLO



- 1 Beam Pipe
- 2 Cyl. Proportional Chambers
- 3 Cyl Drift Chambers
- 4 Superconducting solenoids
- 5 Liquid Argon Calorimeters
- 6 Hadron Filter
- 7 Muon Chambers
- 8 End Cap Proportional Chambers
- 9 Drift Chambers
- 10 Scintillation Trigger Counters
- 11 Lead glass Counters

Figure 3.1: Sideview of the CELLO detector

A schematic view of the geometrical acceptance of the detector components is given in figure 3.2. Here, only the innermost components of the detector are shown. The CELLO coordinate system is defined with the z -axis along the flight direction of the incoming electrons. The x -axis lies in the plane of the storage ring pointing outwards, the y -axis is defined by $\hat{y} = \hat{z} \times \hat{x}$. In the plane perpendicular to the beam axis the polar coordinates r and φ are used, the angle ϑ is determined with respect to the z -axis.

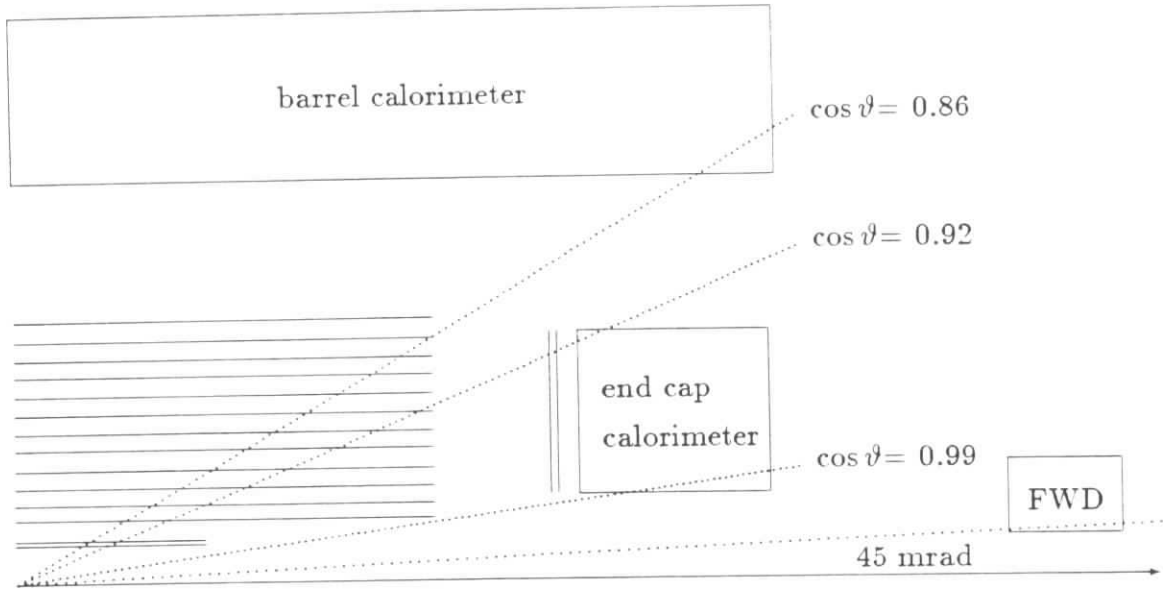


Figure 3.2: Geometrical acceptance of the CELLO detector

3.1.2 Central Track Detector

The central detector consists of a system of cylindrical drift and proportional chambers. They are mounted concentrically to the beam axis and have an outer radius of 0.7 m and an overall length of 2.2 m . Altogether there are 7 drift and 5 proportional chambers. Their position and other parameters can be taken from table 3.1.

The two inner chambers have been added in 1982 to improve the vertex reconstruction in the $r\varphi$ -plane. They consist of two layers of drift tubes that are arranged parallel to the beam axis with a length of 1 m . Each of the drift tubes contains a single anode wire in a gas mixture of 50 % argon and 50 % ethane at atmospheric pressure. The coordinates perpendicular to the beam axis are determined by a measurement of the time difference between the passage of a particle through the drift tube and the arrival of the ionization pulse on the anode wire. The resolution achieved in this chamber is $180\ \mu\text{m}$ [29].

The drift chambers are constructed from entirely open drift cells. Each drift cell consists of one anode wire separated from adjacent ones by a set of three cathode wires. The lateral distance between adjacent anode wires is on the average 15 mm . The drift chambers are grouped in sets of two or three chambers with a common gas volume enclosed by two mylar cylinders. As in the case of the drift tubes a gas mixture of argon and ethane in a ratio of 1:1

chamber number	chamber type	radius [cm]	number of signal wires	distance of wires [mm]	# cathode strips	
					90°	30°
1	drift tube	10.90	128	5.35	—	—
2	drift tube	11.37	128	5.54	—	—
3	prop. ch.	17.0	512	2.09	252	256
4	prop. ch.	21.0	512	2.58	228	256
5	drift ch.	25.5	104	15.41	—	—
6	drift ch.	30.4	128	14.92	—	—
7	prop. ch.	35.7	1024	2.19	366	512
8	drift ch.	40.2	168	15.03	—	—
9	drift ch.	45.1	192	14.76	—	—
10	drift ch.	50.0	208	15.10	—	—
11	prop. ch.	55.3	1536	2.26	420	768
12	drift ch.	59.8	256	14.68	—	—
13	drift ch.	64.7	256	15.88	—	—
14	prop. ch.	70.0	1536	2.86	494	768

Table 3.1: Geometrical and electrical parameters of the central tracking detector.

at atmospheric pressure is used. The resolution of the $r\varphi$ -coordinates reconstructed from the space-drift-time-relation is $170 \mu\text{m}$ [30].

The proportional chambers are used to determine the z -coordinate of track points. This is accomplished by two cylindrical cathodes finely segmented in strips orientated at 90° and 30° with respect to the cylinder axis. The two cathode cylinders enclose a large number of axial anode wires with mutual spacings of the order of 2.5 mm . The precision of the $r\varphi$ -coordinate measurement is given to first order by the geometrical resolution $\text{spacing}/\sqrt{12} \approx 770 \mu\text{m}$. The charge induced on the cathode strips at the point of incidence next to the anode wire is measured by an analog readout of each strip. The resolution of the z -position achieved this way is $\sigma \approx 440 \mu\text{m}$. The proportional chambers are run with a gas mixture of 80 % argon and 20 % isobutane with an admixture of 0.2 % freon. Besides determining the z -position of track points the proportional chambers are used in the fast track trigger. The information from both projections are already available after $2 \mu\text{s}$.

The tracking detector is completed by two crossed layers of proportional chambers which are mounted onto the front end of the end cap calorimeter. The anode wires measure the x - and y -coordinates while the cathode planes are divided into sectors of $\Delta\varphi$ and concentric rings, respectively. The resolution is of the order of 5 mm . The end cap proportional chambers cover the acceptance region of $0.910 < |\cos\vartheta| < 0.988$ [27].

The geometrical acceptance of the central tracking detector is 84 % of 4π if a track is required to hit all 14 chambers. Using in addition the information of the end cap proportional chambers and requiring only five chambers of the inner detector to determine all track parameters the acceptance is increased to 97 % of the full solid angle.

The deflection of charged particles in the magnetic field of the CELLO superconducting coil forces the particles onto circular tracks in the $r\varphi$ -plane with a curvature proportional to their transverse momentum. The precision of momentum reconstruction depends on the number of track points measured, the resolution of the chambers and on multiple scattering in the detector material traversed. The momentum resolution of the CELLO central detector

was determined to be [29]:

$$\frac{\sigma_{p_t}}{p_t} \approx 2\% \cdot p_t$$

where p_t is measured in GeV. The vertex of a track can be determined with a precision of $\approx 330 \mu m$.

3.1.3 Lead Liquid Argon Calorimeter

The CELLO calorimeter has a sampling structure of lead layers alternating with layers of the active material argon. Electrons and photons create a secondary particle cascade by means of bremsstrahlung and pair creation. The ionization loss of these secondary particles is recorded in the argon. Electromagnetic showers at the maximum PETRA energies are fully absorbed in the $20 X_0$ structure of the calorimeter. A good detection efficiency, energy resolution and spatial resolution of photons is achieved over the entire solid angle. Cascades induced by hadronic particles, however, are not completely contained in the calorimeter due its depth of only 0.9 absorption lengths. This feature on the other hand allows a good electron-hadron separation. This is accomplished by the three dimensional reconstruction of shower topologies in the highly segmented calorimeter structure [28].

The barrel calorimeter is composed of 16 modules with trapezoidal cross section corresponding to a sector of an octagon. The two octagons are mirror images arranged symmetric to $z = 0$ inside one large cryostat with an overall length of 4 m. The end cap calorimeter consists of 4 half cylindrical stacks; two of them at each end of the detector enclose the beam pipe.

The modules in each of the calorimeters are identical. Layers of 1.2 mm lead plates (cathodes) and 1.2 mm lead strips (anodes) alternate (see figure 3.3 a)). The gap width between the lead layers is 3.6 mm (4 mm in the end cap calorimeter) and is filled with liquid argon. The lead strips and plates are at a relative voltage of 2.5-5 kV. The orientation of the strips in the barrel part alternates between an alignment parallel to the beam axis (φ -measuring), with an angle of 90° (ϑ -measuring) and at 45° (to resolve ambiguities). The strips in the end cap calorimeter are alternately vertical, horizontal and circular. The width of the strips is of the order of 2-3 cm. In front of the calorimeter there are two additional copper liquid argon layers (three in the end cap) which serve as dE/dX-gaps.

There are more than 3000 strips in each of the modules. In order to decrease the number of electronic channels, neighbouring strips have been grouped to block layers (see fig.3.3 b))

	barrel calorimeter	end cap calorimeter
material in front of calorimeter	1.1 X_0	1.2 X_0
depth of calorimeter	20 X_0	21 X_0
thickness of lead layers	1.2 mm	1.2 mm
distance between lead layers	3.6 mm	3.6 mm
number of layers	41	42
number of electronic channels	9248	1472
angular resolution	4 mrad	6 mrad
acceptance in $ \cos \vartheta $	< 0.86	0.92-0.99

Table 3.2: Technical data of the liquid argon calorimeters.

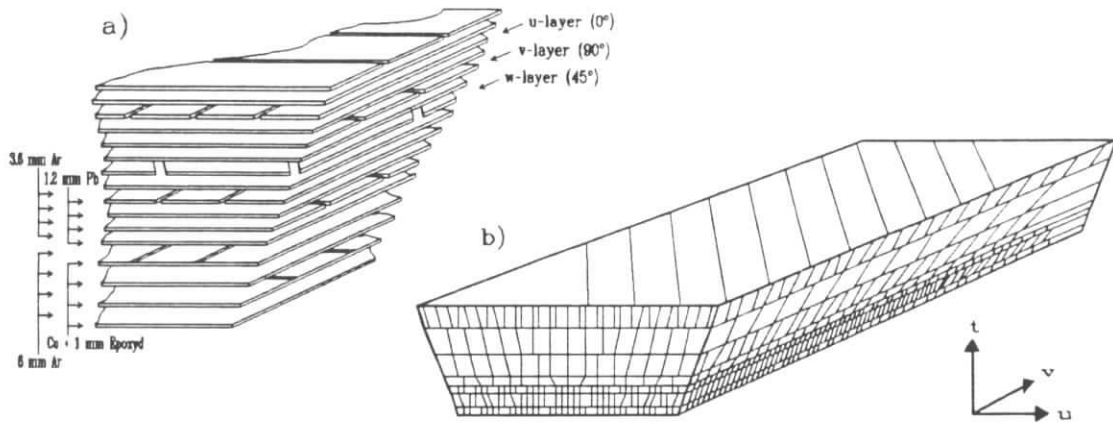


Figure 3.3: Geometric (a) and electronic (b) structure of the lead liquid argon calorimeter

with a scheme that yields a uniform angular resolution. For the azimuthal angle φ this uniform resolution is given by the octagonal structure of the calorimeter, for the polar angle ϑ (measured from the beam axis) it is achieved by a coarser read out structure towards the forward region. A detailed description of this read out block structure is given in [28]. The number of channels to be read out is thus reduced to 576 in a barrel module and 368 in an end cap module. To reduce the amount of data written to tape, channels with a signal below 2.5σ above the electronic noise pedestal are suppressed. The electronic noise in a double layer corresponds to ≈ 1 fC. This has to be compared with the charge deposit of 5 fC for a minimum ionizing particle [28].

The energy resolution of the calorimeter is given by the sampling fluctuations. A further degradation results from material in front of the calorimeter, miscalibration, dead channels etc. The resolution for electromagnetic showers in the CELLO calorimeter achieved in the running experiment is:

$$\frac{\sigma_E}{E} = 5\% \oplus 10\%/\sqrt{E}$$

with E being measured in GeV (\oplus = quadratic addition of the terms).

Besides measuring final state particles the end cap calorimeter is also used in this analysis to tag the scattered electrons of the two-photon reactions at large angles (i.e. above 100 mrad). An important parameter for the measurement of such a tag is the squared momentum transfer or invariant mass squared of the virtual photon. The uncertainty in the determination of Q^2 results from errors of energy and scattering angle of the tag:

$$\frac{\sigma_{Q^2}}{Q^2} = \left(\left(\frac{\sigma_E}{E} \right)^2 + 4 \cdot \left(\frac{\sigma_\vartheta}{\vartheta} \right)^2 \right)^{\frac{1}{2}}$$

which leads to a resolution of $\sigma_{Q^2}/Q^2 \approx 10\%$.

3.1.4 Forward Calorimeter

The forward calorimeters measure electrons that are scattered at small angles not accessible to the end cap calorimeter. They serve as a monitor for the luminosity measurement based on Bhabha events and are used as a trigger for two-photon reactions.

The calorimeters are located at a distance of 2.65 m from the interaction point and cover the acceptance region from 45-110 mrad. Lead glass blocks are used as shower counters; 20 blocks are found on each side of the detector. Each half circular quarter containing 10 blocks is mounted directly onto the beam pipe. The lead glass blocks have lateral dimensions of typically 5 cm ($= 2 X_0$) and a length of 13 X_0 . The Cherenkov light emitted by the charged particles in the shower cascade is detected by photomultipliers. The positional measurement of the tagged electrons is improved by means of a scintillator hodoscope. Half circular scintillator strips of 1 cm width are read out by photomultipliers at each end. A thin layer of lead ($0.5 X_0$) is used for an early start of the shower cascade and hence an increased signal in the scintillators. Comparing the light output at each end allows a determination of the position along the scintillator (φ -coordinate), the radial position of the scintillators hit determine the angle with respect to the beam axis. This information is combined with the centre of gravity position from the lead glass blocks.

Due to the location of the forward counters a large amount of material is positioned in front of the calorimeter. This fact degrades the energy resolution over a large range, in some regions the energy measurement cannot be used at all. On the average the material in front of the calorimeter amounts to 2 X_0 up to an angle of 90 mrad, above, the end cap cryostat shields the forward calorimeter with 10 X_0 of material.

3.2 Data Acquisition and Event Reconstruction

Every 3.8 μs the electron and positron bunches cross each other in the interaction region of the CELLO detector. Most of the bunch crossings do not result in any physically interesting interaction. Due to the small cross section, annihilation events occur with a rate of 1 per 10 minutes at the typical luminosity of $5 \cdot 10^{-30} nb^{-1} s^{-1}$. Background reactions like interactions of beam particles with the residual gas in the beam pipe (*beam gas events*), with the material of the beam pipe wall (*beam wall events*) or cosmic ray events (*cosmics*) and synchrotron radiation are by far more abundant. In order to decrease these sources of background and still accept the majority of physically interesting events a fast trigger logic is essential. The time needed to fully read out all detector components limits the data acquisition rate to about 5 Hz. In order not to lose too many interesting events the trigger conditions cannot be too strict, and hence, a second filter is needed to reduce the amount of background accepted by the loose trigger conditions and to minimize the expenditure of computer-time needed for the full reconstruction of the data.

The forthcoming sections describe the sequence of data acquisition and reconstruction through the chain trigger, filter, event reconstruction and data reduction.

3.2.1 Trigger System

The trigger uses information from all components of the detector. The basic conditions are combined to give the trigger conditions selected. Basic conditions are for example the energy sums in the calorimeter modules, the energy in the forward calorimeter and the number of

tracks in the central and end cap track detector. Altogether there are 16 trigger conditions defined for the CELLO detector, one of which has to be fulfilled for an event to be recorded. The different conditions cover the various signatures of e^+e^- collisions. Here we only describe those conditions that are relevant for triggering two-photon events.

The fundamental ingredient for the charged particle trigger is a software programmable hardware track finding processor [31]. This processor employs the information of the five proportional chambers and of two of the drift chambers for the identification of tracks in the $r\varphi$ -projection and of the 90° cathodes for the rz -projection. The chamber signals are divided into 64 azimuthal (as shown in fig.3.4) and 37 polar sectors. Each track creates a certain

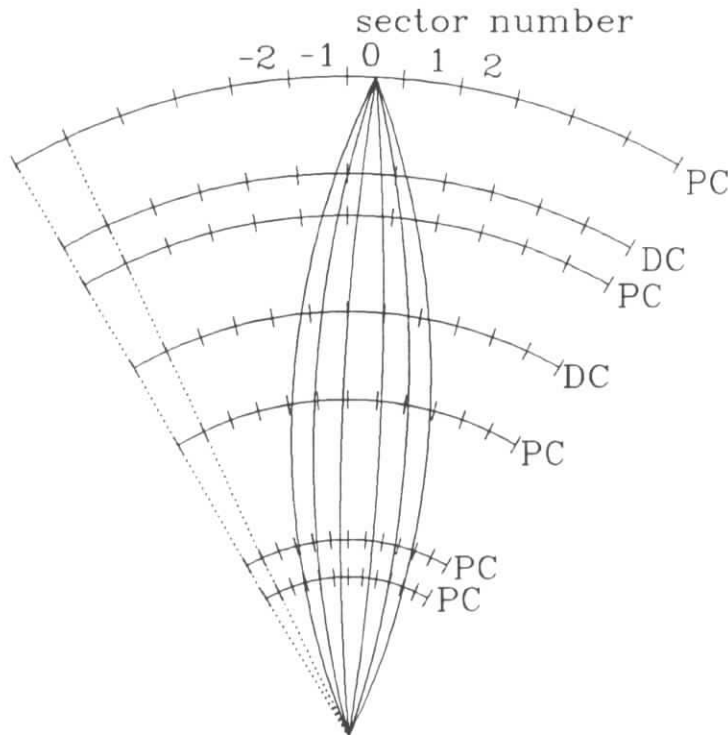


Figure 3.4: $r\varphi$ -sectors for the trigger logic: Shown are the seven chambers used in the trigger, their segmentation in the $r\varphi$ -projection and several tracks that end in sector 0.

signal pattern in the sectors of the seven chambers. All possible patterns of tracks above a certain transverse momentum can be determined. These patterns are then stored in random access memories (RAM) – one set for transverse momenta above 650 MeV ($r\varphi_H$ masks) and one set for $p_T > 250$ MeV ($r\varphi_L$ masks). To take into account chamber inefficiencies additional masks are stored with only 5 or 6 points per track. These precomputed masks are compared with the signals from the central detector. If the pattern coincides with any of the masks the corresponding condition is transferred to the master trigger unit. A similar identification is done in the rz -projection where at least three out of five hits in the proportional chambers are required. The location of masks is done in less than $1 \mu s$.

The neutral particle trigger utilizes the information of the liquid argon calorimeter. Here the energy of a stack is computed by means of a hardware sum of all channels. Using discriminators several trigger conditions can be defined corresponding to the energy deposited in the calorimeter. This system of discriminator triggers (LA1 to LA4) has been supplemented with and partly replaced by a system of flash ADCs [32]. For every module two trigger sums

trigger	track and shower condition	opening angle	other conditions
5	$r\varphi_H(2) * rz(1)$	$> 135^\circ$	—
15	$r\varphi_H(2) * rz(1)$	—	cathode veto beam pipe veto
16	$r\varphi_L(2) * rz(1)$	$> 45^\circ (135^\circ)$	cathode veto
7	$(r\varphi_L(1) * rz(1) + \text{LA4FL}) * \text{FWD}$	—	—
10	$(r\varphi_L(1) * rz(1) + (\text{LA3} + \text{LA4FL})) * \text{LAEC1}$	—	—

Table 3.3: Trigger conditions: the symbol * denotes a logical AND, the symbol + a logical OR; the opening angle refers to the tracks in the $r\varphi$ -projection.

are formed by summing up all channels or those channels that lie in the region of the maximum of electromagnetic showers ($4-7 X_0$). The second sum is taken at a different time to exploit the shape of the FADC signal. Thus showers can be rejected that do not coincide with the beam crossing (e.g. cosmics, electronic noise). All the above information is combined to four trigger conditions LA1FL to LA4FL.

Inside the master trigger unit the number of masks $r\varphi$ (n) and rz (m) found is combined with further basic conditions to give the final trigger criteria. The triggers required for events analysed in this thesis are listed in table 3.3. Here trigger 5, 15 and 16 are pure track triggers. Trigger 15 additionally demands less than 16 cathode signals in the two inner proportional chambers (*cathode veto*) and less than 50 hits in the beam pipe chambers (*beam pipe veto*). These two requirements suppress beam wall and beam gas events. The remaining two triggers listed are used to trigger single tag events with one track reconstructed in $r\varphi$ and rz and in addition with an energy above 1.5 GeV in the end cap calorimeter (LAEC1) or above 2.0 GeV in the forward calorimeter (FWD).

3.2.2 Data Acquisition

The CELLO data acquisition system is steered and controlled by an online computer of the type DEC PDP-11. The detector is read out by a CAMAC system which is organized in a tree like structure: each detector component is assigned to a branch, the online computer is the root. Each branch is controlled by a minicomputer. These minicomputers are used to calibrate and test the assigned detector components without interfering with the rest of the system. During data acquisition they monitor the performance of their detector component. Zero suppression of channels without information is already accomplished at this level, block addresses are added to the remaining data words for identification.

Once the master trigger unit sends its interrupt signal to the online computer, the PDP-11 stops all other operations, disables further triggers and starts with the data acquisition. The information from all branches is transferred to the main memory where it is formatted into a data structure with variable length (typically several hundred to several thousand 16-bit words). During this process the data structure is checked and in the case of severe readout errors the event is rejected. Already at this stage a fast track reconstruction is done which is used to verify the track triggers and on the bases of the number of tracks found the event is classified. Candidates for multihadronic and Bhabha events are marked for separate reconstruction. All events are then passed on and the readout system is again enabled for further data acquisition. This whole process takes about 50 ms.

The data are transmitted via a permanent link to the IBM in the DESY computer centre.

There, an online program stores the event on a disk file which is organized as a ring buffer. Once the space on this buffer is almost exhausted the data is copied to magnetic tape (DUMP tapes).

Events marked by the online computer are immediately reconstructed and then written to a special disk file. These events are scanned by the shift crew using an interactive display program to monitor detector performance and reconstruction chain.

The Bhabha events are furthermore used to determine the position of the interaction point of each filling of the PETRA storage ring. The knowledge of this position is crucial for the further reconstruction of the data, since all track parameters are determined relative to the primary vertex.

3.2.3 Filter

Soft trigger conditions are essential for the acquisition of two-photon events. This, on the other hand, increases the amount of background reactions acquired and hence a preselection of events is necessary before the time consuming full reconstruction of the data. Such a filter offers the possibility to conduct a more refined analysis of the events than the one done on the trigger level.

The CELLO filter program [34] analyses the events without referring to the trigger explicitly. The basic input informations used in this program are :

- the inner detector wire chamber coordinates
- the hardware energy sums in the calorimeters
- the energy of single channels in the liquid argon calorimeter

In a first step charged tracks coming from the interaction point (assumed at $r=0$ with an uncertainty of 3 cm) are reconstructed in the $r\varphi$ -plane requiring a minimum of 9 points per track. In a second stage the reconstruction of tracks in the rz -projections is performed with no assumptions about the interaction point. Instead, there must be at least one track with a z -vertex not more than 5 cm apart from the z -vertices of 60 % of all other tracks. For those events a common z -vertex is computed that has to be within ± 15 cm around the origin ($z = 0$). Otherwise all reconstructed tracks are ignored.

The energy sums of the calorimeters are classified according to their energy levels. For each stack the signal time relative to the time of the interaction is computed from the FADC sums taken at two different times. Signals in a stack within ± 300 ns around the expected time are classified as *in time*. In a second stage showers are reconstructed from the signals of the single channels in the liquid argon calorimeters.

Finally, at least one of the fired triggers has to be verified on the bases of the analysis described above. Less than 1 % of all reconstructable events for most of the reactions are effected this way.

During data acquisition the filter program runs on an IBM 370/E emulator. The events are read in from the online disk and marked *accepted* or *rejected* according to the criteria selected. An identical program executes on the central DESY IBM computer. This program reads in all events – analyses all events accepted by the emulator and those not analysed by the emulator due to time limitations – and writes all accepted events onto magnetic tapes (FILTER tapes). In addition as a check 5 % of the events marked rejected are reconstructed once more.

In the run period 1986 out of 61.5 million events 7.5 million (12.2 %) were accepted by the filter. The FILTER tapes for that year are used as an input for the full event reconstruction described in the following section.

3.2.4 Event Reconstruction

The raw event data are processed by several independent programs, called processors. The main program OFFRAM constitutes a frame around these processors, steers the sequence of reconstruction and delivers the required information about the conditions of the detector components (calibration constants, defect channels, resolutions, etc.) to these processors. The results of the reconstruction, e.g. track and shower parameters, are stored in *banks* and are written together with the raw data onto data summary tapes (DST tapes). Because of the huge amount of computing time needed, the production of the DST tapes is split up between several of the institutes participating in the CELLO collaboration.

The program OFFRAM embodies the following processors :

CELPAT: The program CELPAT reconstructs tracks of charged particles in the inner detector by an iterative procedure described below. First, the signal of the anodes and the 30° and 90° cathodes of the proportional chambers are correlated to form three dimensional space points; tracks in the rz -plane are formed by a fit to a straight line pointing to the interaction region. Then, three points in the $r\varphi$ -projection are searched for, that can be connected by a segment of a circle passing the interaction point not further than 15 cm. The points used have to lie within one of the predefined sectors in the inner detector which corresponds to a cut in the transverse momentum of the particle. In the vicinity of the segment further points are looked for. A collection of at least 7 points (6 points for low momentum tracks) is called a track candidate. After a successful fit of these track candidates the points used are excluded from the search for further candidates. This procedure is repeated with larger sectors corresponding to smaller transverse momenta until, finally, low energetic tracks with momenta down to 100 MeV are reconstructed. At last, complete tracks are formed by combining the $r\varphi$ and rz -parts with the help of the spatial information of the proportional chambers.

CLGEOM: For the tracks found by CELPAT a further fit is performed including the interaction point and taking into account the inhomogeneties of the magnetic field. The usage of the primary vertex position determined from the Bhabha events improves the momentum resolution of tracks coming from the interaction point. For the case of particles created at secondary vertices this result cannot be used.

ECCPAT: Particles traversing the detector in the very forward region ($0.91 < |\cos \vartheta| < 0.99$) only hit very few chambers of the inner detector. Using in addition the hits in the end cap chambers and including the primary vertex as a measured point, ECCPAT reconstructs these forward going tracks.

LATRAK: The processor LATRAK reconstructs showers in the liquid argon calorimeters. At first, two-dimensional shower energy clusters are formed in each layer of the calorimeter employing the different directional orientation of the lead strips (cf. section 3.1.3). For all tracks in the inner detector pointing to the two-dimensional clusters, three-dimensional

clusters are constructed along the flight direction of the particle. A straight line fit is applied including the intersection point of the track with the magnetic coil to determine the orientation of the shower inside the liquid argon. All other three-dimensional showers are constructed under the assumption that they are created by photons coming from the primary vertex.

LNKJOB: This program links showers to tracks in the inner detector. This assignment of showers initiated by charged particles prevents them from being treated as photons later on.

MUCH: This last processor extrapolates tracks through the calorimeter and the hadron filter and combines them with the hits in the muon chambers. The distance between the extrapolated position and the actual hit is a measure for the quality of the identification as a muon.

For the purpose of this and several other analyses substantial improvements have been implemented in the reconstruction chain, e.g. identification of secondary vertices [35], particle identification below 1 GeV in the liquid argon calorimeter [28], shower reconstruction in the forward calorimeter and an improvement of photon identification and their discrimination from electronic noise.

3.2.5 Data Reduction

Following the data reconstruction there are two more selection steps. The first one consists of soft cuts to obtain all annihilation and two-photon events. This selection is the basis for next to all physical analyses conducted in the CELLO collaboration. The second selection yields events resulting from two-photon reactions.

For final states with low multiplicity, as in the case of two photon reactions, the following conditions have to be fulfilled:

- ≥ 2 tracks with at least 5 points per track *and*
- at least one positive and one negative track *and*
- less than 50 hits in the beam pipe chambers *and*
- not exactly two tracks in opposite side end caps with both energies > 5 GeV (to reject end cap Bhabhas)

For tagged events trigger condition 7 or an energy above 3 GeV in the end cap calorimeter is demanded in combination with at least one track with $|\cos\vartheta| < 0.9$.

Events that meet these condition are written to magnetic tape (SELECT tapes) [36]. This selection still contains 3.5 million events. To further reduce the amount of data and to restrict the events to low multiplicity final states, at least 2 and no more than 8 tracks are demanded with a charge balance of ± 1 . These 1.3 million events are written to the SELGGEX tapes, which are used as a starting point for all two-photon analyses.

Chapter 4

Monte Carlo Simulation

Only a very small fraction ($\approx 1\%$) of the resonances produced in two-photon reactions are actually detected and the final states they decay into are fully reconstructed. This fraction is commonly referred to as the detector acceptance. A detailed understanding of its magnitude and its dependence on the measured quantities is crucial for the determination of the cross section of any process. However, the acceptance cannot be calculated analytically for the detectors used in high energy physics. A numerical method is used instead to determine the acceptance, based on so called *Monte Carlo* descriptions of the various detector components and their response to the particles traversing them.

Furthermore, the calculation of the integral (e.g. equation 2.40) describing the functional dependence of the cross section σ on the radiative width of a resonance cannot be achieved by analytical methods if no approximations to the formulas are applied. So here as well a numerical method for its determination is needed. Programs have been developed that make use of these Monte Carlo techniques.

The following sections describe the Monte Carlo integration of the cross section, the generation of events based on this cross section and the tracking of the generated particles through the detector components. This will lead to a determination of the detector acceptance which in turn is used to calculate the cross sections and radiative widths of the resonances under study.

4.1 Event Simulation

4.1.1 Event Generation

It has been shown in section 2.4 that the quantity of interest $\Gamma_{\gamma\gamma}(R)$ is a linear parameter in the cross section formula. The radiative width of a resonance can be determined from the counting rate of the reaction $e^+e^- \rightarrow e^+e^-R$, which implicitly is integrated over the kinematical region available to the final state particles. For reactions at e^+e^- colliders like PETRA only five independent kinematical variables have to be considered, since no azimuthal dependence is expected for unpolarized lepton beams. The variables used for the integration of the cross section are the normalized three-momenta $x_i = |\vec{p}_i|/p_{beam}$ of the scattered leptons, their scattering angles ϑ_i with respect to their initial flight direction and the azimuthal angle $\bar{\varphi}$ between the lepton scattering planes. The integration for the x_i is performed over the full range from 0 to 1, because no additional information is available about the energies of the scattered leptons. Likewise, the angle $\bar{\varphi}$ is integrated over the range between 0 and 2π . Only

for the scattering angles ϑ ; some limits can be introduced due to the known experimental acceptances. For tagged and untagged events the range is taken from 0 to 450 mrad (0-40 mrad would be sufficient for untagged events, since above 40 mrad limit the scattered leptons will be detected by the forward calorimeters with high efficiency). For the calculation the radiative width $\Gamma_{\gamma\gamma}$ (later to be determined) is set to 1 keV. If the numerical value of the integration is called INT , the cross section and radiative width are related by the following expression:

$$\sigma_{\epsilon^+\epsilon^-\epsilon^+\epsilon^-R} [pb] = INT \cdot \Gamma_{\gamma\gamma}(R) [keV] \quad (4.1)$$

The other quantity to be measured is the Q^2 -dependence of the form factor. It is determined by comparing the number of events in every Q^2 -interval to the number of generated events if no form factor was present. A generation of events with such a *flat form factor* would, however, lead to an enormous number of events for large values of Q^2 , where only few events are expected as known from previous measurements of form factors. This large number of events would lead to an unnecessary consumption of CPU time in the subsequent detector simulation. To circumvent this problem and, yet, keep a reasonably small statistical error in the higher Q^2 -intervalls the events are generated with a J/Ψ -form factor and afterwards weighted according to a flat form factor.

A program package that performs the five dimensional integration of the cross section has been developed by Feindt [37]. The program MOTTE0 integrates the cross section for the two-photon process $\epsilon^+\epsilon^- \rightarrow \epsilon^+\epsilon^-R$ over the scattered particle phase space using the method of *importance sampling* based on the routine BASES by Kawabata [39]. The starting point for this program is the cross section formula in the form given by Budnev [7] (see eq. 2.16). A parameter transformation is carried out such that the integration is performed in hypercubes over the five variables introduced above. For narrow resonances such a numerical integration will however not converge sufficiently. The definition of hypercubes is much more effective when the variables x_1 and x_2 are replaced by $W_{\gamma\gamma}$ and x_2 [38]. In this plane hypercubes can be found where the function to be integrated is more or less flat. The result of the integration is a five dimensional grid for the cross section that is used as an input for the second program MOTTE1. Here the four-vectors of all particles participating in the full process $\epsilon^+\epsilon^- \rightarrow \epsilon^+\epsilon^-R$ are generated and written to tape. Table 4.1 shows the number of four-vector events generated for each of the reactions studied.

resonance	ϑ -range	INT	# events	W -range	form factor
η	0-450 mrad	3440.2	300000	0.5480-0.5496	J/Ψ
η'	0-450 mrad	468.79	360000	0.955-0.960	J/Ψ
$a_2(1320)$	0- 50 mrad	1872	120000	0.88-1.76	ρ
$f_1(1285)$	0-450 mrad	371.5	100000	1.000-1.566	$J/\Psi(TT)$
	0-450 mrad	170.3	100000	1.000-1.566	$J/\Psi(LT)$

Table 4.1: MC generated events on the four vector level

The generated resonances then decay into the final states under study. The decay of the pseudoscalar resonances into the various final states is accomplished using a set of routines from the program package SAGE [40]. These routines generate phase space distributed decays.

The decay into the final state $\rho\gamma$, on the other hand, takes into consideration a matrix element linear in the centre of mass momentum k^* of the virtual photon for the magnetic

dipole transition nature of the decay $\eta' \rightarrow \rho\gamma$ and the limited phase space available for this decay (see section 2.5).

The production of the spin-1 resonance $f_1(1285)$ is generated according to the cross sections of the Cahn model (cf. eqs. 2.46). Since the decay predominantly proceeds via the intermediate state $\delta\pi(\delta^\pm \rightarrow \pi^\pm\eta)$ no direct phase space decay into three particles has been considered. The calculation of the matrix element for the decay via the intermediate state mentioned follow the formulae of appendix D in ref [6], taking into account the interference between the two possible combinations of forming the intermediate δ -resonance (called $a_0(980)$ in ref. [17]). With the abbreviation $BW_i = 1/\{(P^2(\delta_i) - M^2(\delta_i)) + iM(\delta_i)\Gamma(\delta_i)\}$ the matrix elements used are for the transverse-transverse coupling:

$$\mathcal{M}(J_z = 0) = (P(\delta_1) - P(\pi_2))_z \cdot BW_1 + (P(\delta_2) - P(\pi_1))_z \cdot BW_2 \quad (4.2)$$

and for the longitudinal-transverse coupling:

$$\begin{aligned} \mathcal{M}(J_z = +1) &= \frac{1}{2} [\{-(P(\delta_1) - P(\pi_2))_x - i(P(\delta_1) - P(\pi_2))_y\} \cdot BW_1 \\ &\quad + \{-(P(\delta_2) - P(\pi_1))_x - i(P(\delta_2) - P(\pi_1))_y\} \cdot BW_2] \end{aligned} \quad (4.3)$$

$$\begin{aligned} \mathcal{M}(J_z = -1) &= \frac{1}{2} [\{+(P(\delta_1) - P(\pi_2))_x - i(P(\delta_1) - P(\pi_2))_y\} \cdot BW_1 \\ &\quad + \{+(P(\delta_2) - P(\pi_1))_x - i(P(\delta_2) - P(\pi_1))_y\} \cdot BW_2] \end{aligned} \quad (4.4)$$

and hence:

$$\mathcal{M}(J_z = \pm 1) = \frac{|\mathcal{M}(J_z = +1)| + |\mathcal{M}(J_z = -1)|}{2} \quad (4.5)$$

4.1.2 Preselection Cuts

Since not all of the generated events decay into the acceptance region of the detector or can be triggered because of their limited transverse momentum, the efficiency of the subsequent detector simulation can be improved by applying the following acceptance cuts on the events:

- $|\cos \vartheta_{\pi^\pm}| < 0.98$ for all charged particles to have a fair chance to be seen in the inner detector.
- $|\cos \vartheta_\gamma| < 0.98$ for photons to be detected in the liquid argon calorimeters, if all final states photon are required to be seen. For the analysis of only partly reconstructed final states this cut is omitted.
- $p_t^2(\pi^\pm) > 0.064 \text{ GeV}^2$ to assure that tracks have enough transverse momentum to be triggered and to be reconstructed by CELPAT.
- $\vartheta_{tag} > 35 \text{ mrad}$ for either of the scattered leptons in reactions studied in the single tag mode.

Only a limited number of events can pass these conditions. Due to the strong fall off of the cross section with large scattering angles, the preselection is far more efficient for untagged events than for those created in the single tag mode. The number of events for each of the various generated final states can be read off from table 4.2. Subsequently these events are passed through the detector simulation described further below. From the number of events passed through the detector simulation and the preselection efficiency the effective

decay	# gen.	# pres.	pres.eff. [%]	# simul.	$\mathcal{L}_{MC}/B(R \rightarrow X) [pb^{-1}]$
$\eta' \rightarrow \rho\gamma$	360000	122151	40.72	48000	242.17
$a_2(1320) \rightarrow \pi^+\pi^-\pi^0$	120000	72095	60.08	23998	21.3
$\eta' \rightarrow \rho\gamma$	360000	35456	9.85	24000	1663
$\eta' \rightarrow \eta\pi^+\pi^-$	360000	35609	9.89	24000	2906
$\eta' \rightarrow 2\pi^+2\pi^-(\pi^0/\gamma)$	360000	27947	7.76	24000	5040
$\eta \rightarrow \pi^+\pi^-\pi^0$	300000	39530	13.18	16000	148.9
$\eta \rightarrow \pi^+\pi^-\gamma$	300000	36573	12.19	15976	775.8
$f_1(1285)_{TT} \rightarrow \eta\pi^+\pi^-$	41645	30000	72.04	15988	384.6
$f_1(1285)_{LT} \rightarrow \eta\pi^+\pi^-$	34045	30000	88.12	15842	1016.8

Table 4.2: Generated and preselected number of events for the various final states under study. The first two lines are for events studied in the untagged mode, the rest for the single tag mode. The effective MC luminosity is given for a radiative width of 1 keV, a J/Ψ -form factor and the branching ratio for this reaction.

MC luminosity generated for a specific process can be calculated using the result INT from the numerical integration of the cross section formula for this process:

$$\mathcal{L}_{MC} = \frac{N_{sim}}{INT \cdot \text{pres.eff.}} \quad (4.6)$$

This number given for a radiative width of $\Gamma_{\gamma\gamma}(R) = 1 \text{ keV}$ and the branching ratio for the specific decay is also displayed in the above table.

4.2 Detector Simulation

Every event generated according to the above scheme is then subjected to a detailed simulation of its way through the detector geometry. Each of the final state particles is carefully traced through the various detector components, taking into account the magnetic field for the charged particles. In each of the components the possible interactions of the particles are randomly chosen from e.g. multiple scattering, ionization, decay of the instable particle, bremsstrahlung, hadronic interaction, absorption, or pair creation for photons according to their relative probability of occurrence. The secondary particles created by either of these processes are as well further traced through the detector. Electromagnetic and hadronic showers are simulated using the program packages EGS and HETC [41]. The energy deposits, the ionization charges and their distance to the anode and cathode wires are stored for each of the detector components.

In a second step the response of the components to these depositions – the *measuring process* – is simulated, e.g. drift times are calculated from the distance of the ionizing tracks to the wires in the chambers and pulse heights in the calorimeters. All of this is stored in a form that corresponds to the output of a TDC or an ADC. To achieve a good correspondence between the simulated and the real detector, a detailed and precise knowledge of the chamber and calorimeter efficiencies as well as the calibration constants of every electronic device attached to it is necessary. To take the changing actual state of the detector into consideration, the whole period of data taking is divided into 25 run ranges corresponding to one week of data acquisition. For each run range the detector is simulated according to

the observed behaviour. Chamber efficiencies are determined from Bhabha events and from a set of selected events containing identified pions. The response of the detector is simulated accordingly. Dead and hot electronic channels are monitored during data taking and the information is written to a *status file*. The simulated response of the electronics uses these files and the measured calibration constants. Furthermore, electronic noise and background due to synchrotron radiation is taken into account. Since a realistic simulation of the electronic noise of each individual channel in the liquid argon calorimeter is essential for the acceptance calculation for events with low energetic photons, the noise levels are generated according to the measured electronic noise of each of the more than 10000 channels in the various run ranges.

Finally, the simulated events are written to tape in a format that is identical to the raw data format of the measured events. The Monte Carlo events, therefore, can be treated in the same manner as the data events by the reconstruction program and the analysis chain following.

4.3 Trigger Simulation

A very important aspect of the event simulation is the analysis of the trigger decision, since trigger thresholds contribute to a large extent to the overall acceptance. This is especially true for two-photon reactions. The trigger system and the trigger conditions have already been described in section 3.2.1. From data it is known that most events are triggered by trigger 16. A precise simulation of for instance its opening angle condition is necessary. Hence, the charged part of the trigger is simulated in the same fashion as done in the experiment. The r_z and r_φ -masks are read in and compared to the hit pattern in the central detector. For the neutral part of the trigger logic the energy deposits in the respective calorimeters are taken. Since the requirement of the detection of an energy deposit in the forward or end cap calorimeter together with a single track reconstructed in r_φ and z in the inner detector is much easier met than the condition for two reconstructed tracks with a specific opening angle, tagged events are far more often triggered than untagged events. The trigger rate for untagged events with two tracks and one or two photons is of the order of 35 %, while events with a tag are triggered with an efficiency above 80 %.

The trigger simulation program is quite precise as can be checked by running the same program on data events. Here 96.5 % of all triggers are verified while only 2 % of all events not containing a specific trigger are wrongly assigned one. This remaining discrepancy is taken as the systematic error due to trigger simulation.

The events are then passed through the same filter program which ran directly after the data acquisition. Nearly all triggered events pass this filter stage, whereby tagged events again pass with a higher rate (99.5 %) than do untagged events (94%).

4.4 Evaluation of the Radiative Width of Resonances

The luminosity L is a proportional constant that relates the cross section σ of a reaction with the observed counting rate:

$$\frac{dN}{dt} = L \cdot \sigma \quad (4.7)$$

The value of this constant at a collider is dependent on the beam currents, the beam cross section, its revolution frequency and the number of bunches per beam. Since the parameters are not easy to control, it is common to determine the time integrated luminosity $\mathcal{L} = \int L dt$ with a monitor reaction. The elastic e^+e^- -scattering (Bhabha scattering) is especially suitable since its cross section can be calculated exactly in QED, its signature in the detector is unique and nearly background free, and the statistical error of the measurements are minimized due to the large cross section in comparison to all inelastic processes.

The systematic error is lowest ($< 3\%$) in the central region of the detector. The total amount of data taken in 1986 and available for the analysis corresponds to an integrated luminosity of $\mathcal{L} = 86pb^{-1}$ [42].

For a specific resonance the number of events produced throughout that year is therefore: $N_{pro} = \mathcal{L} \cdot \sigma$. Including the detector acceptance $DA (= N_{obs}/N_{pro})$ and the branching ratio $B(R \rightarrow X)$ of the resonance decaying into the final state X , only a small fraction of these events are actually observed:

$$N_{obs} = \mathcal{L} \cdot \sigma(e^+e^- \rightarrow e^+e^-R) \cdot DA \cdot B(R \rightarrow X) \quad (4.8)$$

A similar equation is valid for the number of observed Monte Carlo events. Here, the luminosity is given for a resonance with a radiative width of 1 keV (see eq. 4.1) and a branching ratio of 1 into the final state X . Hence, the radiative width of the resonance under study is given by the following expression:

$$\Gamma_{\gamma\gamma}(R) [keV] = \frac{N_{obs}}{N_{obs}^{MC}} \cdot \frac{\mathcal{L}_{MC}}{\mathcal{L}_{data}} \cdot \frac{1}{B(R \rightarrow X)} \quad (4.9)$$

If the Monte Carlo events are weighted with the ratio $(\mathcal{L}_{data} \cdot B(R \rightarrow X))/\mathcal{L}_{MC}$, the radiative width can directly be taken from the ratio of the observed number of data and MC events.

Chapter 5

Event Selection and Improvements of the Reconstruction Software

This chapter describes the criteria for the selection of events used in all following analyses. The final states under study are $\pi^+\pi^-\gamma$, $\pi^+\pi^-\pi^0$ and $\pi^+\pi^-\eta$, whereby the π^0 and η decay into two photons. Thus, events with two charged particles and at least one neutral particle have to be selected for these decay modes. Furthermore, the decay of the η' -meson into $\pi^+\pi^-\eta$ is studied where the η decays into the two major charged modes $\pi^+\pi^-\pi^0$ and $\pi^+\pi^-\gamma$. For this final state a data sample with 4 charged tracks has to be selected.

5.1 Selection of $\pi^+\pi^-N\gamma$ events

The data selection for the final states mentioned above starts from the preselection tapes (SELGGEX) described in section 3.2.5. To single out events with two tracks that result from two-photon interactions, the following cuts have to be applied on account of the inner detector information:

In a first stage exactly two tracks are demanded, where one must be identified to come from a positively charged, the other to come from a negatively charged particle¹. None of these particles may have a momentum of more than 10 GeV. This requirement rejects most of the radiative and non-radiative annihilation events still present at this selection stage. The two tracks must show an acollinearity (angle between the two tracks in space, see Fig. 5.1) and acoplanarity (angle between the two track in the $r\varphi$ -plane) of more than 2° . In addition, a missing transverse momentum is demanded of at least $p_t^2 > 0.005 \text{ GeV}^2$ to allow for photons in the final state. To reject events with unreconstructed tracks coming from the interaction point, no more than 5 hits are allowed in the 8 innermost chambers in any of the 12 sectors defined for this purpose. The above cuts remove about 78 % of the events collected on the exclusive two-photon selection tapes. Out of the 1.3 million events on the SELGGEX tapes 294000 remain at this first stage.

In a second stage only those events are kept which have at least one unlinked energy cluster in the lead liquid argon calorimeters or in the hole tagger counter. About one third of the events survive these cuts.

All these cuts can be applied using the standard CELLO reconstruction software developed for multihadron and exclusive annihilation events. For the special needs of reconstructing

¹Due to noise that fakes additional hits close to the track sometimes one track is reconstructed twice with nearly identical track parameters. The track with the more complete information is kept, the other discarded.

number of events (arbitrary units)

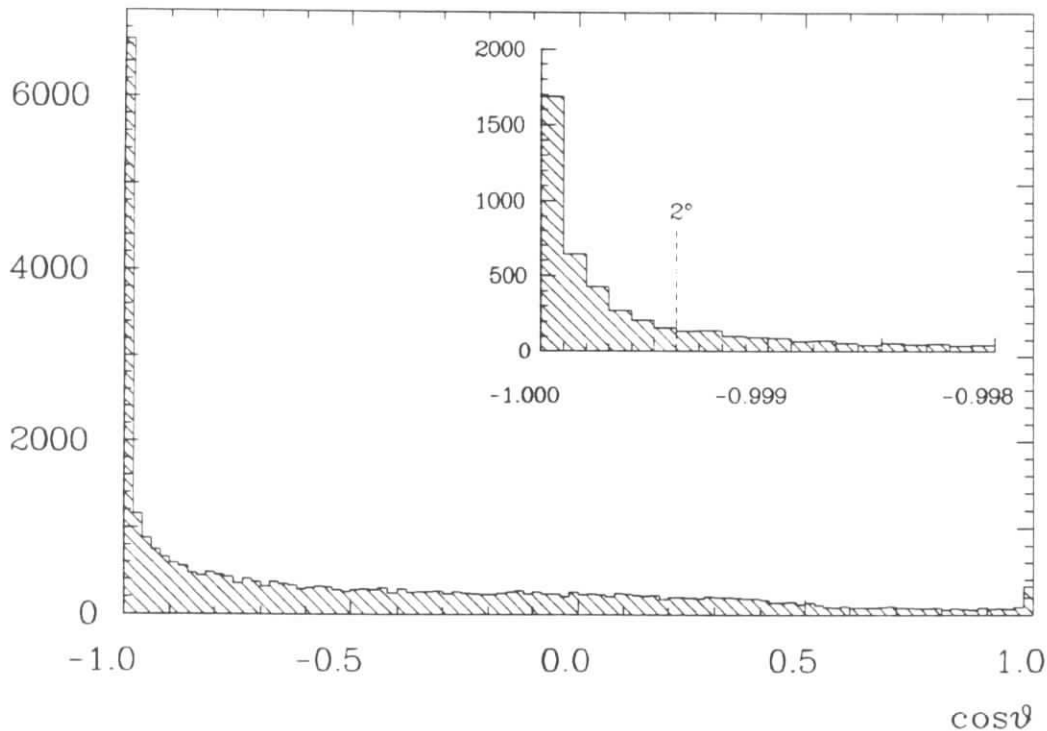


Figure 5.1: $\cos \vartheta_{\pi\pi}$ -distribution between charged tracks.

low multiplicity two-photon events the program package VIOLA has been developed by the CELLO two-photon group [43]. The main program contains several modules each of which evaluate the information present in the various detector components. There are modules that decode the information of the forward calorimeter or the hole tagger counter. Another module grades charged tracks according to their track parameters and to the number of hits on the track, and calculates a common event vertex of all accepted tracks in the event. A detailed secondary vertex search and reconstruction is performed to identify decays of converted photons, K_S^0 - or Λ -particles [35,44]. Furthermore, a particle identification for charged particles down to energies well below 1 GeV is achieved in the liquid argon calorimeters by a comparison of the longitudinal and lateral energy deposits of the particles with a set of norm showers [28]. Yet another module identifies collections of hits in the inner detector not attributed to any track by the standard reconstruction program. These hits, in general, stem from tracks not coming from the interaction point, such as backscattering particles or particles from decays. Showers that are created by these particles are removed from the photon sample and linked to the tracks. A set of routines performs an improved linkage of

cuts for charged particles		
$ p_{\pi^\pm} $	$<$	10 GeV
$\cos \vartheta_{\pi^+\pi^-}$	\geq	-0.9994
$\cos \varphi_{\pi^+\pi^-}$	\geq	-0.9994
$(p_t^{miss})^2$	\geq	0.005 GeV^2

Table 5.1: Selection cuts for charged particles. These cuts primarily reject annihilation background and exclusive 2-prong events.

information from the various detector components, taking into account the energy leakage from one component to the other – thus, the program prevents double counting of showers created at the borders between forward and end cap calorimeter, end cap calorimeter and hole tagger, hole tagger and barrel calorimeter – as well as the scattering or decay of particles in the magnetic coil of the CELLO detector.

Special care has been taken to identify genuine low energetic photons and distinguish them from noise. The noise structure for each individual electronic channel has been monitored and taken into account at the time of reconstruction. On these grounds a set of criteria (cf. next section) is applied to judge the quality of energy clusters in the liquid argon calorimeter and if these criteria are passed such a cluster is called a *photon*.

All particles accepted by VIOLA are filled into four-vectors which allow an easy handling of the events. For all other information that is not identified as noise a flag is set to distinguish between truly exclusive and not fully reconstructed events.

This program is now applied to the data. Hereby, an adaption of the value of the magnetic field of the coil² and a new calibration of the liquid argon calorimeter for showers below 500 MeV was included. This energy region is especially interesting for the reactions analysed in this thesis. The average energy of photons from η' -decays is of the order of 250 MeV for untagged reactions and roughly 100 MeV higher in the single tag mode. Therefore, the barrel and end cap part of the calorimeter are recalibrated using γ 's from the η' -decay and low energy electrons stemming from converted photons. The calibrations from both methods agree quite well and result in an improved resolution for various observed states.

Nevertheless, the photon energy stays the quantity measured with the lowest precision and kinematical fits or constraints have to be used to achieve an improved mass resolution of the final state spectrum, as will be shown later. While this can easily be done for events with no tags, the knowledge of the exact position and energy of the scattered lepton is crucial for the reconstruction of single tag events. An energy deposition of more than 5 GeV in the end cap calorimeter is required for a tag to be accepted by VIOLA. In the forward calorimeter the threshold is lower to clearly separate an untagged from a tagged event. The energy deposition has to be lower than 1 GeV for an event to be accepted as untagged, an energy above 2 GeV qualifies for a tag (5 GeV for a good tag). Events with a measured tag energy between these values are discarded.

Events containing at least one photon are then separated into different samples according to the number of tags and photons. The number of events in each sample can be found in the following table.

class	untagged	single tag
2 tracks 1 photon	20967	5034
2 tracks 2 photons	6932	1449
4 tracks n photons	–	3539

²It proved to be necessary to reduce the value of the magnetic field by 1.5 % in the reconstruction program for data events to avoid mass shifts in the invariant mass spectra of resonances of the order 10 MeV observed in previous analyses. The correction was determined using inclusive $K_S^0 \rightarrow \pi^+\pi^-$ from two-photon reactions and non-radiative μ -pairs from annihilation.

5.2 Selection of $\pi^+\pi^-\pi^+\pi^-N\gamma$ events

For the analysis of the decay $\eta' \rightarrow \pi^+\pi^-\eta \rightarrow \pi^+\pi^-\pi^+\pi^-(\pi^0/\gamma)$ it is not necessary to detect and identify the photons from the η -decay. Thus, the selection of the data sample can be done solely on the ground of the inner tracking detector information. Starting point for the selection are the same SELGGEX-tapes already used for the previous selection.

First a data sample with four charged tracks (2 positive and 2 negative) is produced. Second, a data sample is created which contains events with 2 and 3 tracks and at least 2 and 1 track candidates, respectively. These track candidates are identified by a routine that searches for a collection of unassigned hits in the innermost chambers in predefined sectors. It is the same routine that was used in the previous selection to reject events that still contain unreconstructed track candidates. This time these events are subjected to a modified version of the reconstruction program. Due to the very stable beam conditions in the 1986 data taking period, the events are very clean and seldom contain hits in the inner detector chambers not stemming from genuine tracks of the event. Thus, the reconstruction criteria could be loosened substantially. Instead of demanding a full reconstruction in z (which would require a certain p_t of the particle to reach 3 out of the 5 z -chambers) tracks are also accepted with only one z -point from the inner detector plus the common z -vertex from the other tracks in the events [45]. In order not to collect too many fake tracks at least 5 points with no hit missing inbetween is required for a good track. This way tracks down to a momentum of 60 MeV can be reconstructed and the statistics for four charged particle final states is increased by about 50 %.

Events with exactly 2 positive and 2 negative tracks after this additional reconstruction are merged with the above data sample. This sample of events is now processed by the VIOLA program. Out of 43000 events at that stage 3600 events are triggered by the relevant triggers 5, 15, 16, 7 or 10, and have a tagged lepton with an energy larger than 2 GeV.

5.3 Photon Selection Criteria

Due to the fine segmentation of the lead liquid argon calorimeter, a multitude of information is available on every shower [46]. This information is used to clearly separate photons from noise or other neutral particles. A precise knowledge of the noise pattern is however essential for this task. This was achieved by identifying hot and dead channels in the liquid argon calorimeter throughout the whole experiment. For each channel the exact position and form of the pedestals and their run dependance is monitored. This information is available to the reconstruction program LATRAK described in section 3.2.4. Nevertheless, a small fraction of channels still show some noise, which must be identified and rejected. Photon candidates in the barrel and end cap calorimeter are subjected to special cuts, comparing their longitudinal and lateral shower topology to norm-showers of a given energy. Furthermore, all those events are rejected where an identified photon is radiated off a charged particle, i.e. where the direction of the photon coincides with the track direction in any point of the track in the inner detector [47].

The criteria for accepting a photon are in particular:

- No established link to any track
- Relative amount of energy deposited in the first four layers must be larger than 30 %

- The shower centre of the photon has to be in the first half of the calorimeter
- Showers must have an energy deposition in at least two of the three projections in the calorimeter, independent of any other shower present in the same calorimeter module.
- The total number of strips fired must be greater than or equal to two. If this number is less than 5 at least 2 of the strips must have a pulse height 4σ above the respective noise pedestal.
- A detailed analysis is performed in the barrel and end cap calorimeters to make sure a shower is not created from noise and stray energy from another photon or track. A minimum distance is required between energy clusters in one projection, if they overlap in the projection perpendicular to the first. Otherwise the cluster with the least strips is rejected. No cuts are applied if the cluster has more than 6 strips in total or at least 3 strips in the other two projections. By this procedure existing ambiguities can be resolved in all cases, where two or more showers are in the same module.
- No energy cluster in the end cap liquid argon calorimeter is called a photon, if an identified tag is present in the same module.

5.4 Recalibration of the Forward Calorimeter

The angular resolution of the forward calorimeter proved to be insufficient for the needs of this analysis³. So here as well a recalibration of the components was conducted. As a calibration reaction tagged μ -pairs were taken. The φ -position of the tag can safely be predicted from the well measured tracks in the event. This predicted position is compared to the φ -value measured by the different components of the forward calorimeter.

For the positional measurement the information of the scintillator strips is the most crucial item. The pedestals for the strips are taken from those quadrants which are opposite to the actual tag in the event, the calibration constants are determined from the quadrant containing the tag. The measured pulse heights on both ends of the scintillator strips are related with the φ -position of the tag by the following expression:

$$\frac{PH_1}{PH_2} = \frac{c_1}{c_2} \exp(-2\delta r\varphi) \quad (5.1)$$

where the c_i are the calibration constants to be determined, δ the damping constant of the scintillator material and r the radius of the scintillator strip with respect to the beam axis. The logarithm of this ratio is then plotted against the predicted φ -position taken from the final state tracks. A fit [48] minimizing the linear distances of the measured fractions to a straight line at the same time determines the damping constants as well as the ratio of the calibration constants. For MC events the input values for the calibration constants are verified and all damping constants are equal within errors. For data events, however, no

³A kinematical fit does not improve the situation here as much as in the notag case. Together with the badly measured angular quantities in the forward spectrometer, we would have the insufficient energy resolution of the low energetic photons in the liquid argon calorimeter. Thus, the mass resolution of the final state cannot be improved. The same, unfortunately, is true for the Q^2 resolution of the tag itself. The situation is quite different if only charged particles make up the final state. Here the Q^2 resolution can considerably be improved by a kinematical fit (cf. ref. [35]).

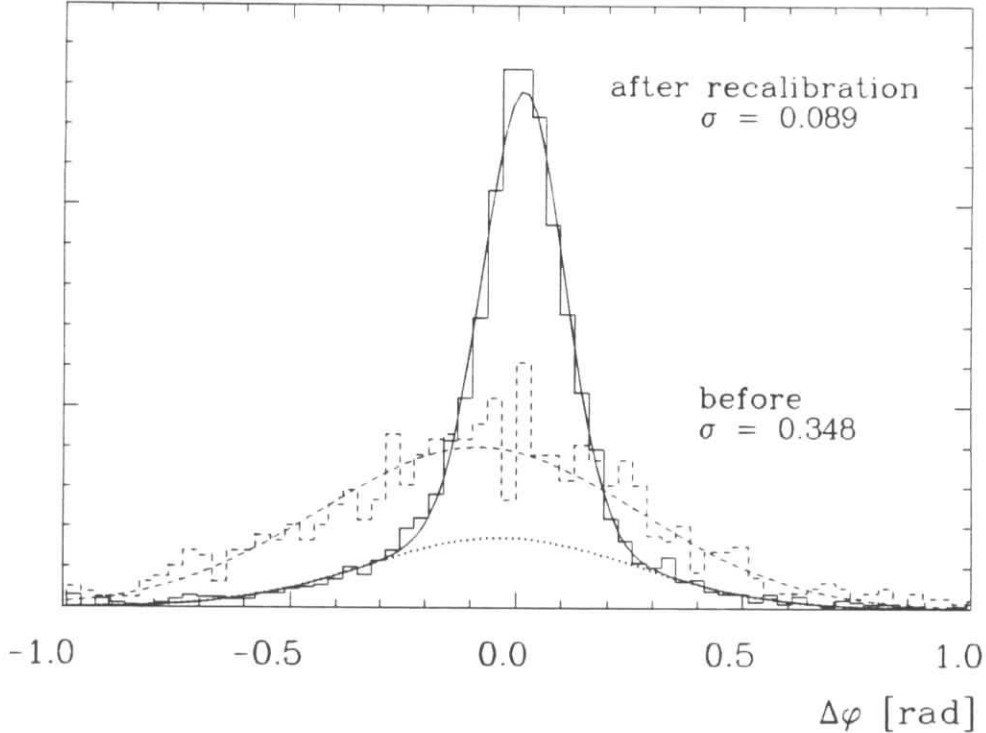


Figure 5.2: Result of the recalibration on the φ -resolution of tags.

unique value for the damping constants is found (this most likely shows the influence of aging of the scintillator material). Instead, the individual values are taken into consideration at the time of reconstruction. The φ -resolution ($\varphi_{\text{scintillator}} - \varphi_{\text{reconstructed}}$) of the combined scintillator information using the above technique improves from 350 *mrad* to 95 *mrad*. Together with a centre of gravity determination of the φ -position from the lead glass block [49] an overall resolution of 85 *mrad* is achieved – an improvement of a factor of 2.4 over the previous situation.

One of the major obstacles in the simulation of the forward calorimeter is the unknown precise amount of material below and in front of the calorimeter. In the central part of the calorimeter the energy deposits are reliably simulated as can be seen from the good agreement between measured and simulated energy spectra of Bhabha events. However, the distributions of energies in the full angular acceptance range of the forward calorimeter show a pronounced disagreement for low energies. The functional dependence seen between the tagging angle ϑ and the measured energy can be corrected for. However, it is not obvious that this will cure the whole problem. If the observed excess of low energetic showers over MC in the data is not due to miscalibration of the energy response but rather due to additional leakage into the calorimeter from below, one would introduce a bias in the overall normalisation. Therefore, the tagged data sample is later divided into two parts. One in the central region of the forward calorimeter and another one comprising data from the full region. It will be shown in chapter 7 that the results of the form factor measurements only slightly depend on this selection.

Chapter 6

Analysis of the Reaction $\gamma\gamma \rightarrow \eta' \rightarrow \rho\gamma$

The η' has been the first resonance observed in a two-photon reaction [50]. By now, a large number of publications exist on its production and decay into different decay channels. Very few of them, however, report on the measurement of the production form factor of this resonance. Although more than 14 measurements of the radiative width of the η' have been published or presented at conferences so far, there is still interest in further measurements or a reanalysis of older data for the different decay modes. The values quoted for the radiative width of this resonance cover the region from 3.8 keV to 6.2 keV. These results, however, are not consistent within their statistical errors (high statistics experiments tend to smaller values of the radiative width). Systematical effects seemingly play an important role and some of the early measurements might have underestimated their systematical errors.

The total width of this resonance ($\Gamma_{\eta'} = 0.24$ MeV) is so small in comparison to its mass ($m_{\eta'} = 957.57$ MeV) that the observed resonance shape is dominated by the experimental resolution. The observation and analysis of this resonance, as a side effect, therefore provides a nice tool for checking the performance of the apparatus.

The scope of the following sections is an attempt for a bias-free analysis of the decay $\eta' \rightarrow \rho\gamma$ by applying as few cuts as possible to identify and select this very channel. In the first section to come, the selection cuts for this channel will be described. From these data the radiative width is determined. The value obtained is discussed in the section following and compared to the values obtained by other experiments.

6.1 Determination of the Radiative Width of the η'

The data sample with two charged tracks and one photon is taken as a starting point for the analysis of η' -production in untagged two-photon reactions. The decay of the η' into $\rho\gamma$ with $\rho \rightarrow \pi^+\pi^-$ is the only decay channel which is triggered with a non-negligible rate in the CELLO detector in the untagged mode. The pions from the ρ decay have a momentum of 358 MeV in the ρ -centre-of-mass at nominal ρ mass. If emitted under angles large enough, this is above the threshold of $p_t > 250$ MeV demanded by the trigger masks (see section 3.2.1).

Tracks that go into the very forward direction only pass a very limited number of chambers in the central detector and use additional information supplied by the end cap proportional chambers. These tracks are not so well reconstructed and are therefore omitted from the following and all subsequent analyses.

Plotting the invariant mass $m(\pi^+\pi^-\gamma)$, already at this stage an η' -signal can be seen

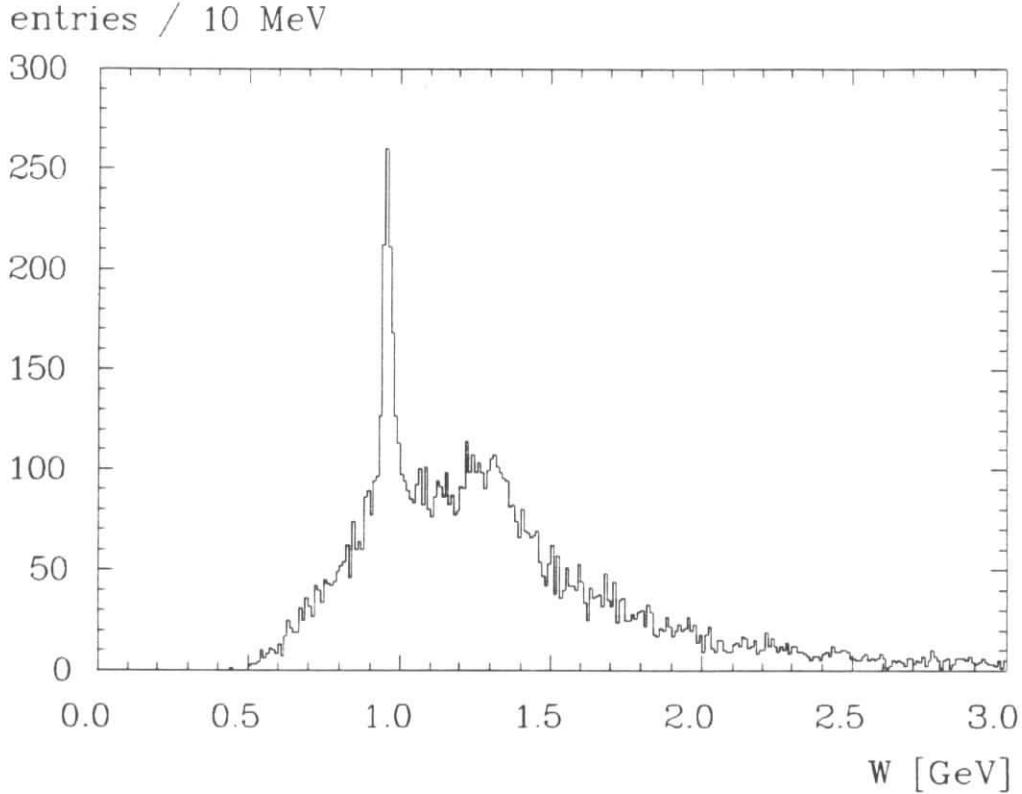


Figure 6.1: Invariant $\pi^+\pi^-\gamma$ -mass spectrum after SF correction

above a sizeable background. The resolution of the signal can drastically be improved using the fact that all truly exclusive reactions in the untagged mode should have a balanced transverse momentum. The badly measured energy of the photon can be replaced by a value calculated from the well measured track momenta and the angle between the $\pi^+\pi^-$ -system and the photon. Multiplying the photon energy by the scale factor SF will put the transverse momentum parallel to the $\pi^+\pi^-$ direction to zero and at the same time will minimize the overall event transverse momentum. The value of the scale factor is given by:

$$SF = \sqrt{\frac{p_t^2(\pi\pi)}{p_t^2(\gamma)}} \cdot |\cos \varphi(\pi\pi, \gamma)| \quad (6.1)$$

The invariant mass spectrum after applying this correction is shown in figure 6.1. Clearly seen is an η' -signal with about 1300 events and an $a_2(1320)$ -signal with about 1500 events. The latter stems from the decay $a_2 \rightarrow \pi^+\pi^-\pi^0$, where one of the photons from the π^0 -decay escapes detection. This reaction has already been analysed in detail elsewhere [74]. Here we only study this reaction as a source of background to the η' -signal. Since the η' -decay is fully reconstructed and reactions like the a_2 -decay are only partly reconstructed, the background level can drastically be reduced by applying a cut on the total transverse momentum of the final state. The recalculation of the photon energy allows us to cut at very small values of the transverse momentum. Values as low as $|\sum p_t|^2 < 0.001 \text{ GeV}^2$ can be chosen. The total transverse momentum spectrum with this cut value is shown in figure 6.2.

For the determination of the radiative width of the η' from its decay into $\rho\gamma$ it is necessary to identify the ρ . It has been known for a long time that the ρ -spectrum in this decay cannot be described by a simple Breit-Wigner function, since the spectrum is bound from below by the $\pi\pi$ -threshold and from above by the η' -mass. Taking into account the correct description

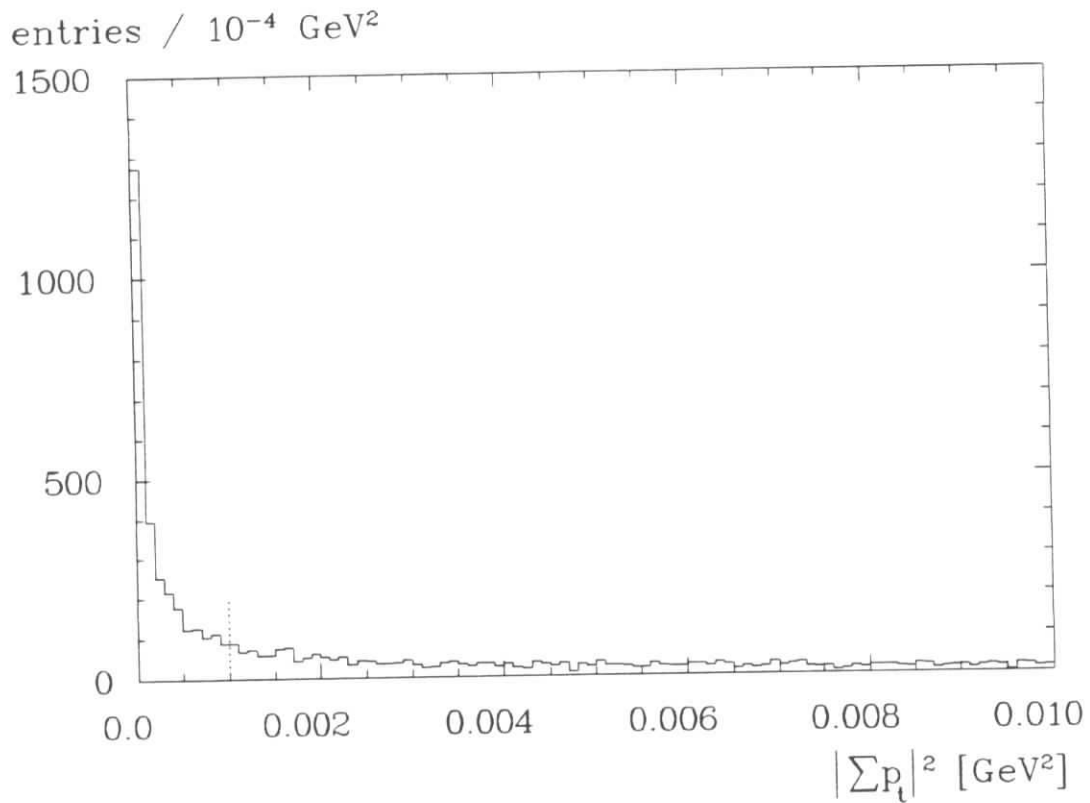


Figure 6.2: p_t^2 -spectrum after recalculation of the photon energy.

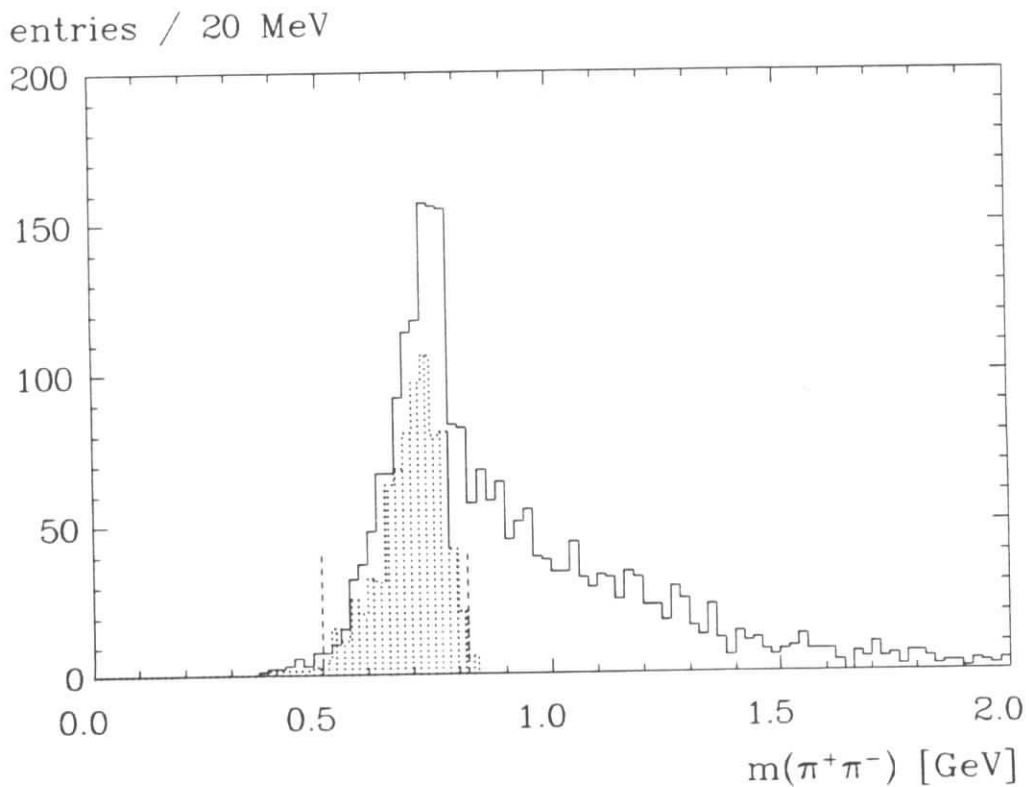


Figure 6.3: Invariant $\pi^+\pi^-$ -spectrum of events after SF-correction and a cut in the total transverse momentum of the event of $|\sum p_t|^2 < 0.001 \text{ GeV}^2$. The shaded histogram is the MC expectation for the ρ -shape normalized to $\Gamma_{\gamma\gamma} = 3.62 \text{ keV}$. The dashed lines mark the ρ -band cut values.

[24] of the $\pi\pi$ -phase space and the matrix element (see section 2.5), the ρ -spectrum is shifted towards smaller invariant masses and takes an asymmetric form. For selecting events in the ρ -band we choose the following mass range:

$$\rho\text{-band} : 0.50 \text{ GeV} < m(\pi\pi) < 0.82 \text{ GeV} \quad (6.2)$$

The invariant $\pi\pi$ -mass spectrum with a $|\sum p_t|^2$ -cut of 0.001 GeV^2 is shown in fig. 6.3 together with the MC expectation (dashed histogram) for the process under study, and the above ρ -band cut values.

Counting the number of events. To calculate the radiative width of a resonance the number of events in the signal region has to be compared to the number of MC events expected in the same region. This is most easily done if no background is present underneath the signal or the level of background can safely be predicted by counting the number of events in sidebands where no signal is expected. A clean data sample with as little background as possible is favoured for such an approach. To get a handle on differences in the acceptance of the various detector components, the data sample is split according to the calorimeter the photon is detected in. The course of the analysis will first be described for the data sample where the photon is detected in the barrel calorimeter. Here we expect most of the events. The analysis of the end cap calorimeter sample, following the same line, will then be presented in less detail.

Commonly a cut in the photon energy is applied to reject showers created by noise still present in the data. In the barrel calorimeter we choose a value of 130 MeV for this cut. The mass spectrum of the remaining events with (shaded histogram) and without (solid line histogram) ρ -band cut is shown in figure 6.4. To calculate the radiative width $\Gamma_{\gamma\gamma}(\eta')$ the number of events in the signal region (0.92 - 1.00 GeV) has to be determined. The background still present under the signal is estimated from two sidebands (0.76 - 0.84 GeV and 1.08 - 1.16 GeV) far away from the resonance. With 716 events found in the signal region and 96 events in the sidebands the number of η' -candidates is 668 ± 27 . The error is purely statistical and is given by the square root of the number of events in the signal region before background subtraction. The effect of the sideband subtraction will be accounted for in the final systematical error. The same procedure for the MC events (normalized to the data luminosity \mathcal{L} of 86 pb^{-1} and to a branching ratio $B(\eta' \rightarrow \rho\gamma)$ of 30.1 % [17]) gives 183.4 events. The systematical uncertainty of background subtraction is estimated to be less than 4 %. These numbers translate by virtue of eq. 4.9 into a radiative width $\Gamma_{\gamma\gamma}$ of:

$$\Gamma_{\gamma\gamma} = 3.62 \pm 0.15 \text{ keV} \quad (6.3)$$

Since a cut in the photon energy might introduce some bias if the shapes of the energy distributions do not quite agree between data and MC, a systematic study has been performed. The energy spectra of the signal and side band regions have separately been obtained for data and MC. A simple subtraction of the side band spectra, however, does not take into account the reduced (increased) amount of phase space available for the respective side bands in comparison to the signal region. Therefore negative entries occur on both ends of the photon energy spectrum. The background subtracted energy spectra are shown in fig 6.5. A division of the integrated spectra will directly give the dependence on a lower energy cut if the integration is performed from right to left. Figure 6.6 on the left hand side shows this dependence on the energy cut while the right hand side of this figure shows the result of

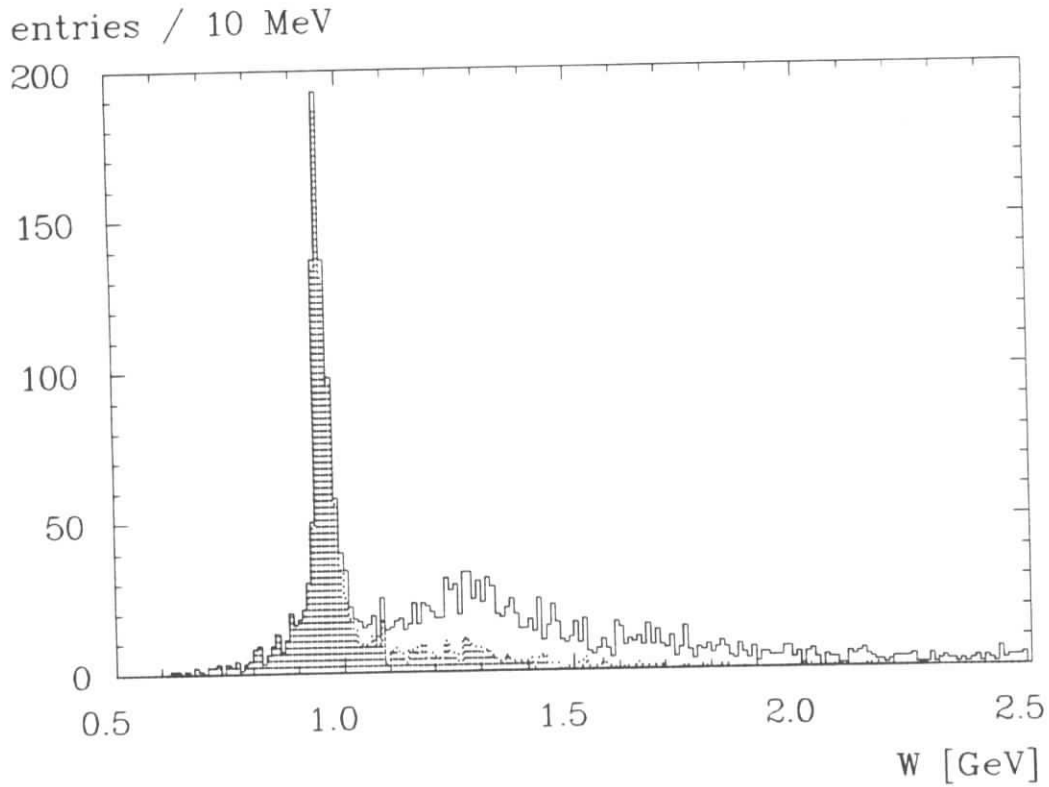


Figure 6.4: Invariant $\pi^+\pi^-\gamma$ -mass spectrum with $|\sum p_t|^2 < 0.001 \text{ GeV}^2$ and $E_\gamma > 130 \text{ MeV}$. The dashed histogram marks events in the ρ -band.

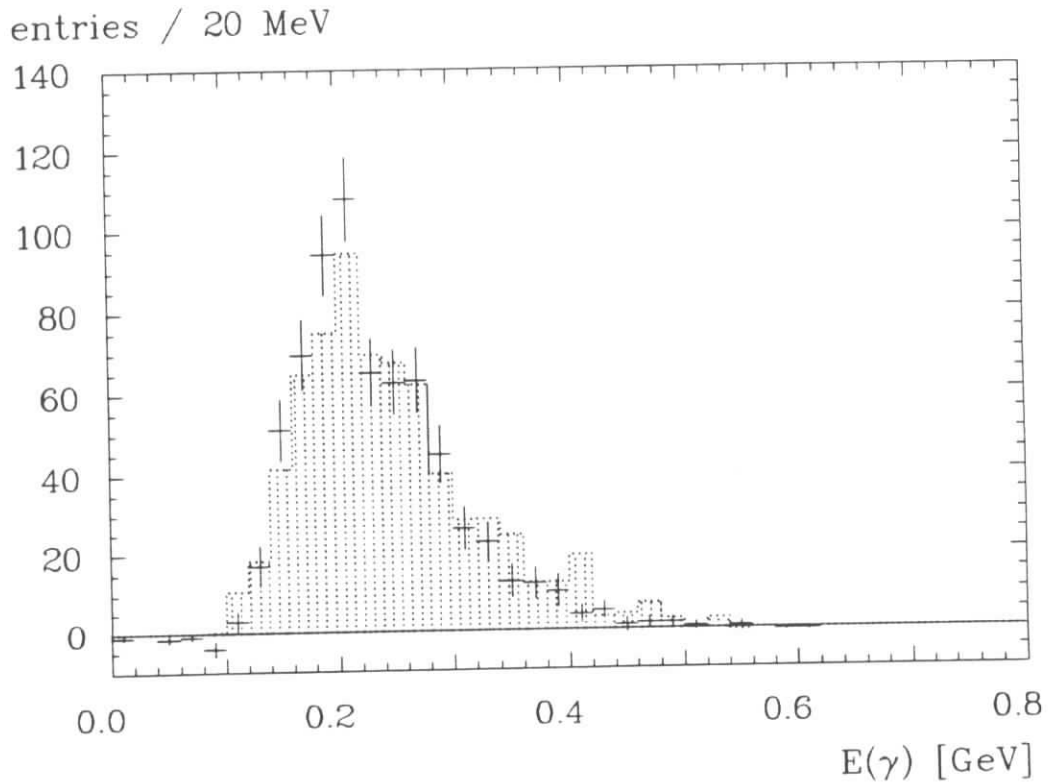


Figure 6.5: Photon energy spectrum after background subtraction. The crosses mark the data events and the shaded histogram the MC expectation for a radiative width $\Gamma_{\gamma\gamma}(\eta') = 3.62 \text{ keV}$.

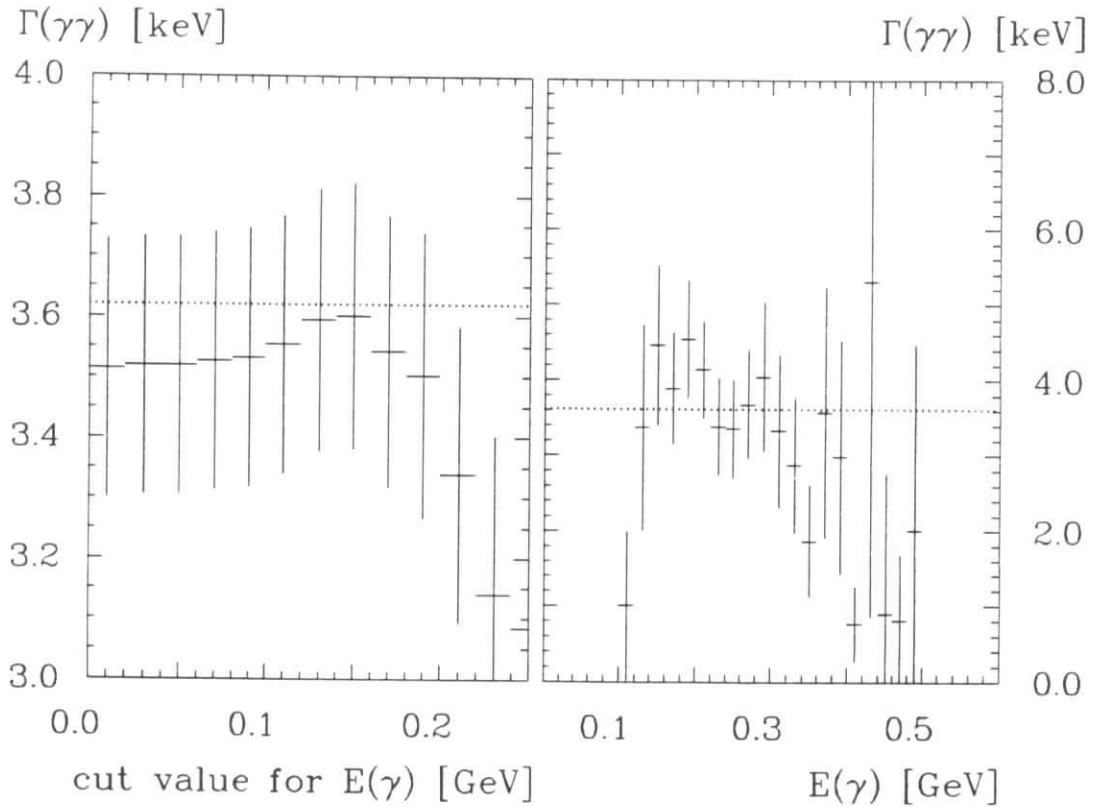


Figure 6.6: Effect of lower photon energy cut on the radiative width $\Gamma_{\gamma\gamma}$ (left figure). The figure on the right hand side shows the result of a determination of $\Gamma_{\gamma\gamma}(\eta')$ in bins of the photon energy of 20 MeV.

the division of the energy spectra itself. This latter is equivalent to a determination of the radiative width in certain bins of the photon energy. The highest values occur in the centre of the photon spectrum while the results from both flanks are considerably lower. Nevertheless, all results agree within their statistical errors. The systematic effect on a lower cut value on the photon energy is estimated to be of the order of 4 % towards lower values from the one quoted above. The same procedure can be repeated with a full kinematical fit of the final state system requiring p_t -balance. The results obtained are systematically 4 % higher for every photon energy cut value selected.

In the end cap calorimeter the same technique is applied to obtain the radiative width of the η' . The statistics is about a factor of 7 lower than in the barrel calorimeter. Here, only 99.0 ± 11.7 events are observed (22.8 in MC), leading to a radiative width of:

$$\Gamma_{\gamma\gamma} = 4.34 \pm 0.51 \text{ keV} \quad (6.4)$$

The combined result for the barrel and end cap calorimeter sample is obtained by a weighted average of the two results:

$$\bar{x} \pm \delta\bar{x} = \left(\frac{\sum_i w_i x_i}{\sum_i w_i} \right) \pm \left(\sum_i w_i \right)^{-1/2}; \quad w_i = 1/(\delta x_i)^2 \quad (6.5)$$

The value is dominated by the statistically more significant result from the barrel calorimeter sample:

$$\Gamma_{\gamma\gamma} = 3.68 \pm 0.14(\text{stat.}) \pm 0.48(\text{syst.}) \text{ keV} \quad (6.6)$$

The second error quoted is the systematical error. It is the sum of squares of the contributions from the luminosity determination (3 %), background subtraction (3 %), trigger simulation

(5 %), variation of the photon energy cut (4 %), the track reconstruction efficiency (4 %) and the photon detection efficiency (8 %), giving rise to an overall systematical error of 13 %. The branching ratio ($30.1\% \pm 1.4\%$) that is needed to calculate this number is known with a precision of 5 %. Its error is included in the above number.

A fit to the mass spectrum. Another way of determining the radiative width of a resonance is a fit to the invariant mass spectrum, using MC events to predict the shape of the resonances present in the spectrum and some parameterisation for the background shape. Since no full kinematical fit has been performed to produce the invariant mass spectrum under study (cf. figs. 6.1, 6.7), but rather a recalculation of the photon energy, the signals are not necessarily described by Gaussian resolution functions or Breit-Wigner functions folded with a Gaussian. Instead, the shape has to be taken from the MC simulation, where a sum of two Gaussians with different resolutions σ was found to give a good description of the MC invariant mass spectrum.

The η' -events were generated according to the procedure described in chapter 4 based on the cross section formula (eq. 2.40) in chapter 2. For generating a_2 -events results from our analysis [74] of the helicity structure have been used. A Breit-Wigner function with the mass ($m = 1.318$ GeV) and width ($\Gamma = 110$ MeV) of the $a_2(1320)$ taken from [17], modified by Blatt-Weisskopf form factors for helicity-2 production, has been used to generate the resonance for lepton scattering angles up to 50 mrad. The Q^2 -evolution of the form factor has been described by a simple ρ -pole.

The events are then subjected to various cuts. The first data sample contains events where no cuts have been applied, except the ones from the preselection described in chapter 5, a second data sample contains those that passed a transverse momentum cut of $|\sum p_t|^2 < 0.01$ GeV^2 , and a third those that passed the strong transverse momentum cut of $|\sum p_t|^2 < 0.001$ GeV^2 with photon energies above 130 MeV. For all these data samples the shape parameters of both resonances have been determined separately. Fixing the shape parameters and leaving only the absolute normalization free, the sum of the resonances plus a background is fitted to the data invariant mass spectrum. For the background shape three different parametrisations have been used: (1) $a * (x - b)^c * e^{dx + ex^2}$, (2) $a * (x - b)^c * (d - x)^e$ and (3) a third order polynomial. The second and third parametrisations were found to be numerically more stable, leading to a faster convergence of the fit. The parameter b in the first and the parameters b and d in the second describe the end points of the distribution and were held fixed during the fit. Varying these parameters has a maximum impact on the resulting η' -radiative width of 3 %. The third parametrisation does not contain such parameters and can be used to cross check the results. Fixing the end point parameters of the second function at $b = 0.5$ and $d = 3.5$ yields results that are identical to the results obtained with the third order polynomial for the last two data samples. Such a fit to the data spectrum with a $|\sum p_t|^2$ -cut of 0.01 GeV^2 can be seen in fig. 6.7. It was found that the integration range played a much stronger systematic role on the results than the parametrisation of the background shape, and therefore will be presented here. Figure 6.8 shows this dependence of the resulting radiative width for the η' on the upper bound of the fit range. The tendency to higher values of the radiative width with an increasing upper bound is easily understood by the fact that the background shape is primarily fixed by the values far away from the resonance region.

Since none of the data samples and none of the background parametrisations can be favoured, the final result has been obtained by averaging over the individual results. For the a_2 a radiative width of $\Gamma_{\gamma\gamma}(a_2) = 0.97 \pm 0.09(stat.) \pm 0.20(syst.)$ keV was found, which is

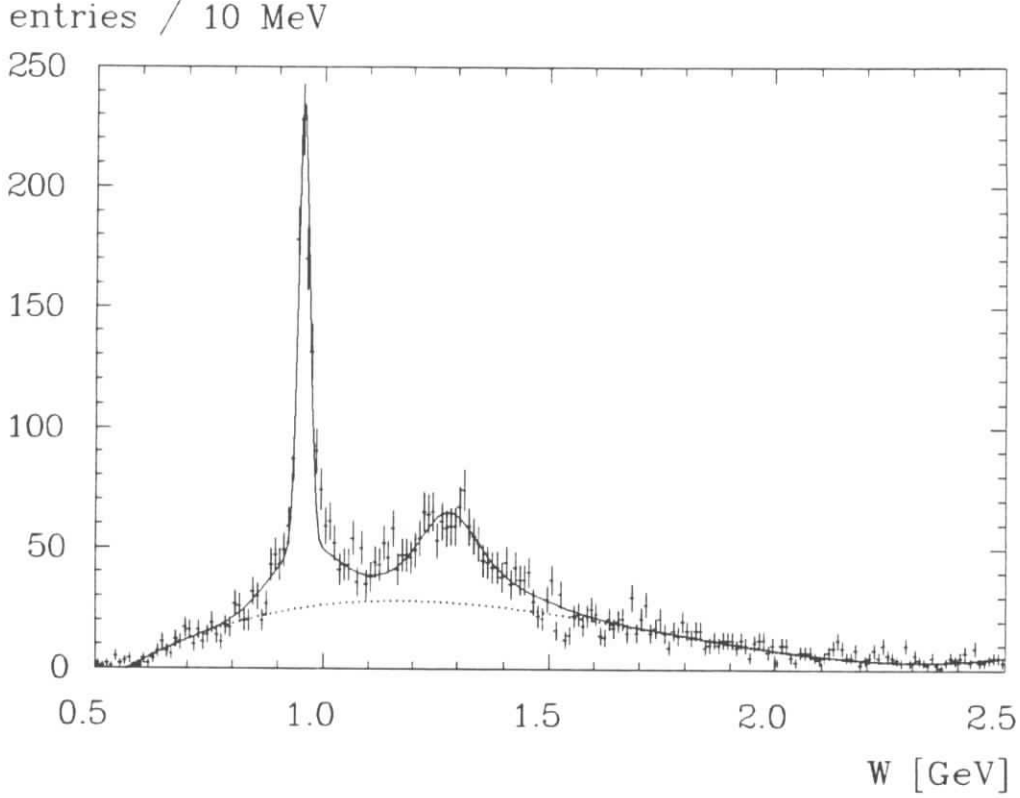


Figure 6.7: Invariant $m(\pi^+\pi^-\gamma)$ -spectrum with $p_t^2 < 0.01 \text{ GeV}^2$. Shown are the results of a fit to the data spectrum using the MC predicted shapes.

in good agreement with the result obtained by our previous analysis [74]. The systematical error given here, however, only includes the systematical effects from the fit procedure and denotes the *maximum* deviation from the mean value found. The corresponding result for η' -radiative width is:

$$\Gamma_{\gamma\gamma}(\eta') = 3.62 \pm 0.15(\text{stat.}) \begin{matrix} +0.23 \\ -0.19 \end{matrix}(\text{syst.}) \text{ keV} \quad (6.7)$$

Here as well, the systematical errors denote the *maximum* deviation found by varying the upper fit bound.

This result for the radiative width is in excellent agreement with the one found by the simple counting of η' -candidates. The systematic error determined here is a measure for the background shape and photon energy determination accuracy. It is well in accord with the 3% and 4% error estimated in the last section. Thus, the overall systematic error is determined to be 13%, including the error of the branching ratio.

The final number for the radiative width will be taken from the last determination since it comprises more systematic effects than the simple counting determination. To be independent from the actual value of the branching ratio and to quote only the errors present in this analysis, the radiative width is quoted as:

$$\Gamma_{\gamma\gamma} \cdot B(\eta' \rightarrow \rho\gamma) = 1.09 \pm 0.04(\text{stat.}) \pm 0.13(\text{syst.}) \text{ keV} \quad (6.8)$$

The systematic error of 12% contains the contributions from the luminosity determination (3%), trigger simulation (5%), photon detection (8%) and track reconstruction (4%) efficiency as well as the 6% error from the background parametrisation and photon energy cuts.

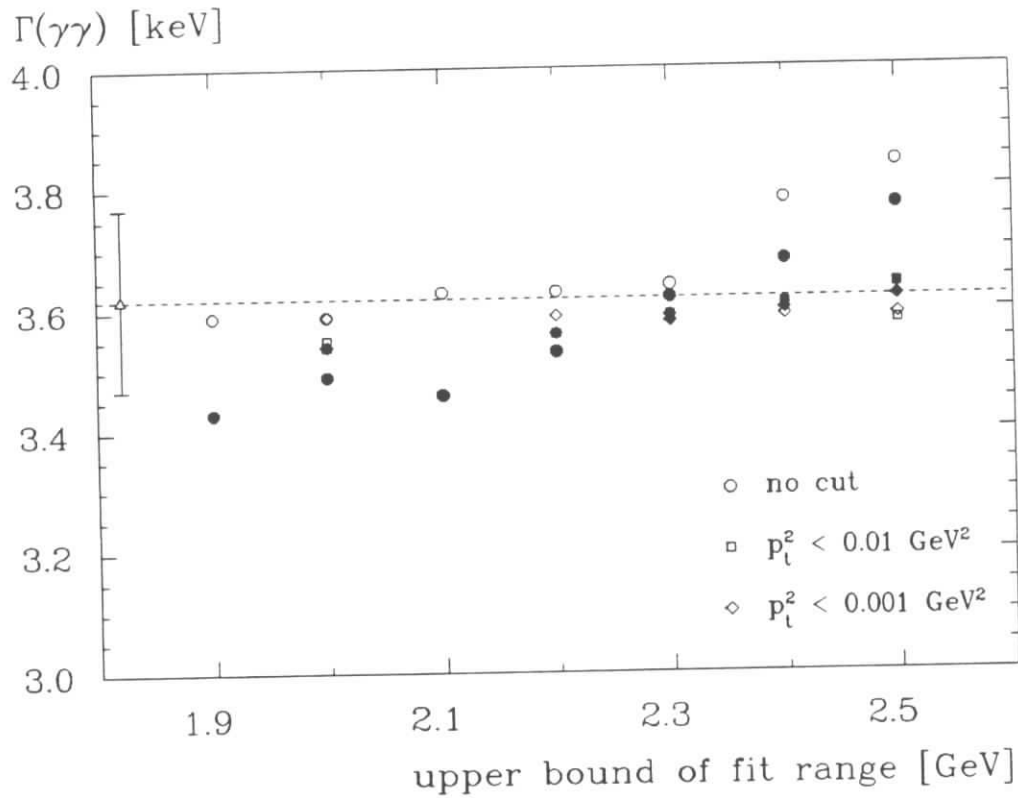


Figure 6.8: Dependence of the radiative width on the fit range. The lower bound is fixed to 0.55 MeV while the upper bound was varied between 1.9 GeV and 2.5 GeV. The white symbols are the result of a fit with the polynomial background, the black symbols use the second parametrisation (see text).

6.2 The ρ -Mass Spectrum and Decay Angular Distribution

The electromagnetic decay of the $\eta' \rightarrow \rho\gamma$ is a magnetic dipole transition with a partial decay rate described by equation 2.54. Starting from the selection of events shown in fig. 6.4 it is interesting to study whether the ρ -mass spectrum and the decay angular distribution of the pions in the ρ -helicity frame are well described by the MC data generated according to this formula.

The η' events considered for this study have passed a transverse momentum cut of $|\sum p_t|^2 < 0.001 \text{ GeV}^2$ and have a photon with energy above 130 MeV after the scale factor correction. Since the η' has spin zero and the photon is massless the helicity of the ρ in the decay $\eta' \rightarrow \rho\gamma(0^- \rightarrow 1^-1^-)$ is restricted to ± 1 . This leads to a $\sin^2 \vartheta$ -distribution of the π -decay angle in the ρ -helicity frame. The $|\cos \vartheta_\pi^*|$ -distribution of this angle for η' -events is plotted in fig.6.9. In order to assure that only η' -events contribute to this plot, only events in the ρ -band have been taken. Furthermore the contributions from two sidebands (0.88-0.92 and 1.00-1.04 GeV) have been subtracted from the distribution in the η' -mass region (0.92-1.00 GeV). The data distribution is marked with crosses denoting the width of the $\cos \vartheta_\pi^*$ -bins and the statistical error on the number of entries in these bins. The MC prediction of this angle normalized to the measured radiative width of 3.62 keV is shown as a dotted line histogram. The agreement between the two distributions is very good, showing that indeed the ρ -meson is polarized in this decay.

The shape of the ρ is studied in the $\pi\pi$ -invariant mass spectrum obtained in a similar fashion. Again the contributions of the two sidebands are subtracted from the distribution gained in η' -mass region. However no ρ -band cut is applied this time. The resulting shapes of the ρ -mass distribution is shown in fig.6.10, the crosses mark the data entries and the dotted line histogram the MC predicted shape and normalization for a radiative width of 3.62 keV. The agreement between the curves is good, maybe there is little excess of data events on the right flank accompanied by a little excess of MC events on the left flank. This distortion of the shape has also been observed by the PLUTO [53], ARGUS [58], TASSO [54] and TPC/2 γ [56] collaborations. Other collaborations, however, do not observe this effect. The effect is certainly small and only a combined analysis of acceptance corrected spectra could yield a definite answer.

6.3 Discussion of the Results and Comparison to Other Experiments

The resulting radiative width of 3.62 keV is one of the lowest obtained so far. Other publications as well quote values below 4 keV. In table 6.1 an overview is given over all published values for the radiative width of the η' . One has to note that the quoted radiative widths were derived with different values for the corresponding branching ratios. To correct for possible changes of the branching ratio between the date of publication and now, the radiative widths have to be recalculated from the values for $\Gamma_{\gamma\gamma}$ times branching ratio. These values are taken directly from the publications or calculated from the branching ratios given in the paper. If none of these numbers is available, the branching ratio is taken from the latest issue of the *Review of Particle Properties* available at the time of publication. The radiative width is then recalculated using the branching ratios from the 1988 edition of this review [17]. The

number of events / 0.1

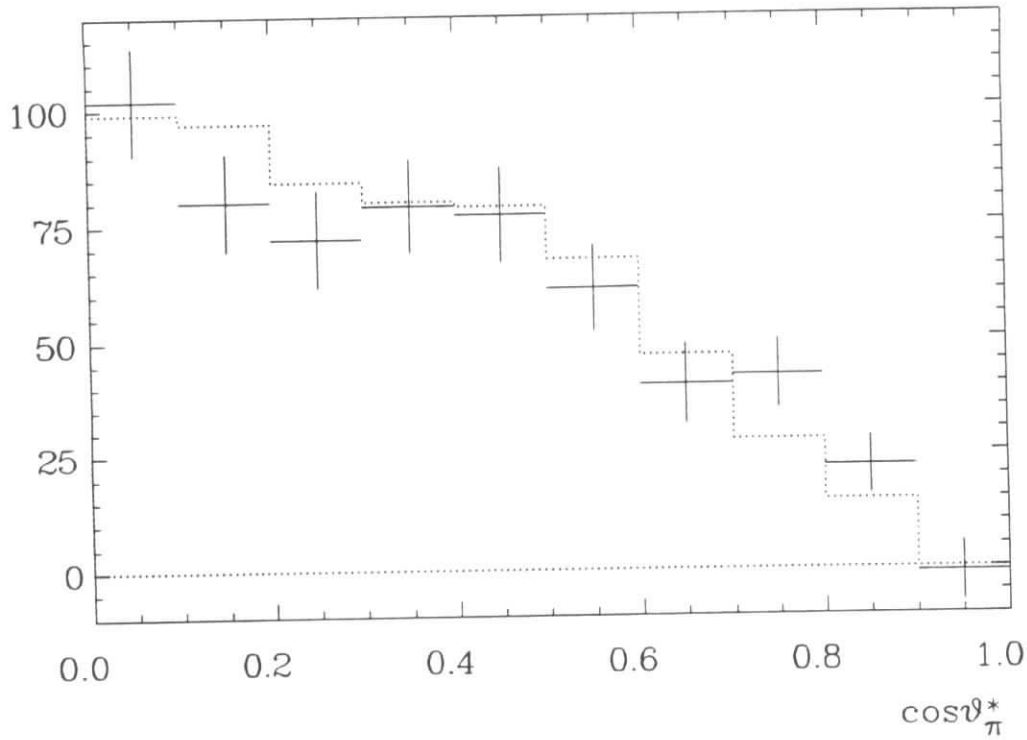


Figure 6.9: $|\cos \vartheta_\pi^*|$ -distribution. The crosses mark data points and the dotted line histogram the MC expectation for a radiative width of 3.62 keV.

entries / 20 MeV

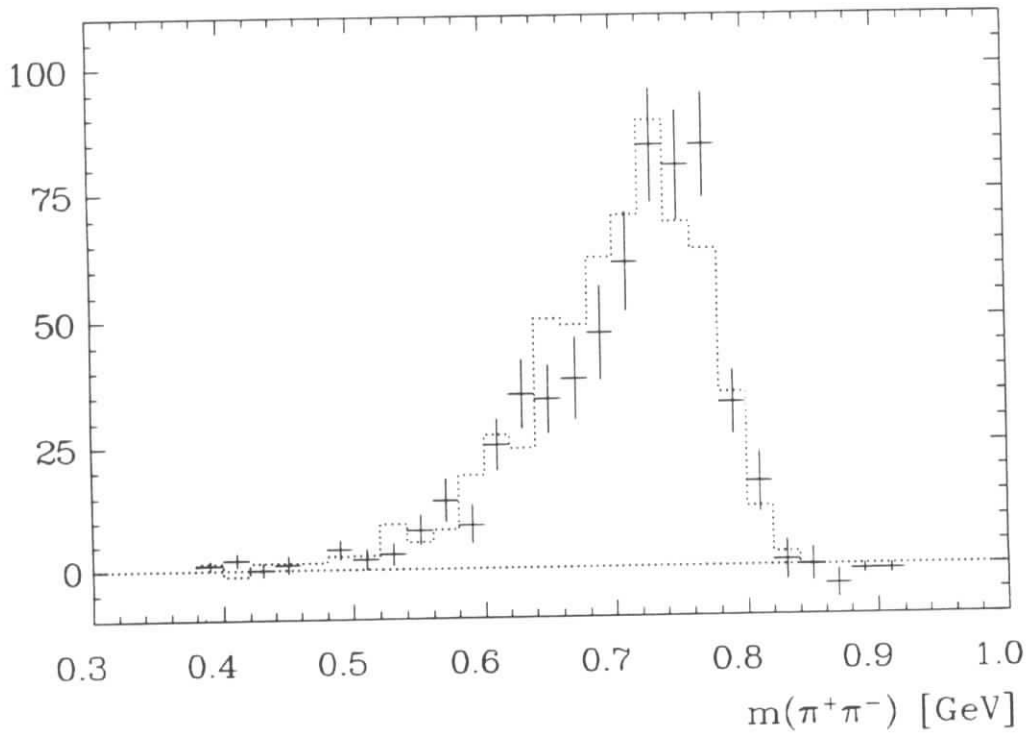


Figure 6.10: ρ -shape: The crosses mark the $\pi\pi$ -mass distribution for events in the η' -band (see text), the dotted line histogram is the MC expectation for a radiative width of 3.62 keV.

collaboration	year	mode	$\Gamma_{\gamma\gamma}$ [keV]	BR [%]	$\Gamma_{\gamma\gamma}^{corr}$ [keV]
MarkII ^f	1983 [50]	$\rho\gamma$	$5.8 \pm 1.1 \pm 1.2$	29.8 ± 1.7	$5.7 \pm 1.1 \pm 1.1$
JADE	1982 [51]	$\rho\gamma$	$5.0 \pm 0.5 \pm 0.9$	29.8 ± 1.7^a	$5.0 \pm 0.5 \pm 0.9$
CELLO	1982 [52]	$\rho\gamma$	$6.2 \pm 1.1 \pm 0.8$	29.8 ± 1.7^a	$6.1 \pm 1.1 \pm 0.8$
PLUTO	1984 [53]	$\rho\gamma$	$3.80 \pm 0.26 \pm 0.43$	30.0 ± 1.6	$3.79 \pm 0.26 \pm 0.42$
TASSO	1984 [54]	$\rho\gamma$	$5.1 \pm 0.4 \pm 0.7$	30.0 ± 1.6	$5.1 \pm 0.4 \pm 0.7$
JADE	1985 [55]	$\gamma\gamma$	$4.0 \pm 0.9 \pm 0.7^b$	1.9 ± 0.2^a	$3.5 \pm 0.8 \pm 0.5$
TPC/2 γ	1987 [56]	$\rho\gamma$	$4.5 \pm 0.3 \pm 0.7$	30.0 ± 1.6	$4.5 \pm 0.3 \pm 0.7$
ARGUS	1987 [58]	$\rho\gamma$	$3.76 \pm 0.13 \pm 0.47$	30.0 ± 1.6	$3.76 \pm 0.13 \pm 0.47$
MarkII ^g	1987 [59]	$\eta\pi^+\pi^-$	$4.7 \pm 0.6 \pm 0.9$	16.9 ± 0.5^a	$4.7 \pm 0.6 \pm 0.9$
Crystal Ball	1987 [60]	$\eta\pi^0\pi^0$	$4.6 \pm 0.4 \pm 0.6$	0.086 ± 0.008	$5.1 \pm 0.4 \pm 0.6$
MD-1 (prel.)	1987 [57]	$\rho\gamma$	$4.6 \pm 1.1 \pm 0.9$	30.0 ± 1.6^a	$4.6 \pm 1.1 \pm 0.9$
TPC/2 γ	1988 [61]	$\eta\pi^+\pi^-$	$3.8^d \pm 0.7 \pm 0.6$	$16.9 \pm 0.5^{a,c}$	$3.7 \pm 0.7 \pm 0.6$
Crystal Ball	1988 [62]	$\gamma\gamma$	$4.7 \pm 0.5 \pm 0.5$	2.23 ± 0.18	$4.8 \pm 0.5 \pm 0.5$
JADE	1988 [63]	$\eta\pi^+\pi^-$	$3.80 \pm 0.13 \pm 0.50$	17.2 ± 0.6^a	$3.80 \pm 0.13 \pm 0.50$
ASP	1989 [64]	$\gamma\gamma$	$4.96 \pm 0.23 \pm 0.72$	2.16 ± 0.16	$4.96 \pm 0.23 \pm 0.72$
MarkII (prel.)	1989 [65]	$\rho\gamma$	$4.61 \pm 0.32 \pm 0.60$	30.1 ± 1.6^a	$4.61 \pm 0.32 \pm 0.60$
MarkII (prel.)	1989 [65]	$\eta\pi^+\pi^-$	$4.37 \pm 0.62^{+0.98}_{-0.95}$	17.2 ± 0.6^a	$4.37 \pm 0.62^{+0.98}_{-0.95}$
MarkII (prel.)	1989 [65]	$\eta\pi^+\pi^{-c}$	$4.60 \pm 0.49^{+0.68}_{-0.96}$	12.6 ± 0.5^a	$4.60 \pm 0.49^{+0.68}_{-0.96}$
CELLO	this exp.	$\rho\gamma$	$3.62 \pm 0.15 \pm 0.47$	30.1 ± 1.4	$3.62 \pm 0.15 \pm 0.47$

^a value taken from PDG

^b systematical error estimated

^c η -decay into $\pi^+\pi^-(\pi^0/\gamma)$

^g results superseded by [65]

^d value was extrapolated from Q^2 -evolution to $Q^2 \rightarrow 0$

^e isospin fraction of 2/3 of $BR(\eta' \rightarrow \eta\pi\pi) = 65.2\%$ used

^f supersedes an earlier publication from 1979

Table 6.1: Compilation of published values for $\Gamma_{\gamma\gamma}(\eta')$. If not marked differently, all η -decays are observed in their decay mode $\eta \rightarrow \gamma\gamma$.

branching ratios used are listed in table 6.2.

On first sight there seems to be a clustering of radiative widths in two regions. One around values of 3.8 keV and the other one in the range between 4.5 and 6.2 keV. Is this clustering significant? An answer to this question can be given using a presentation of the results known as an *ideogram* [17]. It is a graphical representation of the sum of all results, where each individual measurement contributes with a Gaussian function of mean x_i , standard deviation δx_i and weight $1/\delta x_i$. Figure 6.11 shows such an ideogram based on the *statistical* errors given by the experiments. The full line is the sum of all Gaussians, while the broken lines represent the sums of the different decay channels. Based on the statistical errors only, a world average for the radiative width can be calculated from all the experiments using formula 6.5. The resulting radiative width is

$$\langle \Gamma_{\gamma\gamma} \rangle = 4.04 \pm 0.06(stat.) \text{ keV} \quad (6.9)$$

consisting of the results from the individual decay channels: 3.95 ± 0.08 keV ($\rho\gamma$), 3.97 ± 0.12 keV ($\eta\pi\pi$) and 4.84 ± 0.20 keV ($\gamma\gamma$). The first two decay modes clearly favour a value just below 4 keV, while the last decay mode results in a value closer to 5 keV. The central value of the $\gamma\gamma$ -decay mode is off the average by 4 standard deviations. If instead the standard way of determining a world average is taken, i.e. the quadratic addition of statistical and

channel	branching ratio	
$\eta' \rightarrow \eta\pi^+\pi^-$	44.1 ± 1.6	
$\eta' \rightarrow \rho\gamma$	30.1 ± 1.4	
$\eta' \rightarrow \eta\pi^0\pi^0$	20.5 ± 1.3	S=1.2*
$\eta' \rightarrow \gamma\gamma$	2.16 ± 0.16	S=1.4*
$\eta \rightarrow \pi^+\pi^-\pi^0$	23.7 ± 0.5	
$\eta \rightarrow \pi^+\pi^-\gamma$	4.91 ± 0.13	
$\eta \rightarrow \gamma\gamma$	38.9 ± 0.4	
$\pi^0 \rightarrow \gamma\gamma$	98.798 ± 0.032	S=1.1*

* scaled error see [17]

Table 6.2: η' , η and π^0 branching ratios from the *Review of Particle Properties*, 1988 [17]

systematic errors to weight the measurements, the discrepancy is not as big:

$$\langle \Gamma_{\gamma\gamma} \rangle = 4.27 \pm 0.17(stat + syst) \text{ keV} \quad (6.10)$$

with 4.22 ± 0.22 keV ($\rho\gamma$), 4.23 ± 0.34 keV ($\eta\pi\pi$) and 4.56 ± 0.45 keV ($\gamma\gamma$). The same effect is seen in the ideogram (fig.6.12) when systematic and statistical errors are added quadratically. The resulting shape does not show the two distinct peaks at 4 and 5 keV. This seems to be an indication that systematic effects already taken into account by the experiments play an important role. To identify possible sources of these systematic effects it is instructive to go back to the ideogram with the statistical errors.

While the results from the decay into $\gamma\gamma$ favour higher values of the radiative width, both the decay channels $\rho\gamma$ and $\eta\pi\pi$ show the same structure as the total sum, namely the centering around two different values. This latter effect already rules out an earlier attempt for an explanation based on an argument about the decay matrix element for the reaction $\eta' \rightarrow \rho\gamma$. Some of the early experiments did not take into account the magnetic dipole transition nature for this decay and were therefore excluded in some review articles from an averaging of results. However, the split-up into two regions is preserved when these experiments are omitted from the ideograms.

Another possible explanation for this clustering of values might be found in the simulation of the production cross section. Here big differences can be expected if the simple EPA-formalism is taken instead of exact formulas such as the one given in [7,71]. Several different programs are used to calculate the cross sections and to generate the events. One of the commonly used generators is based on a work by Vermaseren [70], used e.g. by the ASP and Crystal Ball collaborations. This generator was cross checked by the Crystal Ball Collaboration [60] with an independent program based on the cross section formula by Bonneau, Gourdin and Martin [71]. One of the integration variables in our generator is the scattering angle of the leptons. Our MC events have been generated in the range from 0-450 mrad. The dependence of the cross section integration result INT in eq.4.1 on this scattering angle is shown in fig.6.13. Above angles of 150 mrad the value stays stable and reaches the limiting value of 166 nb/keV. The integration has been performed with a ρ -form factor and for a centre of mass energy of 10.01 GeV at the Υ -resonance as studied by the Crystal Ball collaboration. The values used in their study of the η' -decay into $\eta\pi^0\pi^0$ [60] are shown in the same figure and are in excellent agreement with the value obtained with our MC generator. The same exercise has been performed for other beam energies to compare with the integration results of other experiments. The expected dependence of INT on the beam energy as predicted by

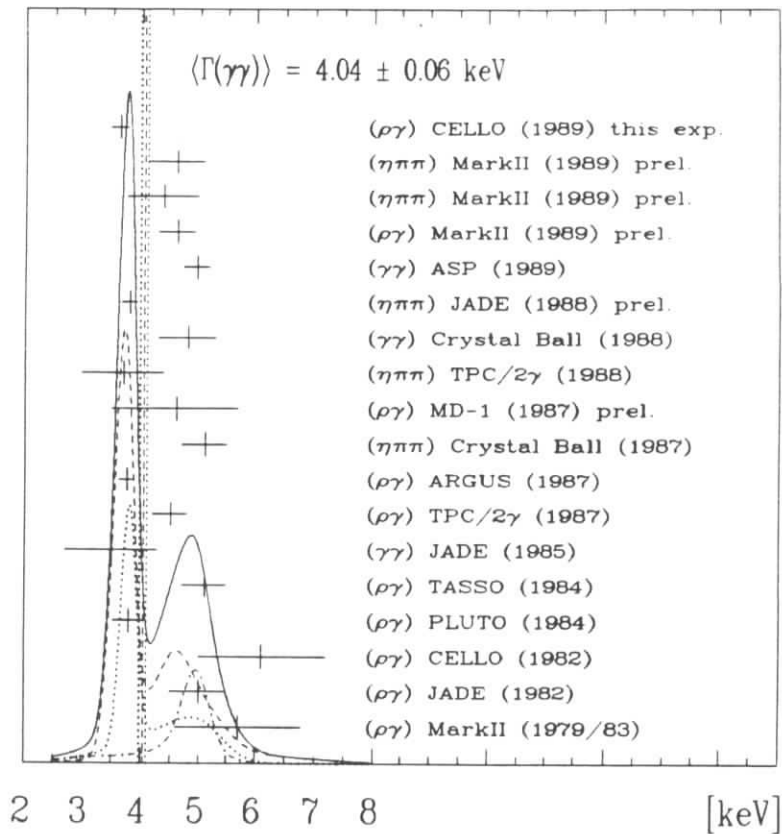


Figure 6.11: Ideogram with statistical errors. The full line is the sum of all Gaussians, while the broken, dotted and dash-dotted line are the results for the $\rho\gamma$, $\eta\pi^+\pi^-$ and $\gamma\gamma$ final states respectively.

our generator is shown as a dashed line in fig.6.14. Besides our value and the Crystal Ball value, the values from TPC/2 γ [68], ASP [64] and MarkII [59] are shown. They agree within 5% with our result for a beam energy of 14.5 GeV, showing that the generator alone cannot account for the wide spread found in the radiative widths. However, the number for MarkII was calculated from a publication which in the meantime was superseded by a later publication [65,66]. In this publications and in the thesis [67] the 1989 values are based upon, the radiative widths are calculated under the false assumption that the Field correction factors $C(\tau)$ (see [72]) can be applied to Low's approximation of the cross section formula. Indeed, Low's formula and Field's leading log approximation are nearly identical up to the argument of the logarithm: $\ln 2E/m$ (Field) vs. $\ln E/m$ (Low). This logarithm of 2 accounts for a difference of 16-14% at energies between 5 and 17.5 GeV. This effect in the meantime has been noticed by MarkII and the results have been corrected accordingly [66] and quoted in the above table as the 1989 results. The exclusion of the MarkII results because of these effects and the preliminary nature of their corrected data does however not change the problem of clustering of results for the radiative width.

If the acceptances of the detectors are correctly understood, the only remaining quantity that can cause such a clustering are the branching ratios of the various channels. Here, the branching ratio of the η' into $\gamma\gamma$ is a clear candidate. Its value has been determined by the Particle Data Group in two different ways. One value is obtained by averaging the individual results of experiments measuring the quantity $\Gamma(\gamma\gamma)/\Gamma_{total}$, the other is obtained by a combined fit to all branching fractions. In the 1986 Particle Data Book the branching ratios obtained from the average (0.0183 ± 0.0016) and the fit (0.0185 ± 0.0016) are in

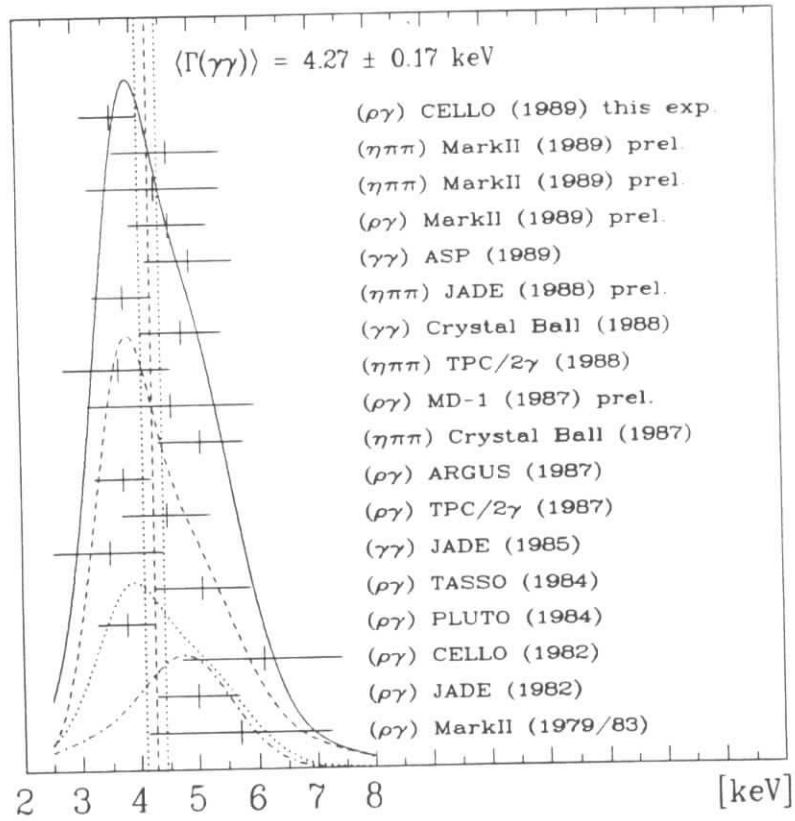


Figure 6.12: Ideogram with statistical and systematic errors added quadratically. The full line is the sum of all Gaussians, while the broken, dotted and dash-dotted line are the results for the $\rho\gamma$, $\eta\pi^+\pi^-$ and $\gamma\gamma$ final states respectively.

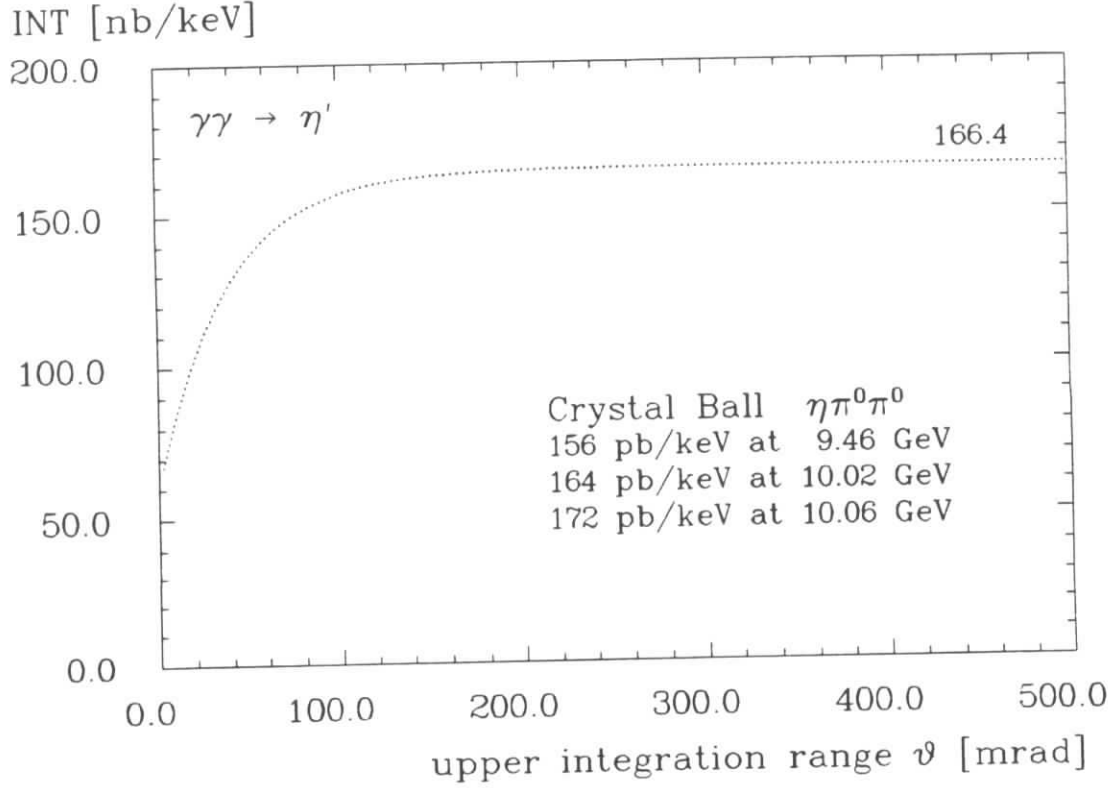


Figure 6.13: Dependence of the numerical integration result INT on ϑ . The dotted line marks the development predicted by the CELLO MC-generator.

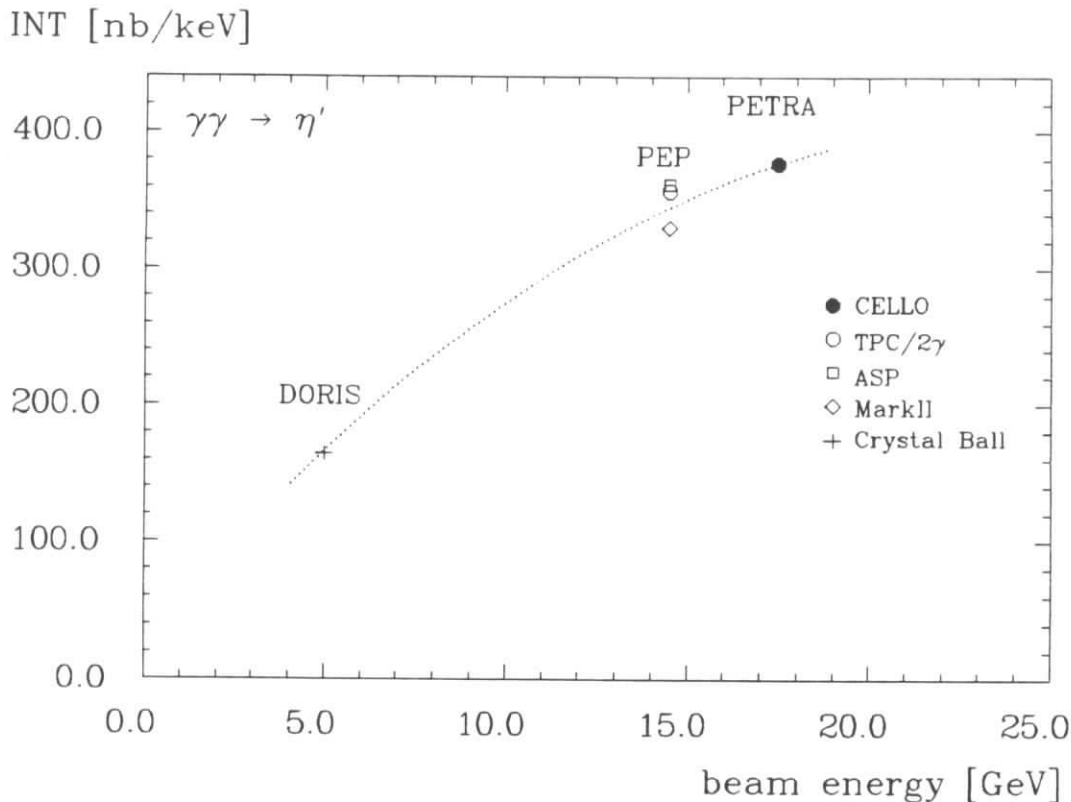


Figure 6.14: Dependence of the numerical integration INT on the beam energy. The dotted line is the result obtained with the CELLO MC-generator.

excellent agreement. The 1988 issue quotes 0.0196 ± 0.0015 for the average and 0.0216 ± 0.0016 for the fit, where the error of the latter is scaled up by a factor of 1.4 to account for inconsistent measurements. The fit result is quoted in the meson summary table and is therefore used as the branching ratio by the experiments. It is 10 % higher than the 1988-average and 18 % higher than the 1986-average. The error on the branching ratio in the same time has only diminished from 8.7% to 7.5%, leaving enough room for further movements of the central value. The changes in the branching ratios are due to measurements of various neutral η' -branching ratios performed by the GAMS Collaboration [75] in 1987, destroying the seemingly consistent picture of fits and averages in the 1986 particle data book. The measurements by GAMS are however very precise and at least one other experiment is now needed to resolve the inconsistencies. With the current measurements of the radiative width in the decay channel $\eta' \rightarrow \gamma\gamma$ a branching ratio as high as 2.6 % is needed to arrive at a value of 4 keV, found for the other two decay modes if averaged with the statistical error only.

If the deviations of the radiative width determined in the $\gamma\gamma$ -decay mode of the η' in comparison to the other two modes can be attributed to the branching ratio, the only recent results that is far off from the average is the measurement of Crystal Ball in the $\eta\pi^0\pi^0 \rightarrow 6\gamma$ decay mode. Here as well the branching ratio has moved by 10% due to the GAMS measurement. With the current branching ratio a value of $5.1 \pm 0.4 \pm 0.6$ keV is found. With about 40 % more data events this value has gone down to $\Gamma_{\gamma\gamma}(\eta') = 4.6 \pm 0.3 \pm 0.5$ keV (prelim.) [76] moving closer to the average of the statistically more significant results. This might be an indication that with more statistics the systematic effects are better understood by the experiments and the apparent discrepancies between the published values can be attributed to a large extent to detector acceptances and branching ratios.

Chapter 7

η' -Form Factor Measurement

To measure the production form factor of a resonance in a two-photon reaction at least one of the scattered leptons has to be detected. Experimentally it is found that the production rate for pseudoscalar mesons is drastically reduced for increasing values of the momentum transferred by the virtual photon. This behaviour is described by different models. The expected dependence of the production rate on the four-momentum squared ($q^2 = -Q^2$) of the virtual photon, tagged by the measurement of its corresponding lepton, typically has the form $1/(1 + Q^2/m^2)^2$. In VDM-type descriptions m is the mass of a ρ or ϕ -meson, in a QCD inspired calculation by Brodsky and Lepage the functional dependence on Q^2 turns out to be the same and the mass is calculated to be $m = 830 \text{ MeV}$.

Whatever model is taken, the production rate is drastically reduced for large values of Q^2 and hence for large tagging angles. Only experiments with tagging devices as close as possible to the beam pipe are able to measure tagged reactions with a reasonable rate. With the CELLO forward detector the Q^2 -range from 0.3 GeV^2 to 3.4 GeV^2 is covered while with the end cap calorimeter Q^2 -values above 3.5 GeV^2 can be measured.

In this chapter, the measurement of the form factor for the pseudoscalar resonance η' is presented in the decay modes $\eta' \rightarrow \rho\gamma$ and $\eta' \rightarrow \eta\pi^+\pi^-$ with $\eta \rightarrow \gamma\gamma$ or $\eta \rightarrow \pi^+\pi^-(\pi^0/\gamma)$. In the last section the results of the various decay channels are combined and will be compared to results of other experiments and theoretical expectations.

7.1 The Reaction $\gamma\gamma^* \rightarrow \eta' \rightarrow \rho\gamma$

A data sample of 5000 events with two charged tracks, one photon and a tag with energy above 2 GeV is available for this analysis. However, in order to have a well reconstructed tag, a tagging energy above 5 GeV is demanded in this analysis. Besides the data sample covering the full acceptance region of the forward calorimeter, a subsample in the well understood region between 50 and 85 mrad is considered as well.

As in the analysis of the corresponding untagged reaction, events with tracks with very small angles with respect to the beam axis are omitted from the analysis. The detection of the photon is done with the barrel calorimeter. Unlike the untagged data sample no signal is visible above the huge background without any kinematical fit. The simple method for recalculating the photon energy from the well measured tracks does not work here, since the tagged lepton carries a non-negligible transverse momentum which is only known with poor precision. Although the φ -resolution was considerably improved, the lack of a good energy resolution in the forward calorimeter still prevents a tuning of the final state system

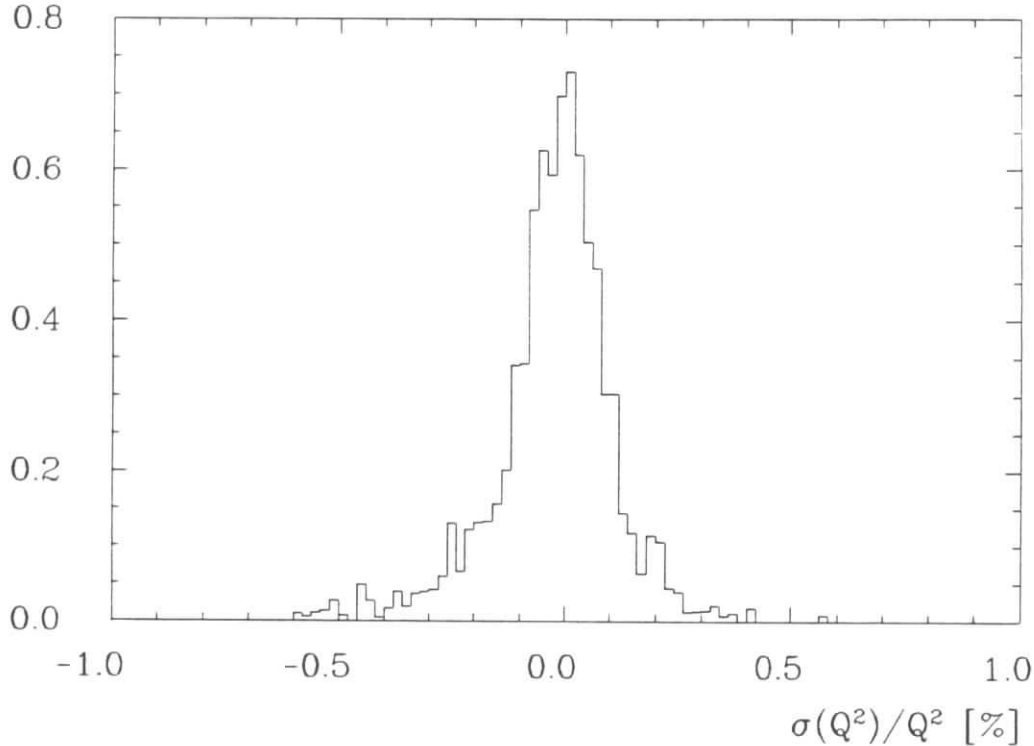


Figure 7.1: Q^2 -resolution of tagged events after a kinematical fit requiring p_t -balance

towards a mass resolution comparable to the one achieved in the untagged reaction. Instead, the kinematical fit improves the Q^2 -resolution. The Q^2 -resolution $\sigma(Q^2)/Q^2$ reached (see fig. 7.1) is 10 % in the forward calorimeter and 8 % in the end cap calorimeter.

The mass spectrum of events surviving the kinematical fit with a χ^2 -probability of $> 2\%$ is shown in fig 7.2. Clearly seen is an η -signal around mass values of 500 MeV and the η' -signal around 950 MeV. The level of background is considerably reduced if only events with photons above an energy of 50 MeV (200 MeV for a cross check, see fig. 7.3 for a comparison between photon energy spectrum in data and MC) are considered and a cut in the decay angle of the π in the ρ -helicity frame of $|\cos\vartheta_\pi^*| < 0.8$ is applied. If events are selected which have their $\pi\pi$ -mass in the ρ -band (500 - 820 MeV) barely any background is left. The corresponding spectrum is shown as the shaded histogram in fig. 7.2 with about 30 η' -candidates.

If besides the photon energy cut and the ρ -band condition events in the η' -region are selected, the distribution of the π -decay angle in the ρ -helicity frame can be studied. Fig. 7.4 shows this distribution in the η' -region with the contribution of two sidebands subtracted to account for the background present under the resonance. The distribution nicely agrees with the expected behaviour for the decay of the η' into the two vector particles ρ and γ . The inset in this figure shows the MC prediction for this angle.

To determine the number of events in the signal region and correctly subtract the number of background events, the mass plot is binned in such a fashion that the expected signal is present in a single bin. This way the neighbouring bins of equal size only contain background events. From these bins the background shape can be inferred and a hand-drawn background is subtracted from the bin containing the signal. This recipe is now applied to the mass spectrum with mass bins of 200 MeV width and a signal bin that is centred at 950 MeV. The data sample is split according to the measured Q^2 -values of the event into 5 bins of Q^2 with

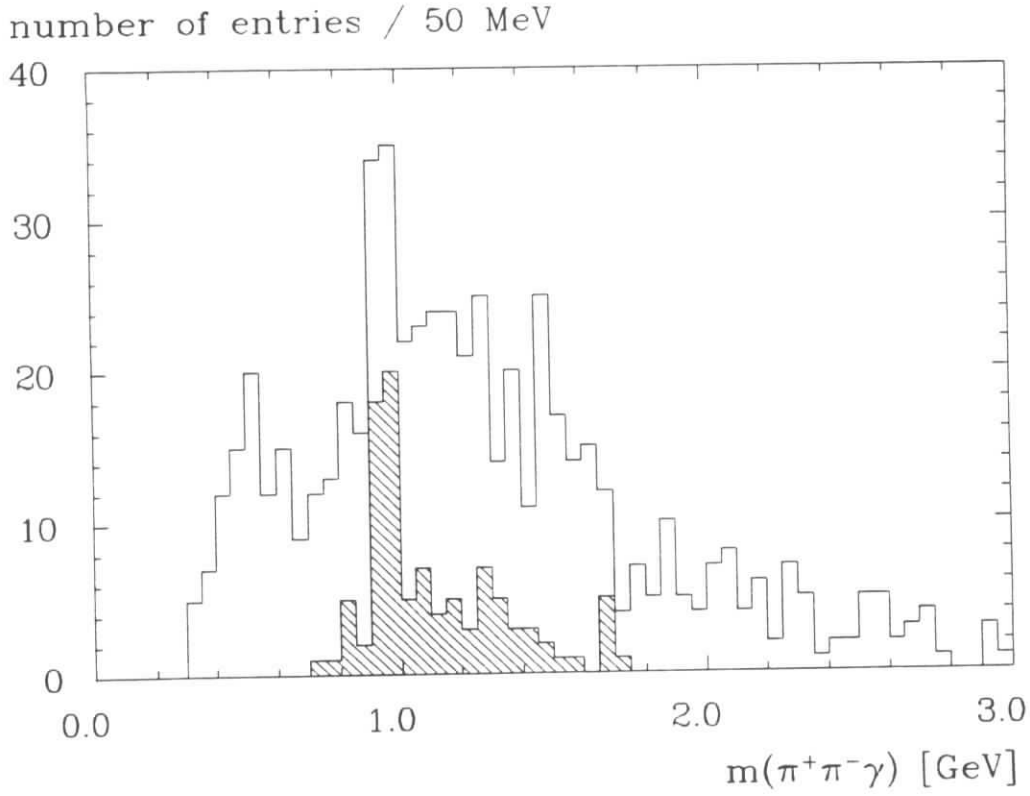


Figure 7.2: Invariant $m(\pi^+\pi^-\gamma)$ -spectrum for tagged events after a full kinematical fit. The shaded histogram shows the spectrum for events in the ρ -band with $|\cos\vartheta_\pi^*| < 0.8$ and $E_\gamma > 200\text{MeV}$.

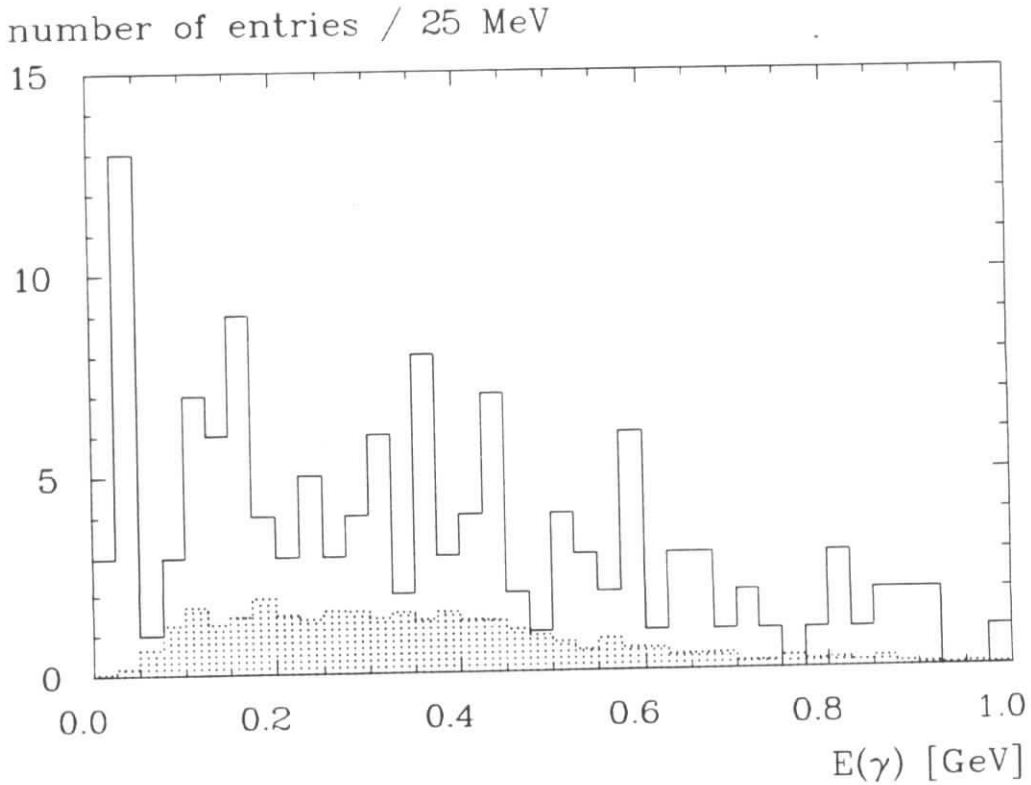


Figure 7.3: Photon energy spectrum for data and MC events in the ρ -band with $|\cos\vartheta_\pi^*| < 0.8$. The MC distribution (shaded histogram) is the prediction for a ρ -pole form factor.

number of events

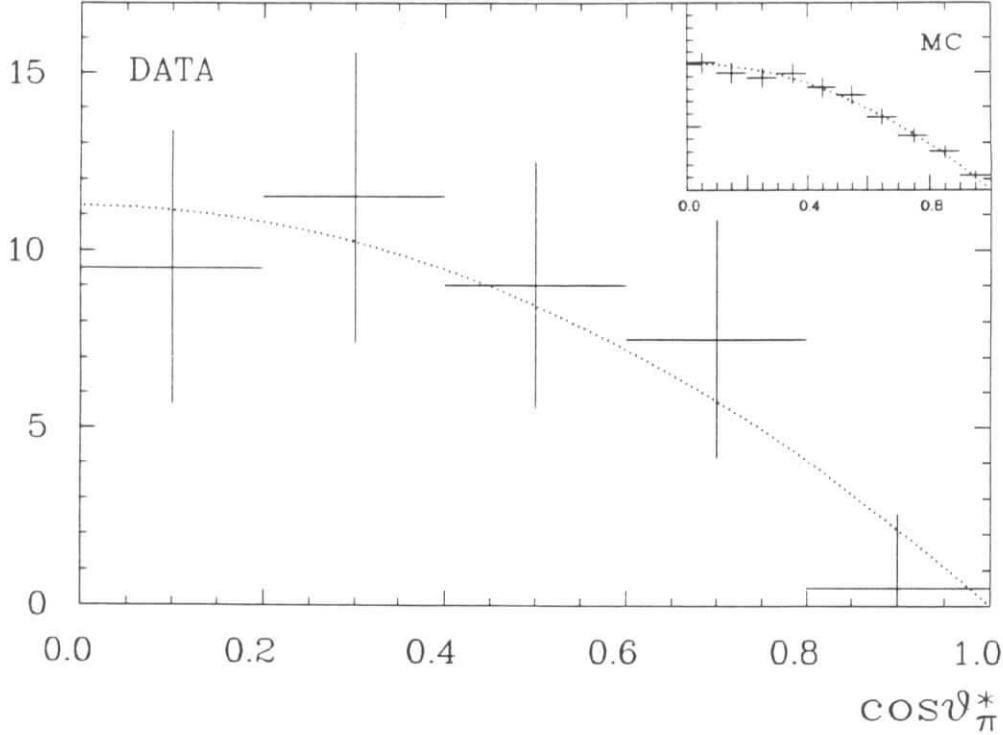


Figure 7.4: Decay angle of the π in the ρ -helicity frame, the inset shows the MC prediction for a $0^- \rightarrow 1^-1^-$ decay for the case where one of the vector particles is a photon

roughly equal statistics. The first 4 Q^2 -bins cover the forward calorimeter, the last Q^2 -bin the end cap calorimeter. The resulting number of η' -events in each Q^2 -bin can be found in table 7.1, the number of events including the background is given behind the slash. The total number of η' -events after background subtraction found this way is 31.0 ± 6.6 (44 including background) for a cut of 200 MeV in the photon energy and 41.0 ± 7.7 (59) for a cut of 50 MeV.

The Q^2 -dependence of the production form factor is given by comparison of these numbers with the MC expectation for a flat form factor. The MC events in this analysis have been generated according to a J/Ψ -form factor (see chapter 4) and consequently have to be weighted according to a flat form factor and the data luminosity to obtain the desired result. Out of 24000 events that were subjected to the detector simulation 5000 events remain after

Q^2 [GeV]	# of data events	# of MC events	$\Gamma_{\gamma\gamma} \cdot f^2(Q^2)$ [keV]
0.3 – 0.8	18/24 (10.5/15)	16.87 (12.91)	1.07 ± 0.29 (0.81 ± 0.30)
0.8 – 1.2	10/16 (10.0/14)	18.39 (15.20)	0.54 ± 0.22 (0.66 ± 0.25)
1.2 – 1.7	7/11 (3.5/6)	17.39 (14.12)	0.40 ± 0.19 (0.25 ± 0.17)
1.7 – 3.4	4.5/5 (4.5/5)	24.83 (21.95)	0.18 ± 0.09 (0.21 ± 0.10)
3.4 – 20.	1.5/3 (1.5/3)	78.19 (72.07)	0.019 ± 0.022 (0.021 ± 0.024)

Table 7.1: Values of the form factor in 5 bins of Q^2 covering the full acceptance region of the forward calorimeter and end cap calorimeter. The values are given for a photon energy above 50 MeV (200 MeV). The number given behind the slash is the number of events in the signal region including background.

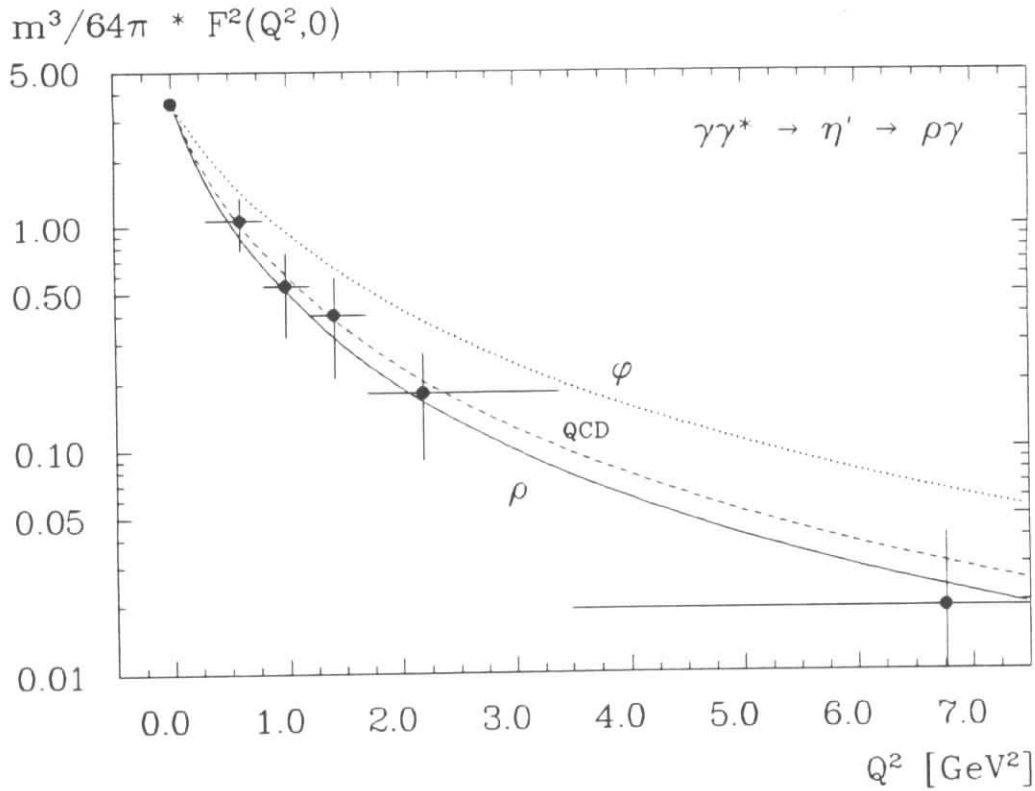


Figure 7.5: Q^2 -evolution of the η' - γ transition form factor in the reaction $\eta' \rightarrow \rho\gamma$ (in keV) for events with a photon energy above 50 MeV. Shown are also the predictions for a ρ and ϕ -VDM form factor and the QCD-prediction by Brodsky and Lepage

all the cuts described. These events are now split into the 5 Q^2 -bins. The weighted number of η' -events in each of the bins is shown in the table with the data events. Dividing the corresponding numbers directly yields the value for the form factor f^2 times the radiative width $\Gamma_{\gamma\gamma}$ of the resonance ($\Gamma_{\gamma\gamma} \cdot f^2(Q^2, 0) = m^3/64\pi \cdot F^2(Q^2, 0)$). The values are plotted in fig. 7.5 together with the data point at $Q^2 = 0$ from the analysis of the untagged reaction described further above. Also shown are the VDM predictions for a ρ and ϕ -form factor and the QCD-form factor as predicted by Brodsky and Lepage, all normalized to the data point at $Q^2 = 0$.

The central region of the forward calorimeter is much better understood than the full acceptance region. If the tags are restricted to the range of 50 to 85 mrad, a nice agreement in the energy spectra between data and MC is obtained for tagged electron and muon-pairs [77] regarding shape and absolute normalization. Although about half of the events are lost by this cut, it is quite instructive to repeat the above analysis for this region. Keeping the

Q^2 [GeV]	# of data events	# of MC events	$\Gamma_{\gamma\gamma} \cdot f^2(Q^2)$ [keV]
0.3 - 0.8	0.0 (1)	1.96	-
0.8 - 1.2	8.5 (12)	13.95	0.61 ± 0.25
1.2 - 1.7	3.5 (6)	13.49	0.26 ± 0.18
1.7 - 3.4	1.5 (2)	6.07	0.25 ± 0.24

Table 7.2: Values for the form factor in the restricted region of the forward calorimeter (50 - 85 mrad) for a photon energy above 200 MeV

same Q^2 -binning as before, the number of data and MC events are determined in the way described above. The number of events and the values for the form factor can be found in table 7.2. Within the statistical precision achieved these values are in good agreement with the ones obtained in the full acceptance region of the forward calorimeter. The following analyses will therefore always exploit the full region available.

The systematical uncertainties in the determination of the Q^2 -development of the form factor comprises all the uncertainties already mentioned in the analysis of the untagged data. However, one has to take into account the larger error for the trigger simulation (6% for the forward tagged events and 10% for events measured in the end caps), some 15 % error from background subtraction and 10% from the photon energy cut, giving rise to a total systematic error of 23 %.

7.2 The Reaction $\gamma\gamma^* \rightarrow \eta' \rightarrow \eta\pi^+\pi^-$, $\eta \rightarrow \gamma\gamma$

While for untagged reactions the decay of the η' into $\rho\gamma$ has been studied by previous experiments far more often than the decay into $\eta\pi^+\pi^-$, this is not true for tagged reactions. Each of these decay modes has been observed by two collaborations in the tagged mode (for a discussions of their results see the conclusions of this chapter). The most pronounced difference to the process described in the last section is the low Q -value of the reaction. Due to the masses involved only a small amount of kinetic energy is available for the decay products. A sizeable transverse momentum of the tracks is however needed in order to pass the trigger condition in the CELLO detector. Therefore, this reaction can only be studied in the tagged mode in our detector. With a magnetic field of 1.32 T tracks from the corresponding untagged reaction curl up in the inner detector. The photons from η -decay on the average have an energy of 274 MeV from the decay and some additional energy due to the momentum of the η itself. Both of the photons can therefore be detected with a reasonable rate and the η can be reconstructed. Once the η is reconstructed, events from this decay channel of the η' are easily identified.

The data sample with two charged tracks, two reconstructed photons and a tagged lepton is much smaller than the one in the previous analysis, it only contains 1500 events. As before, only tags with an energy above 5 GeV are considered for the determination of the Q^2 -dependence of the form factor.

To reconstruct this specific decay mode of the η' , the decay of the η into two photons has to be identified. The mass resolution, taken from MC, for the reconstruction of this resonance decay is 70 MeV. The invariant $\gamma\gamma$ -mass spectrum for data events is shown in fig.7.6, with the expected MC mass distribution shown in the inset in the upper right hand corner of the same figure. Seen is a clear π^0 -signal in the data spectrum, an η -signal, however, is not evident in this plot. It is believed that the small signal is submerged in a larger background of badly measured photon pairs and combinations of photons from higher multiplicity states.

With a mass cut of 310 - 720 MeV events in the η -band can safely be selected, rejecting at the same time all the background from π^0 's. Using the events in the η -band a full kinematical fit with an η -mass constraint for the two photons is performed. The $\gamma\gamma$ -mass spectrum of events surviving this fit is shown as the shaded histogram in fig.7.6.

Combining the two photons fitted to η -mass with the two charged particles yields the invariant $\eta\pi^+\pi^-$ -mass spectrum shown in fig.7.7. A background free η' -signal with 10 events is seen on the left hand side of the mass spectrum. The transition form factor of the η' -meson

number of entries / 20 MeV

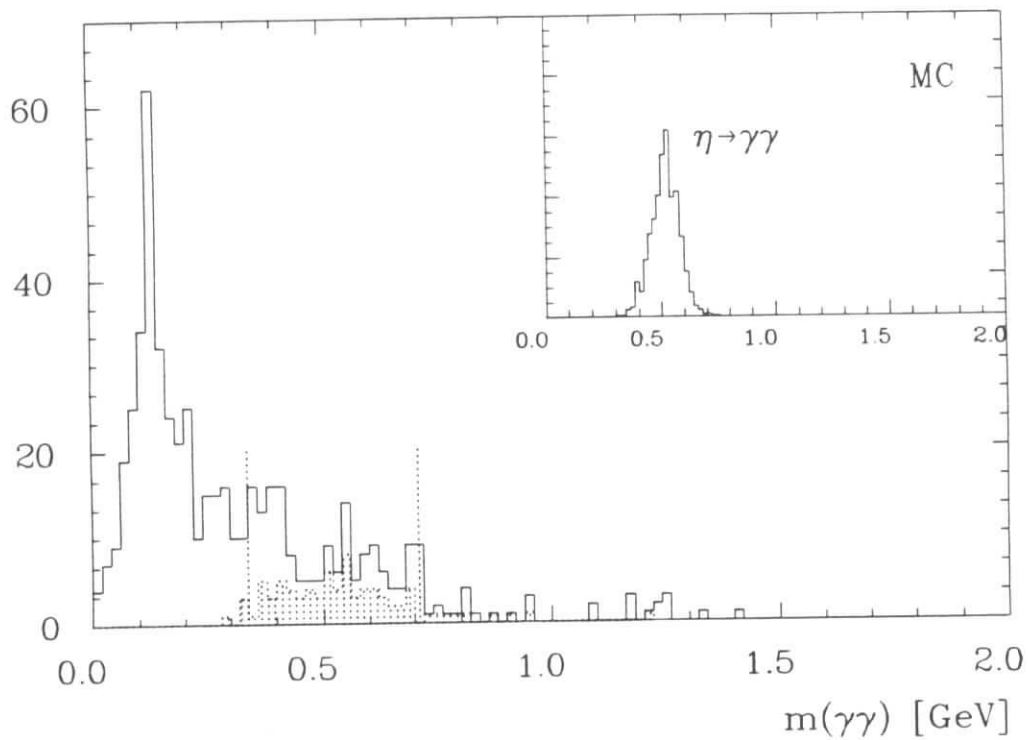


Figure 7.6: Invariant $\gamma\gamma$ -mass for events with two charged tracks and two photons. The solid line histogram shows all events while the events in the shaded histogram survived a kinematical fit with η -mass constraint for the two photons. The dotted lines mark the η -band cut range. The histogram in the upper right hand corner shows the corresponding MC prediction.

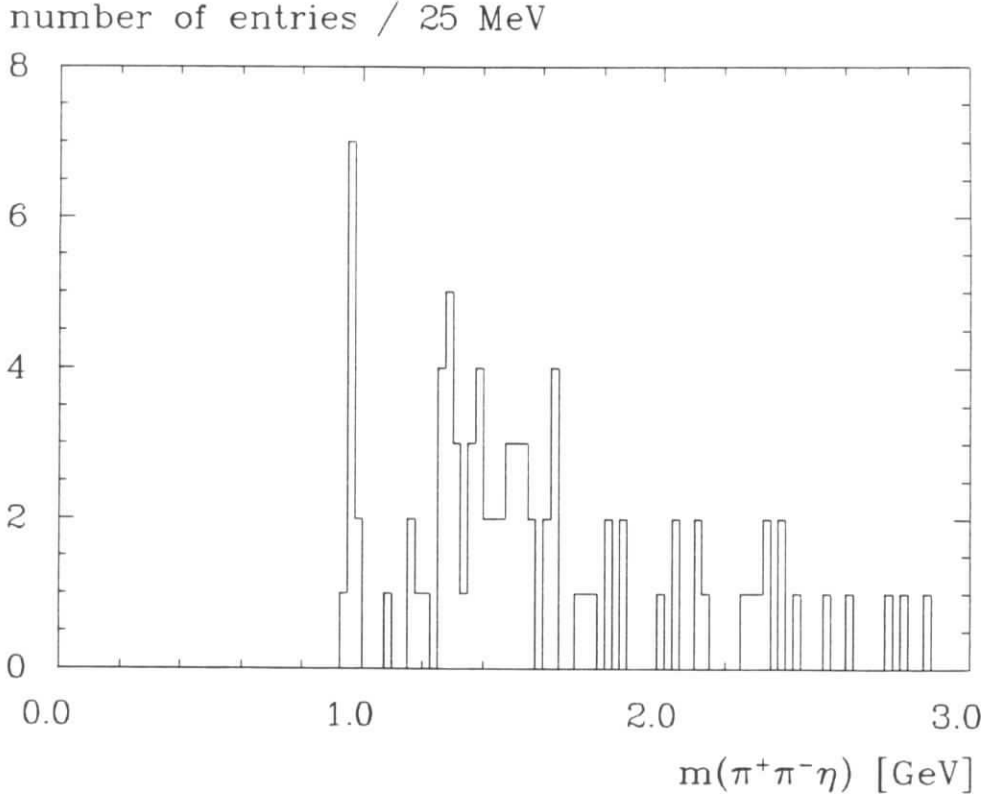


Figure 7.7: Invariant $\pi^+\pi^-\eta$ -mass spectrum after a full kinematical fit with η -mass constraint.

will be determined in the same way as described in the section about its decay mode into $\rho\gamma$. For a later comparison data and weighted MC events are split up into the same 5 Q^2 -bins covering the full acceptance region of the forward calorimeter and the end cap calorimeter. The correlation between the invariant $\eta\pi^+\pi^-$ -mass of the events with their Q^2 -value can be found in fig.7.8. The data events are marked as full circles while the MC events are shown as points. The dotted lines represent the borders of the Q^2 -bins chosen, 4 of them in the forward and one in the end cap calorimeter. The number of data and MC events found in these bins is given in table 7.3. Since no data event is found in the third bin, the values of bin two

Q^2 [GeV]	# of data events	# of MC events	$\Gamma_{\gamma\gamma} \cdot f^2(Q^2)$ [keV]
0.3 – 0.8	3	1.80	1.67 ± 0.96
0.8 – 1.2	4	3.29	combined with next bin
1.2 – 1.7	0	4.72	0.50 ± 0.25
1.7 – 3.4	2	9.80	0.20 ± 0.14
3.4 – 20.	1	27.83	0.036 ± 0.036

Table 7.3: Values of the form factor for the reaction $\eta' \rightarrow \pi^+\pi^-\eta$, $\eta \rightarrow \gamma\gamma$. The values of bins 2 and 3 have been combined, since no data event has been found in the latter bin.

and three have been combined to a single data point for the form factor at $Q^2 = 1.2 \text{ GeV}^2$. Again, the values for the relevant quantity form factor times radiative width of the resonance is calculated from a division of the number of data events and MC events in these bins. The resulting values agree within their statistical error with the ones found in the previous decay mode. They also show the step decrease of the form factor with increasing values of Q^2 . The data points from the form factor measurement in this decay mode are plotted in fig. 7.9.

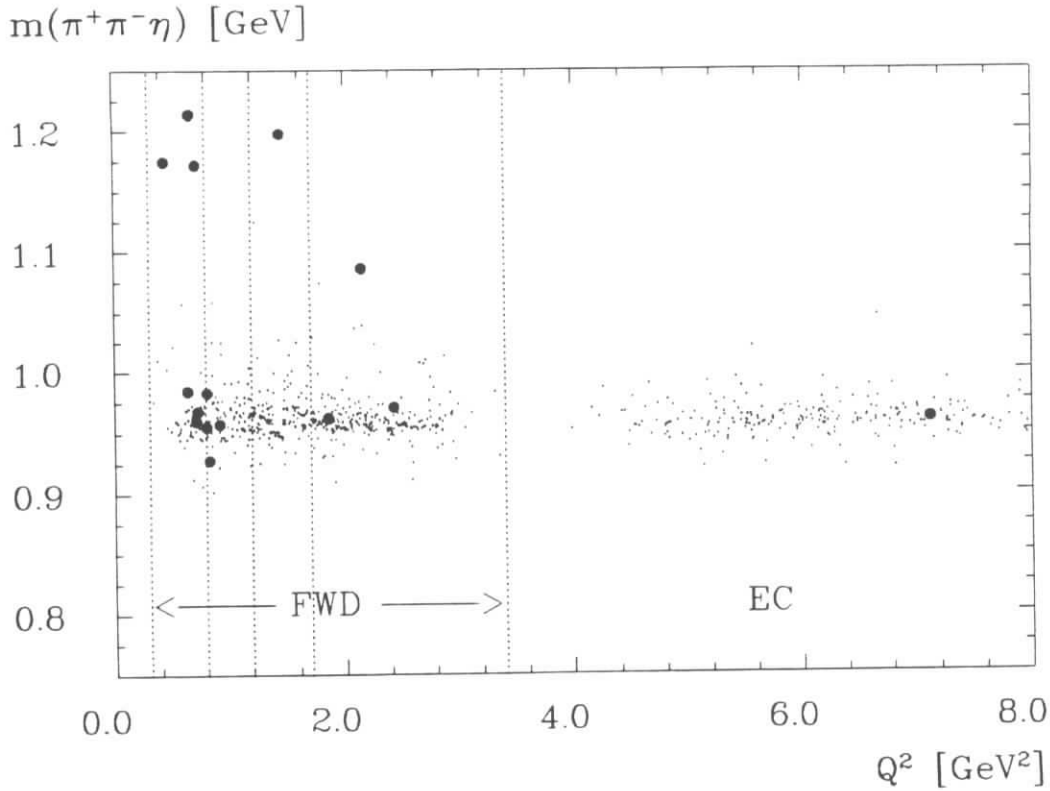


Figure 7.8: Correlation between invariant $\pi^+\pi^-\eta$ -mass and Q^2 . The dotted lines mark the borders of the Q^2 -bins in the forward and end cap calorimeters. The data events are marked with full circles, while the MC events are shown as dots.

The VDM- and QCD-predictions normalized to the measured value of the radiative width from the untagged reaction $\eta' \rightarrow \rho\gamma$ are shown as well in this figure.

The systematical uncertainty for this measurement is of the same order as in the previous analysis. The much smaller error from the background subtraction is compensated by the increased error due to the photon detection efficiency. The total systematical error is estimated to be 25 %.

7.3 The Reaction $\gamma\gamma^* \rightarrow \eta' \rightarrow \eta\pi^+\pi^-$, $\eta \rightarrow \pi^+\pi^-(\pi^0/\gamma)$

In the last section the reaction $\eta' \rightarrow \eta\pi^+\pi^-$ has been analysed for the decay of the η into two photons. This neutral decay of the η has been observed in tagged and untagged reactions several times. The final state with the charged decay of the η into $\pi^+\pi^-\pi^0$ (branching ratio 23.7 %) and $\pi^+\pi^-\gamma$ (BR 4.9 %) has so far only been observed in an untagged reaction by one experiment [65]. The analysis presented here constitutes the first measurement of this decay channel in a tagged two-photon reaction.

The identification of this decay mode demands the reconstruction of all 4 charged tracks in the inner detector, where one of the tracks needs a transverse momentum larger than 250 MeV, so that the event can pass the trigger. A modification of our track reconstruction program allows the identification and reconstruction of tracks in clean events down to transverse momenta of 60 MeV. With this modification the number of events with 4 charged tracks has been increased by 50 %. The photon and the π^0 carry so little momentum that with a high probability they are not detected in the lead liquid argon calorimeters. Therefore, the

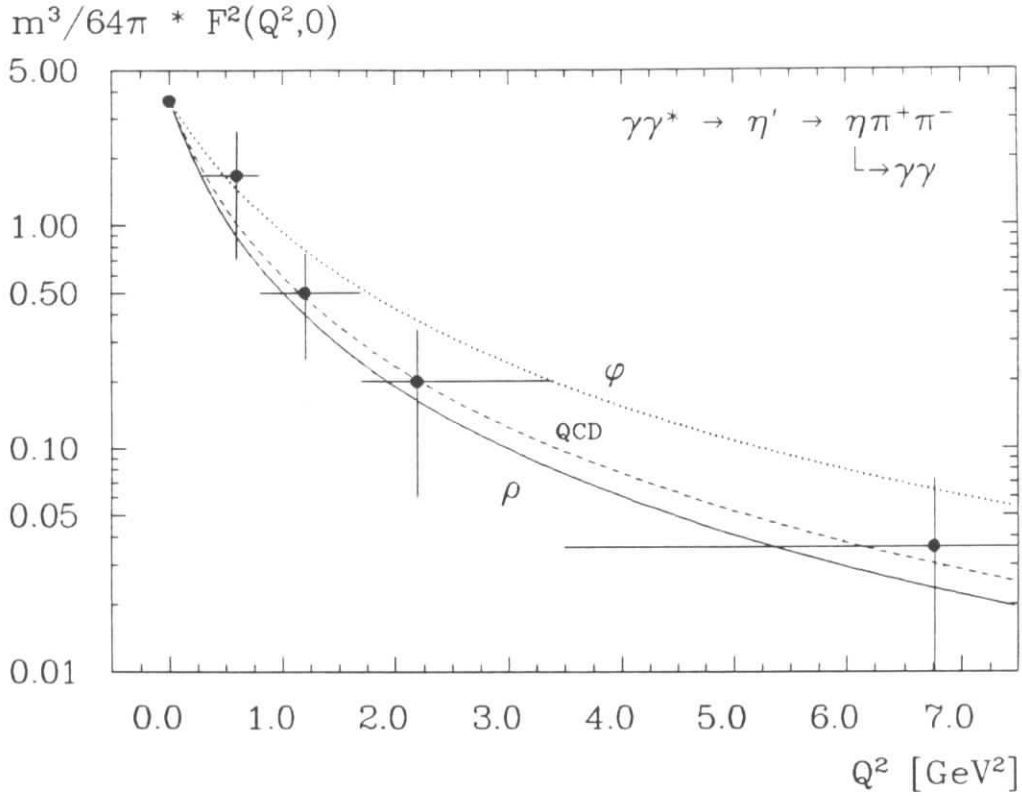


Figure 7.9: Q^2 -evolution of the η' - γ transition form factor in the reaction $\eta' \rightarrow \eta\pi^+\pi^-$ with $\eta \rightarrow \gamma\gamma$. Shown are also the predictions for a ρ and ϕ -VDM form factor and the QCD-prediction by Brodsky and Lepage

η' -decay will not be reconstructed completely. Instead, the identification of this decay is done by summing up the charged pion four-momenta to an invariant 4π -mass.

A data sample of 3600 events with 4 charged tracks, any number of photons (including zero) and a tag with a measured energy above 2 GeV is available for this analysis. In order to have well measured tracks a cut of $|\cos\vartheta| < 0.88$ has been applied on the track direction. By loosening this cut to a value of $|\cos\vartheta| < 0.95$ one can gain an additional 50 % of statistics. The influence of this cut on the form factor measurement will be taken into account in the final systematic error.

Since the final state under study is incomplete, a kinematical fit can only be performed if the missing particles carry only little transverse momentum. Therefore, it is demanded that the tag is located opposite in azimuth to the 4π -state. A cut of $\varphi_{tag,4\pi} > 2.8$ has been found by MC to be adequate for this purpose. The distribution of this angle in data events can be seen in fig.7.10, the cut value is marked with a dotted line. To check the effect of the kinematical fit, the data sample is analysed with and without the fit, both times with the same cut in the angle φ introduced above.

Since the track parameters of the pions are well measured within the CELLO detector, the kinematical fit does not change these parameters too much and the invariant mass spectrum, therefore, stays more or less the same. Instead, the parameters of the tagged lepton, especially its energy, are greatly improved.

The invariant 4π -mass of events passing this fit and the cuts mentioned above is shown in fig.7.11. The signal at 780 MeV on the left hand side of the spectrum is identified as an η' -signal. Shown in the same plot is the MC prediction for the invariant 4π -mass, normalized

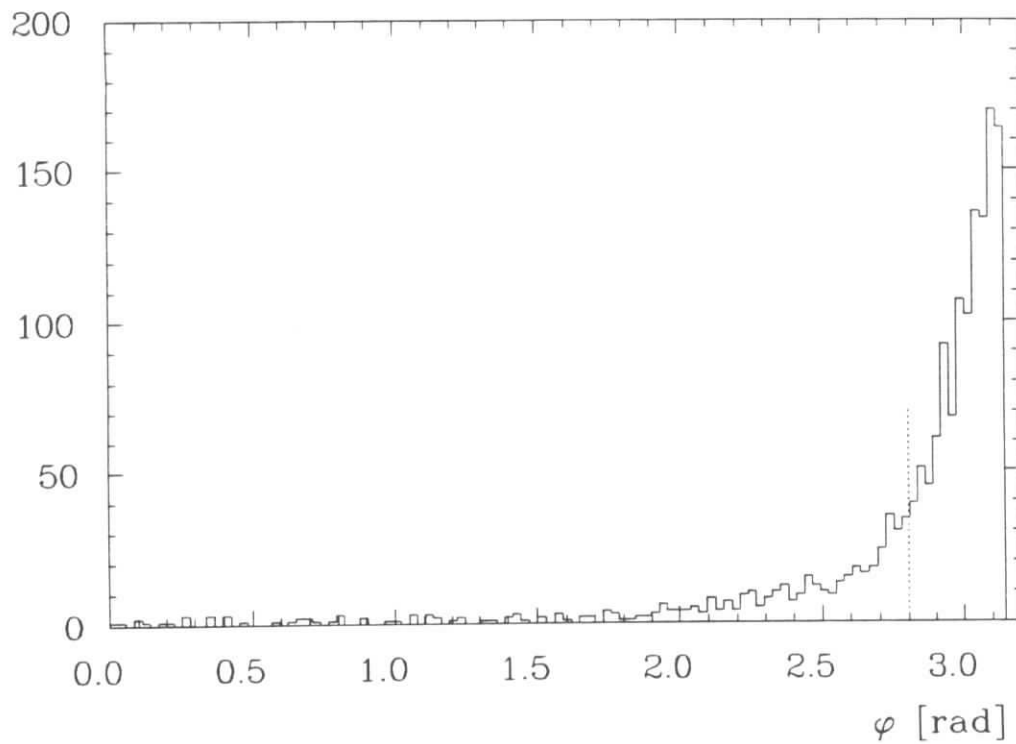


Figure 7.10: Angle between tag and 4π -system in the $r\varphi$ -plane. The dotted line marks the cut value.

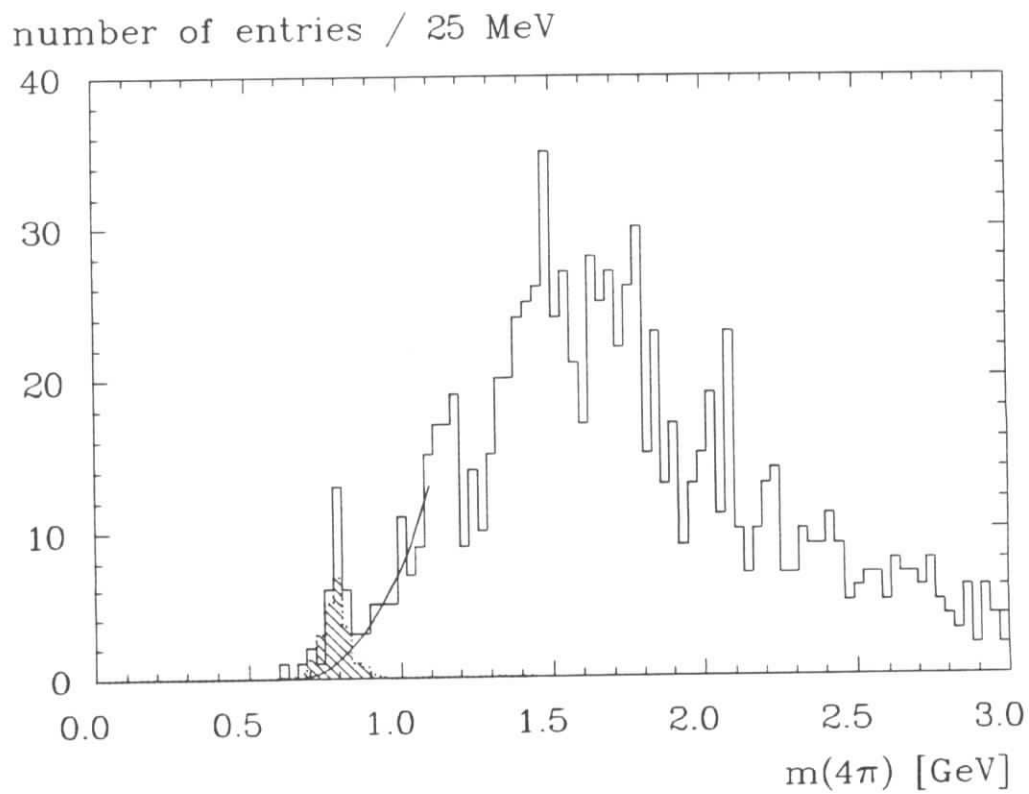


Figure 7.11: Invariant 4π -mass

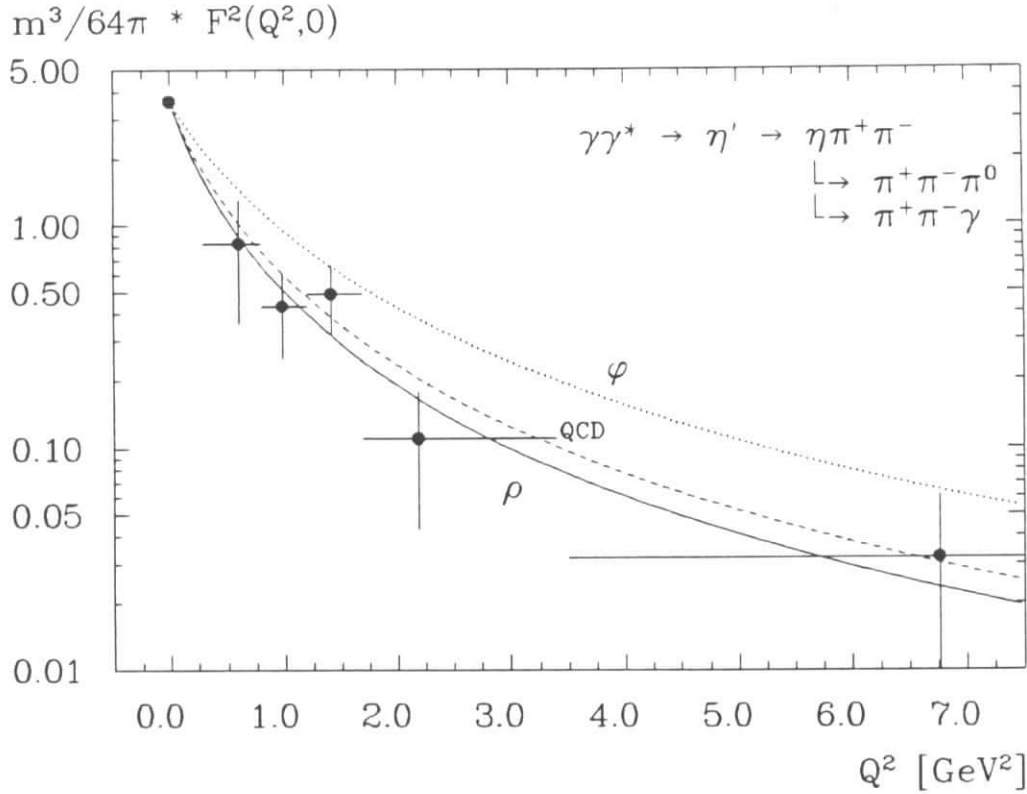


Figure 7.12: Q^2 -evolution of the η' - γ transition form factor in the reaction $\eta' \rightarrow \eta\pi^+\pi^-$ with $\eta \rightarrow \pi^+\pi^-(\pi^0/\gamma)$ for the values shown in table 7.4. Shown are also the predictions for a ρ and ϕ -VDM form factor and the QCD-prediction by Brodsky and Lepage

to the measured radiative width and a ρ -form factor for the Q^2 -dependence. Position, width and absolute normalization between the 4π -mass spectra of data and MC agree quite well.

From the MC shape of the 4π -mass spectrum a signal region of 0.69 – 0.87 GeV is defined. To determine the number of background events in this region a hand drawn curve for the background shape is inferred from the mass spectrum on the right hand side of the signal. This background shape is shown as a full line in the invariant mass spectrum. The total number of events in the signal region is 31 with an estimated background of 6, thus yielding 25.0 ± 5.6 η' -candidates.

These 6 background events now have to be attributed to the various Q^2 -bins. As before, data and MC events are split into 5 Q^2 -regions and the number of signal and background events is determined from the individual mass spectra in each of these regions, giving rise to the numbers found in table 7.4. Hereby, the numbers before the slash denote the number of signal events after background subtraction, while the total number of events including background is given behind the slash. The MC events are treated in the same way. The resulting values for the form factor in this table are plotted with the predictions of the different models in fig.7.12. The values shown are for the angular track cut of $|\cos\vartheta| < 0.95$ and kinematically fitted events.

The systematical effects of the fit and the angular cut is found to be much smaller than the statistical uncertainty at each individual data point. Varying the angular cut between $|\cos\vartheta| < 0.88$ and $|\cos\vartheta| < 0.95$ for fitted and unfitted events the maximum deviation for each data point found is between 10 % and 30 %, uncorrelated in sign between neighbouring data points. This is giving rise to a systematic error of the order of 20% on the average. With

an estimated error of 20 % for the background subtraction, the total error for each data point stays in the order of 30 %. The other contributions from trigger simulation (10%), luminosity error (3%), and track reconstruction efficiency (4%) play a negligible role.

7.4 Conclusions and Discussion

The Q^2 -dependence of the $\eta' - \gamma\gamma^*$ -transition form factor has been measured in three different decay modes of the η' -resonance. The individual results all agree with each other within their statistical errors. The pronounced feature observed for this Q^2 -dependence is the steep fall off of the form factor with increasing values of Q^2 . This general behaviour is well reproduced by VDM-like or QCD-inspired models, which predict an evolution of the coupling between the photons and a resonance with $1/(1 + Q^2/k)$ (see eqn. 2.51, 2.52). Each of these measurements is however not able to distinguish between different models.

The measurements have been performed in such a way that they can easily be combined to a more significant result. By adding up the contributions of each individual Q^2 -bin not only the statistics is increased but also the systematical error is reduced. This is due to the uncorrelated sign of the effects of background subtraction and the specific cuts applied for each of the different final states. These two effects are the largest contributions to the total systematic error and, hence, their reduction greatly improves the situation. The photon acceptance plays a role for those final states where the photons are detected, i.e. it is especially important for the final state with the two photon decay of the η and less important for the $\rho\gamma$ -final state. All other sources for systematic errors are common to all reactions studied. The resulting systematical error for the combined result should thus be of the order of only 15 %.

The resulting numbers for the form factor from the combination of all three measurements can be found in table 7.5. The total number of η' -candidates that are used to derive the $\eta' - \gamma\gamma^*$ -transition form factor is 76 ± 10 over a background of 24 events. The statistical precision is thus of the same order as the systematical effects discussed above. However, due to the observed Q^2 -dependence of the form factor the statistical error is larger for higher values of Q^2 and reach 60% in the end cap calorimeter region. The data points with their error bars are shown in fig.7.13, the vertical bars denote the statistical error and the horizontal ones the Q^2 -range covered.

The description of this Q^2 -development of the form factor is well described by either the QCD-inspired calculation or a VDM-description with a ρ -pole form factor. A ϕ -form factor can be ruled out with the statistical and systematical precision achieved.

Q^2 [GeV]	# of data events	# of MC events	$\Gamma_{\gamma\gamma} \cdot f^2(Q^2)$ [keV]
0.3 – 0.8	5/8	6.0	0.83 ± 0.47
0.8 – 1.2	6/6	14.0	0.43 ± 0.18
1.2 – 1.7	8/8	16.4	0.49 ± 0.17
1.7 – 3.4	4/6	37.1	0.11 ± 0.07
3.4 – 20.	2/3	61.9	0.032 ± 0.029

Table 7.4: Values of the form factor for the reaction $\eta' \rightarrow \pi^+\pi^-\pi^+\pi^-(\pi^0/\gamma)$. These values have been obtained from kinematically fitted events, with tracks within $|\cos\vartheta| < 0.95$ and a cut between the tag and 4π -system of $\varphi > 2.8$.

Q^2 [GeV]	# of data events	# of MC events	$\Gamma_{\gamma\gamma} \cdot f^2(Q^2)$ [keV]
0.3 – 0.8	26.0/35	24.7	1.05 ± 0.24
0.8 – 1.2	20.0/26	35.7	0.56 ± 0.14
1.2 – 1.7	15.0/19	38.5	0.39 ± 0.11
1.7 – 3.4	10.5/13	71.7	0.15 ± 0.05
3.4 – 20.	4.5/7	167.9	0.027 ± 0.016

Table 7.5: Combined values for the η' - γ -transition form factor. These numbers comprises the results from the η' -decays into $\rho\gamma$ and $\eta\pi^+\pi^-$, with a subsequent decay of the η into $\gamma\gamma$, $\pi^+\pi^-\gamma$ and $\pi^+\pi^-\pi^0$.

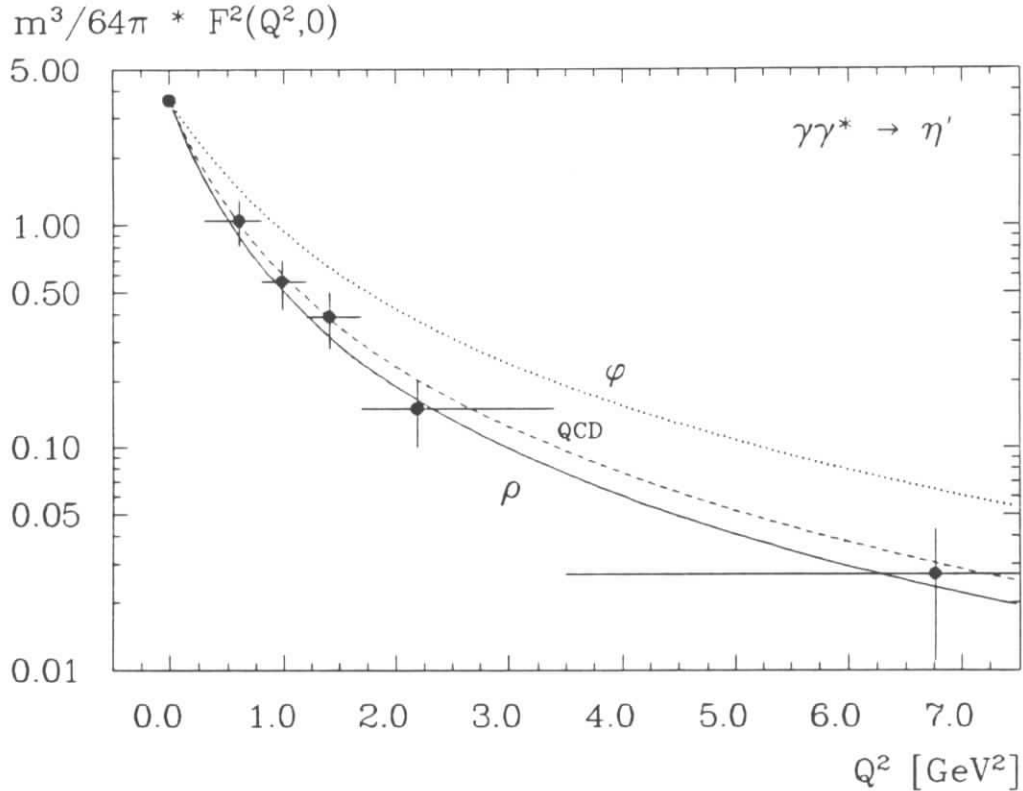


Figure 7.13: Q^2 -evolution of the η' - γ transition form factor, all measured reactions combined. The vertical error bars denote the statistical errors only. The systematic error is of the order of 15%.

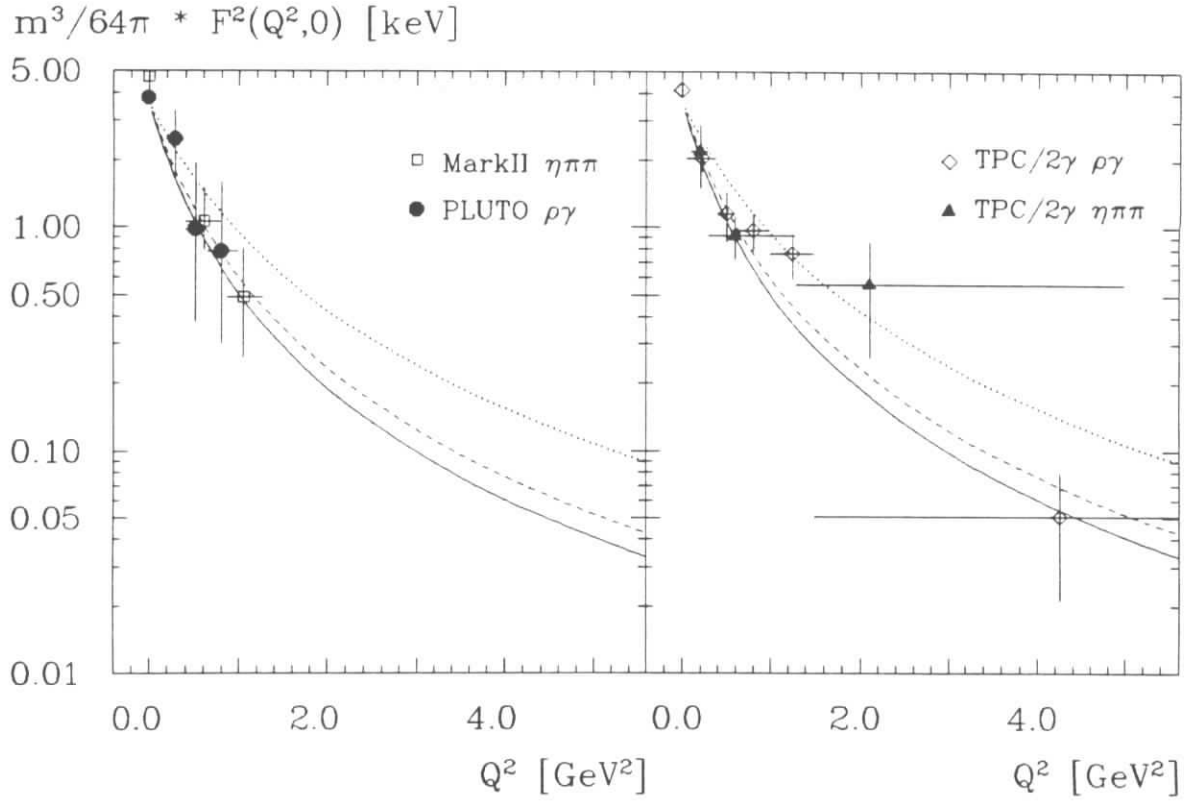


Figure 7.14: A comparison of the η' - γ -transition form factors of the TPC/2 γ , PLUTO and MarkII Collaborations in different decay modes.

A similar result has been found by other experiments that have studied the form factor development. The first measurement of the η' -form factor in the $\rho\gamma$ final state was conducted by the PLUTO Collaboration in 1984 [53]. With the limited statistics of 25 pb^{-1} available, 3 Q^2 -bins were given. The latest measurement of this channel by the TPC/2 γ Collaboration [78] comprises 113 pb^{-1} split up into 5 Q^2 -bins in the range of $0.1 - 5\text{ GeV}^2$. The MarkII [59] and TPC/2 γ [61] collaborations have measured the form factor also in the $\eta\pi^+\pi^-$ -decay. More detailed information on the position of the tagging devices, the Q^2 -range covered and the number of events found by these collaboration has been collected in table 7.6. A graphical

experiment	ref.	\mathcal{L}	ϑ -range of taggers	Q^2 -range	bins	channel	# events
PLUTO	1984 [53]	25	30 - 56	0.1 - 1.0	3	$\rho\gamma$	35 ± 9
TPC/2 γ ^a	1987 [56]	50	25 - 90 100 - 180	0.1 - 5.0	5	$\rho\gamma$	not given
MarkII	1987 [59]	220	21 - 83	0.2 - 1.1	2	$\eta\pi^+\pi^-$	≈ 14
TPC/2 γ	1988 [61]	113	25 - 90 100 - 180	0.1 - 5.0	3	$\eta\pi^+\pi^-$	34 ± 6
TPC/2 γ	1990 [78]	113	25 - 90 100 - 180	0.1 - 7.0	5	$\rho\gamma$	159 ± 15
CELLO	this exp.	86	40 - 110 150 - 400	0.1 - 7.0	5	$\rho\gamma, \eta\pi\pi$	76 ± 10

^a superseded by 1990 publication

Table 7.6: Overview over tagging parameters of various experiments. The observed number of events has been taken from the publication. The value for the MarkII Collaboration has been estimated from the mass spectrum. (The luminosity \mathcal{L} is given in pb^{-1} , the ϑ -range in $mrad$, and the Q^2 -range in GeV^2 .)

presentation of their results is given in fig.7.14. The corresponding values for the form factor

have been taken from the published plots or, when available, have been given by one of the authors [79].

Using the formula 2.52 the pseudoscalar decay constant of the η' can be calculated from the Q^2 -development of the form factor. A fit to the data points from the combined analysis gives a value of 126 ± 7 MeV. This can be compared to the value found by the TPC/ 2γ Collaboration. They give a value of 96 ± 8 MeV [78], which has to be multiplied by $\sqrt{2}$ in our notation. Their adjusted value of 136 ± 11 MeV agrees quite well with our measurement and both are comparable with the value of 131.69 MeV for the π -decay constant found from other reactions [17]. Instead of expressing the results in terms of the decay constant $f_{\eta'}$, the pole mass $\Lambda_{\eta'}$ of the form factor can be given. The corresponding results of such a fit are $\Lambda_{\eta'} = 0.85 \pm 0.07$ GeV for the TPC-Collaboration and 0.794 ± 0.044 GeV for CELLO. The only existing measurement of the form factor in the time-like region by the Lepton-G Collaboration [80] in the reaction $\eta' \rightarrow \mu^+ \mu^- \gamma$ gives a value of $\Lambda_{\eta'} = 0.77 \pm 0.18$ GeV (calculated from the slope of the form factor at $Q^2 = 0$: $b = 1.7 \pm 0.4$ $G\epsilon V^{-2}$; for an overview about other measurements in the time-like region see [19]). All results are in good agreement and give a combined result of $\Lambda_{\eta'} = 0.81 \pm 0.04$ GeV. This number is compatible with a simple ρ -pole and with the prediction of 0.83 GeV by the QCD-inspired model by Brodsky and Lepage [21].

If the value of the untagged reaction at $Q^2 = 0$ is omitted from the fit to our data, the radiative width of the resonance can be determined from the Q^2 -evolution. Assuming a ρ -form factor a fit to the data points yields a value of 3.98 ± 0.52 keV, using the above value of the decay constant we get 3.68 ± 0.48 keV, and with the π -decay constant a value of 3.31 ± 0.43 keV is reached. All values agree within their large error with the result obtained directly from the untagged analysis.

Chapter 8

η -Form Factor Measurement

The η -resonance is the lightest pseudoscalar meson that can be observed in a charged decay mode in two-photon reactions. Belonging to the same quark multiplet as the η' -meson a similar behaviour is expected for the coupling to two photons and its development with increasing values of Q^2 . This chapter will present the measurement of the η - $\gamma\gamma^*$ -transition form factor in the decay modes $\pi^+\pi^-\gamma$ and $\pi^+\pi^-\pi^0$, with the π^0 decaying into two photons. Since for most of the π^0 decays only one photons will be observed, a clear distinction of the two decay modes of the η is not possible. Only for the case of the full reconstruction of the π^0 the decay channel can be identified.

The analysis will proceed as follows. In the first section to come the final state with two charged tracks and two photons will be analysed, followed by the data sample with just one photon detected. Finally, the two measurements will be combined and compared to the only other existing measurement of this form factor.

8.1 The Reaction $\gamma\gamma^* \rightarrow \eta \rightarrow \pi^+\pi^-\pi^0$

The data sample analysed is the same as the one used for the form factor measurement of the η' in the decay mode $\eta\pi^+\pi^-$. From the 1500 events again only those are considered which have a measured tag energy above 5 GeV. This time, however, events in the π^0 -band are selected. To accept most of the π^0 -candidates and reject as many background events as possible a range from 70 – 190 MeV has been selected as the π^0 -band (for a mass spectrum of the π^0 -candidates see fig. 7.6 on page 70). The events are now subjected to a full kinematical fit with π^0 -mass constraint for the two photons. Events that survive this fit with a χ^2 -probability of larger than 1 % constitute the final sample. The invariant mass spectrum of these events in the range from 300 MeV to 1.3 GeV is shown in fig. 8.1. On the left hand side of the spectrum a peak due to the η -decay into $\pi^+\pi^-\pi^0$ is observed separated from the rest of the spectrum. In the same plot the MC expectation for this decay is shown under the assumption of a ρ -form factor for a radiative width of 0.51 keV.¹ The same MC study has shown that the contribution from the $\pi^+\pi^-\gamma$ -channel with an extra fake photon is less than 2%. The peak, therefore, can be attributed solely to the reaction $\eta \rightarrow \pi^+\pi^-\pi^0$.

The data events are now split into 5 bins according to the squared four-momentum transferred by the virtual photon. The Q^2 -bins are the same as in the analysis of the η' -form factor. The MC events which have been generated with a J/Ψ -form factor are weighted such that

¹The value for the radiative width has been obtained by averaging the measurements from two-photon experiments [81].

number of events / 20 MeV

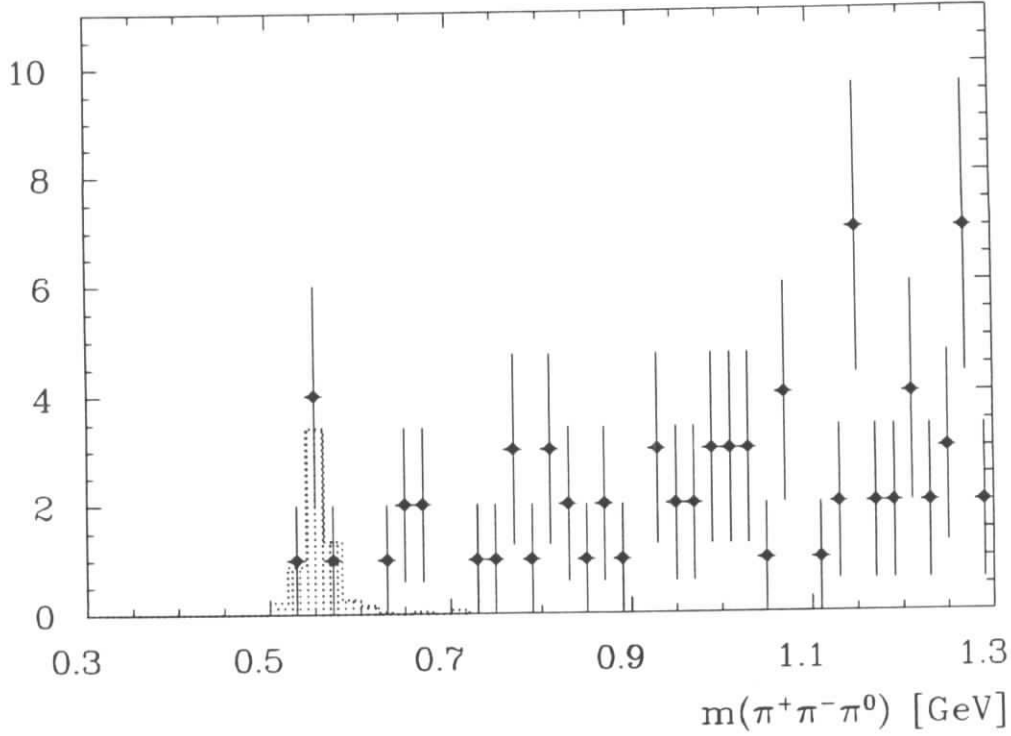


Figure 8.1: Invariant $\pi^+\pi^-\pi^0$ -mass spectrum after a kinematical fit with π^0 -mass constraint. The shaded histogram is the MC expectation for this process assuming a ρ -form factor.

they are consistent with a flat form factor. The number of events found in each of the Q^2 -bins is given in table 8.1. From these numbers the values of the form factor can be calculated.

Q^2 [GeV]	# of data events	# of MC events	$\Gamma_{\gamma\gamma} \cdot f^2(Q^2)$ [keV]
0.3 – 0.8	2	11.2	$0.179+0.179-0.089$
0.8 – 1.2	2	27.6	$0.072+0.072-0.036$
1.2 – 1.7	1	34.6	$0.029+0.046-0.017$
1.7 – 3.4	1	59.2	$0.017+0.027-0.010$
3.4 – 20.	0	27.4	—

Table 8.1: Values of the form factor for the reaction $\eta \rightarrow \pi^+\pi^-\pi^0$.

The corresponding data points are plotted in fig. 8.2. The measured behaviour of the Q^2 -evolution is again well described by the VDM models or the QCD inspired calculation. The fact that no data event is found in the end cap calorimeter region is fully compatible with a MC expectation of 0.2 events assuming a ρ -pole form factor. The total systematic error of this measurement is estimated to be of the same order as in the decay $\eta' \rightarrow \eta\pi^+\pi^-$ discussed in the previous chapter, i.e. roughly 25 %. The errors given for the form factor are the 1σ limits for a Poisson distributed observable. In the same figure with the data points the expected form factor dependence in the VDM picture and the QCD calculation are shown, normalized to the radiative width of 0.51 keV as calculated from recent two-photon experiments.

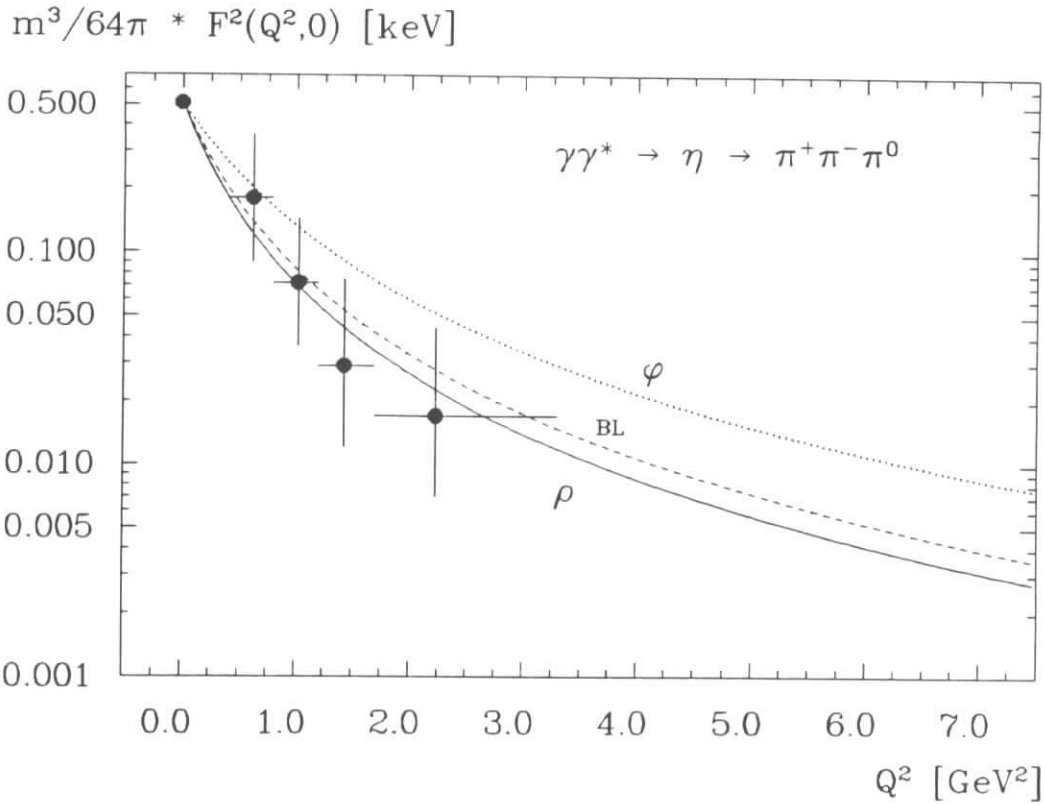


Figure 8.2: Q^2 -evolution of the η -form factor in the fully reconstructed decay mode $\eta \rightarrow \pi^+ \pi^- \pi^0$

8.2 The $\pi^+ \pi^- \gamma$ final state

The majority of all η -decays in the detector show up as an apparent $\pi^+ \pi^- \gamma$ final state. Due to the low Q -value of the reaction $\eta \rightarrow \pi^+ \pi^- \pi^0$, most of the time only one of the photons is recorded in the detector. From a MC study the ratio of fully to incompletely reconstructed events is determined to be of the order of 1:4. This ratio is of course effected if additional cuts on the photon energy have to be applied. The number of η -candidates expected from these arguments and the measurement of the fully reconstructed final state is of the order of 24 events. An additional source of η -candidates is expected from the decay $\eta \rightarrow \pi^+ \pi^- \gamma$. This decay occurs with a relative rate of 20% to the one already mentioned, as can be calculated from the branching ratios of 4.91% ($\eta \rightarrow \pi^+ \pi^- \gamma$) and 23.7% ($\eta \rightarrow \pi^+ \pi^- \pi^0$). However, events from this decay mode show up at the correct nominal mass of the η , while events from the partly reconstructed decay into pions have a smaller mass. Depending on the mass range selected for the signal region the relative contribution of both decays can be varied.

Starting from the tagged data sample with two charged tracks and one reconstructed photon, again only those events have been taken, where the tag energy was measured to be above 5 GeV. These events have been subjected to a kinematical fit requiring a balance of the total transverse momentum of the event. The resulting invariant $\pi^+ \pi^- \gamma$ -mass spectrum is the same as in the analysis of the η' -decay into $\rho \gamma$. Here as well a cut in the photon energy is necessary to remove events with fake photons that are given a very low energy by the fit. For small invariant $\pi^+ \pi^-$ -masses these events otherwise will contribute to the background in the signal region. The invariant $\pi^+ \pi^- \gamma$ -mass spectrum of the events after a photon energy cut of 100 MeV is shown in fig. 8.3. The η -signal is seen over a sizeable background on the

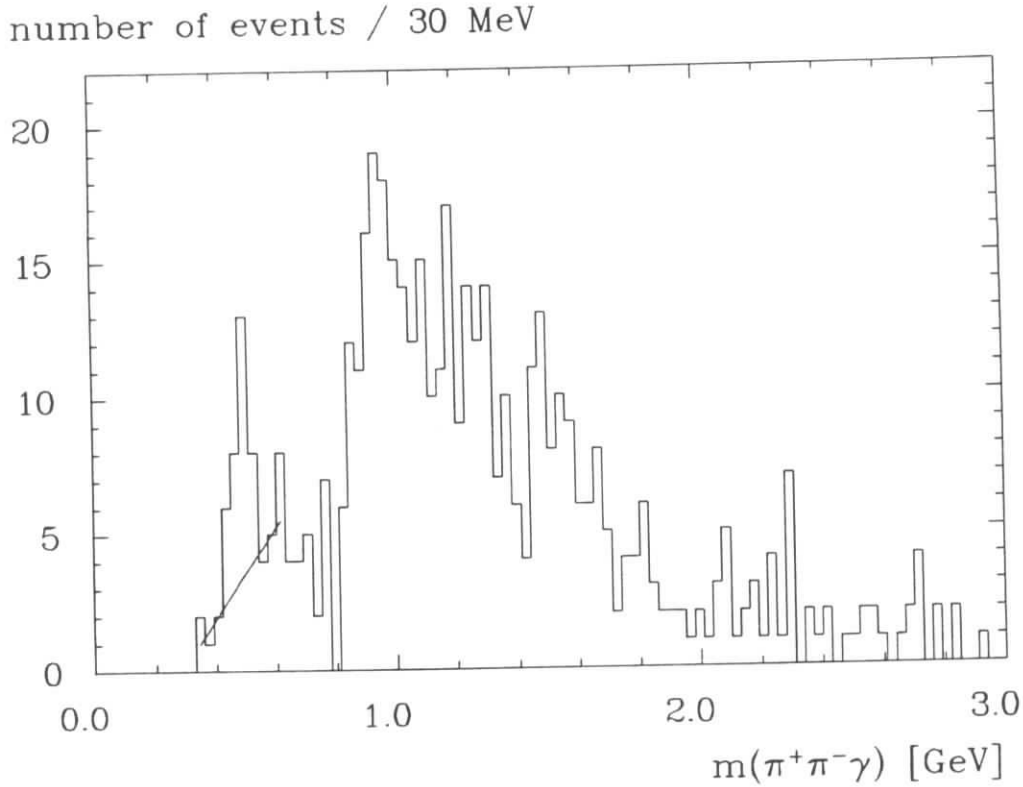


Figure 8.3: Invariant $\pi^+\pi^-\gamma$ -mass spectrum after a kinematical fit and a photon energy cut of 100 MeV. The shape of the background has been estimated by a straight line.

left hand side of the spectrum. The bulk part of the peak is due to the decay of the η into $\pi^+\pi^-\pi^0$ as can be seen from the MC studies. Using this MC information a signal region from 420 – 540 MeV has been defined. To estimate the amount of background in this region the shape of the background is extrapolated from two sidebands (300–420 MeV and 540–660 MeV) with a straight line. From the total number of 35 events in the signal region and an estimated background of 13 events the number of η -candidates is determined to be 22.0 ± 5.9 . Due to the unknown correct shape of the background the systematic error of the background subtraction is certainly of the order of 20%.

The data events are now split into 5 Q^2 -bins for the calculation of the form factor dependence on this variable. The same Q^2 -bins are taken as in the previous analyses. The number of events in each of these bins can be found in table 8.2. To get the number of η -candidates

Q^2 [GeV]	# of data events	# of MC events	$\Gamma_{\gamma\gamma} \cdot f^2(Q^2)$ [keV]
0.3 – 0.8	6.5/9	36.1	0.180 ± 0.083
0.8 – 1.2	7.5/12	62.6	0.120 ± 0.055
1.2 – 1.7	3.5/8	67.6	0.052 ± 0.042
1.7 – 3.4	4.5/6	80.4	0.056 ± 0.030
3.4 – 20.	0/0	71.0	—

Table 8.2: Values of the form factor for the reaction $\eta \rightarrow \pi^+\pi^-\gamma$.

in each of these bins, the invariant mass spectrum is treated in the same way as for the total spectrum, i.e. a linear background shape is assumed. The number of events in the signal region with and without background subtraction is given before and after the slash, respec-

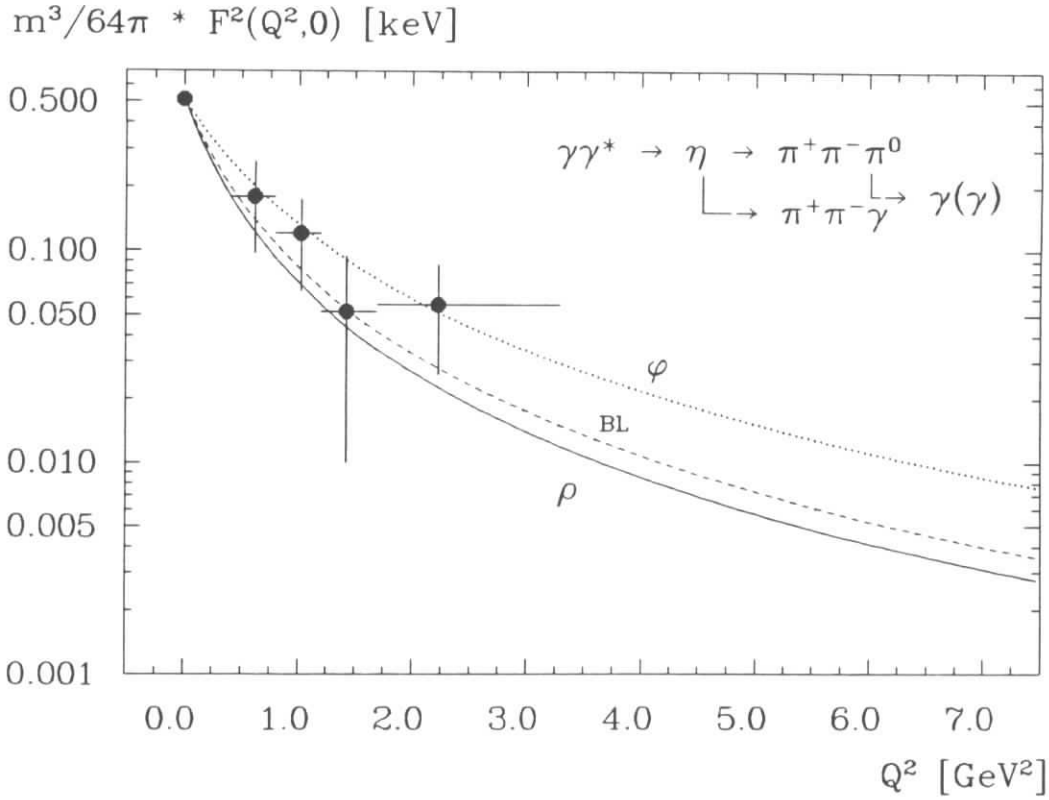


Figure 8.4: Q^2 -evolution of the η -form factor in the final state $\pi^+\pi^-\gamma$.

tively, in the above table. For the MC events the same Q^2 -bins and signal region is chosen. Due to the shifted mass spectra of the different decay modes of the η , the relative amount of the exclusive $\pi^+\pi^-\gamma$ -decay is reduced to about 10% in the signal region. The numbers given, therefore, primarily stem from the decay $\pi^+\pi^-\pi^0$. The values for the form factor times radiative width calculated from these numbers are plotted in fig. 8.4. Shown are again the expectations for this dependence normalized to a radiative width of 0.51 keV for the VDM model and QCD calculation.

8.3 Conclusions and Discussion

Since the fully reconstructed decay into $\pi^+\pi^-\pi^0$ has a very limited statistics, the combined result for the form factor measurement will entirely be dominated by the result derived in the last section. The combined number of events in the various Q^2 -bins and the resulting form factor can be read off from table 8.3. The values for the form factor are plotted in fig.

Q^2 [GeV]	# of data events	# of MC events	$\Gamma_{\gamma\gamma} \cdot f^2(Q^2)$ [keV]
0.3 – 0.8	8.5/11	47.3	0.180 ± 0.070
0.8 – 1.2	9.5/14	90.2	0.105 ± 0.055
1.2 – 1.7	4.5/9	102.2	0.044 ± 0.029
1.7 – 3.4	5.5/7	139.6	0.039 ± 0.019
3.4 – 20.	0/0	98.4	—

Table 8.3: Combined values for the η - γ -transition form factor. The number behind the slash is the total number of events in the signal region including background.

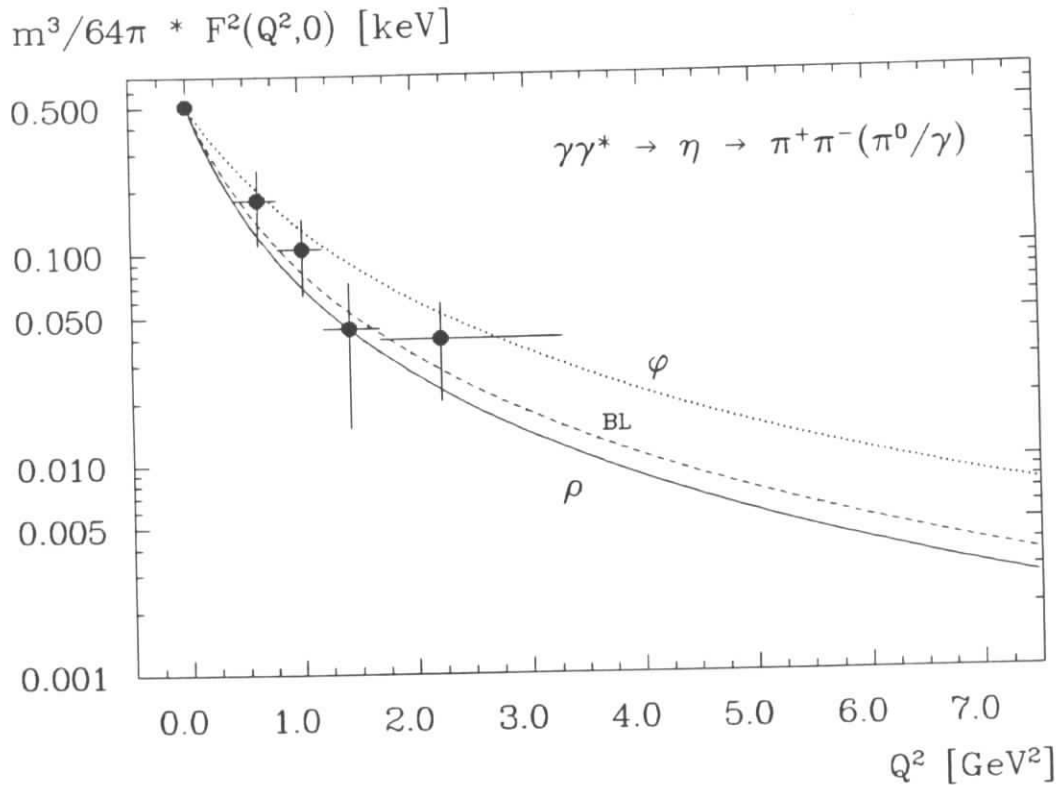


Figure 8.5: Q^2 -evolution of the η - γ -transition form factor calculated from the combined result of the $\pi^+\pi^-\pi^0$ and $\pi^+\pi^-\gamma$ -decays

8.5 with the VDM model and QCD predictions. Assuming a ρ -pole dominance for the form factor 0.6 events are expected in the end cap calorimeter region, which is compatible with the non-observation of any event in this Q^2 -range.

We have also measured the form factor in the totally neutral η -decay mode into two photons [82]. The form factor obtained in this decay mode is in good agreement with the measurements presented here and a combined result is derived from 68.6 ± 11.1 η -candidates. As for the η' a pole fit with $f(Q^2) = 1/(1 + Q^2/\Lambda_p^2)$ is performed on the combined form factor points (see fig.8.6). Again the pole mass Λ can be expressed in terms of the decay constant $2\pi f_\eta$. The fit yields a pole mass of $\Lambda_\eta = 839 \pm 63$ MeV in good agreement with a ρ -pole mass, which corresponds to $f_\eta = 133 \pm 10$ MeV.

The TPC/2 γ Collaboration [78] has performed a similar analysis as described in the last section. They study the $\pi^+\pi^-\gamma$ -final state for events with $|\cos\vartheta_\pi^*| < 0.75$ and a fitted photon energy above 100 MeV. With an integrated luminosity of 113 pb^{-1} they find 38.0 ± 9.4 η -candidates. The form factor is determined in 5 bins of Q^2 covering the region from 0.1 – 7.0 GeV^2 (see fig.8.6). The data points [79] are found to nicely follow the expected behaviour of a ρ -form factor or the QCD interpolation curve. A ϕ -form factor does not describe their data so well. Their result is compatible with our findings, although within the statistical and systematical accuracy achieved no distinction can be made between the various predictions with our data. Using the above pole form of the form factor the TPC Collaboration fitted their data and arrived at a decay constant of $f_\eta = 112 \pm 13$ MeV (or correspondingly at a pole mass of 0.70 ± 0.08 GeV).

The form factor measurements from two-photon experiments can also be compared to the results from leptonic conversion decays. Measurements of the reaction $\eta \rightarrow e^+e^-\gamma$ have so

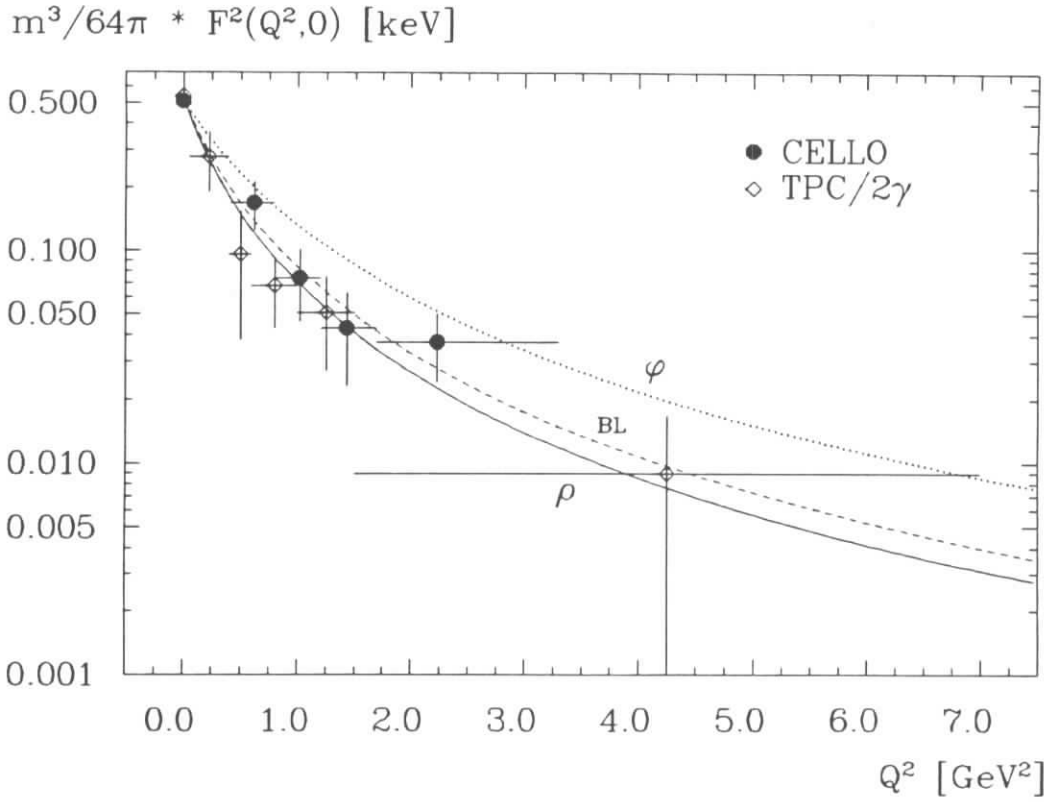


Figure 8.6: A comparison of the η - γ -transition form factor of the TPC/2 γ Collaboration with the results from CELLO calculated from the combined result of the $\gamma\gamma$ [82], $\pi^+\pi^-\pi^0$ and $\pi^+\pi^-\gamma$ -decays

far not arrived at a statistically significant result (for an overview see ref. [19]). The reaction $\eta \rightarrow \mu^+\mu^-\gamma$ has been studied by the Lepton-G experiment [83]. With 600 events of this type they determine the slope b of the form factor at $Q^2 = 0$ to be $b_\eta = 1.9 \pm 0.4 \text{ GeV}^{-2}$ which is equivalent to a pole mass of $\Lambda_\eta = 0.72 \pm 0.09 \text{ GeV}$ ($\Lambda^2 = 1/b$). All three results are in nice agreement. Averaging the three results gives a pole mass which is identical to the mass of the ρ : $0.77 \pm 0.04 \text{ GeV}$.

Chapter 9

Coupling Strength of the Spin-1 Meson $f_1(1285)$

Recently the production of spin-1 mesons in two-photon reactions has been observed by several experiments [59,63,84]. The $f_1(1285)$ (formerly called D(1285)) has been observed in its decay mode $\eta\pi\pi$, $\eta \rightarrow \gamma\gamma$ and the $f_1(1420)$ (the former E(1420)) in $K_S K\pi$. Due to the fact that two real photons cannot couple to a spin-1 state, the production of a meson like the $f_1(1285)$ or $f_1(1420)$ can only be observed in a tagged reaction. Tagged reactions occur with a much smaller rate than untagged reaction for the pseudoscalar mesons presented in this thesis. The contrary is true for spin-1 mesons. One of the most peculiar signs is the absence of a signal in the untagged mode while there is a signal in the tagged mode. This feature has been observed by all experiments, giving an unmistakable signature of the spin-1 nature of these mesons in a two-photon reaction.

While for the $f_1(1420)$ the parity of the state cannot be unanimously fixed and its assignment to the axial vector meson nonet is questionable, no such doubts exist for the $f_1(1285)$. The state is well established and its decay modes are known to be roughly 90% $\eta\pi\pi$ and 4% with the rest decaying into $K\bar{K}\pi$. From this it can be deduced that this meson primarily consists of u and d quarks. The first observation of this state in a two-photon reaction decaying into $\eta\pi^+\pi^-$ was reported by the MarkII Collaboration in 1987 [59]. This observation soon was confirmed by the TPC/2 γ Collaboration [84] in the same decay mode. JADE [63] and CELLO [3,85] reported preliminary results on its coupling strength. The number of events observed by each of the collaborations is quite small. With an integrated luminosity of 140 pb^{-1} the TPC/2 γ Collaboration found 26 f_1 -candidates, MarkII found 24 candidates in 220 pb^{-1} and JADE roughly 40 in 214 pb^{-1} . The expected number of $f_1(1285)$ -candidates in the CELLO data is even smaller due to the lower integrated luminosity of only 86 pb^{-1} .

In this chapter the determination of the coupling strength of this meson to two photons will be presented. Since the radiative width $\Gamma_{\gamma\gamma}$ is equal to zero for a spin-1 meson at $Q^2 = 0$, the result will be expressed in terms of the Q^2 -independent coupling strength $\tilde{\Gamma}$ defined by equation 2.43. The measurement itself is conducted in the single tag mode where one of the photons is almost real and the other one has a virtual mass substantially deviating from zero. This latter photon can be polarized either transversely or longitudinally, leading to two independent coupling strengths with different Q^2 -dependencies. Using the model of Cahn (see section 2.4.2) the two corresponding cross sections σ_{TT} and σ_{LT} are related by the simple expression $Q^2/2W^2$ and hence can be expressed in terms of the same coupling constant $\tilde{\Gamma}_{\gamma\gamma}^{Cahn}$ (eqs. 2.46, 2.47).

number of entries / 40 MeV

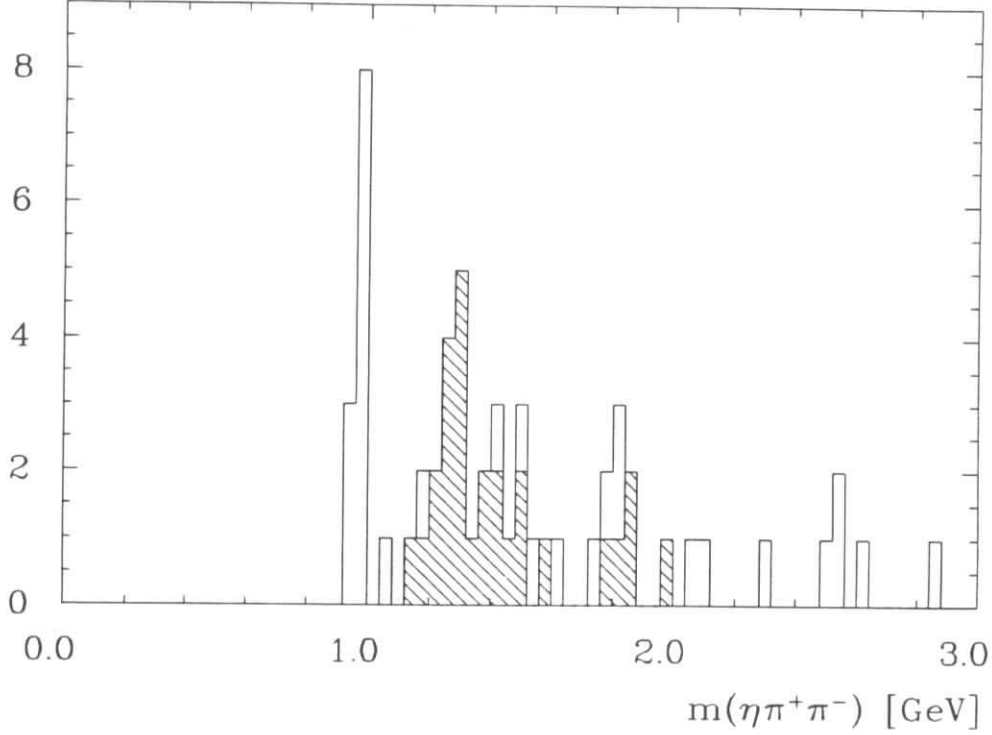


Figure 9.1: Invariant $\pi^+\pi^-\eta$ -mass spectrum after a full kinematical fit with η -mass constraint for eye-scanned events. The shaded histogram marks events with at least one $\eta\pi$ -combination in the $a_0(980)$ -band.

The selection of events for this analysis follows closely that described for the search of the η' decaying into $\eta\pi^+\pi^-$. From the 1500 events with two charged tracks, two photons and a tagged lepton only those with a measured tag energy above 5 GeV are taken. The photons are either detected in the end cap or in the barrel part of the lead liquid argon calorimeter, the tracks have to be well contained in the central part of the inner detector ($|\cos\vartheta| < 0.92$). These events are subjected to a kinematical fit requiring a balance of the overall transverse momentum. To single out the final state under study, a cut in the invariant mass spectrum of the two final state photons in the η -band (310-720 MeV) is applied. The events are then subjected to a full kinematical fit with an η -mass constraint for the final state photons.

While in the mass range of the η' no background has been observed (see figure 7.7), the amount of background is much higher in the mass range of the $f_1(1285)$. An eye-scan of the remaining events was conducted to throw out those events which evidently are no true $\pi^+\pi^-\gamma\gamma$ events. For example, events were removed containing unreconstructed tracks of very low momentum coming from the interaction region. The invariant mass distribution of the events after this scan is shown in fig.9.1.

Clearly seen is the η' -peak just below 1 GeV and a second peak between 1.24 to 1.32 GeV. The majority of the $f_1(1285)$ -decays into the $\eta\pi\pi$ -final state proceed via the intermediate $a_0(980)\pi$ -state. (The branching ratio $B(f_1(1285) \rightarrow \eta\pi\pi) = 49 \pm 6\%$ includes a contribution of $B(f_1(1285) \rightarrow a_0(980)\pi) = 36 \pm 7\%$). To see whether the second peak is consistent with this decay chain, a cut in the $\eta\pi^\pm$ -mass is applied. The shaded histogram in fig.9.1 contains those events which have at least one $\eta\pi$ -combination in the $a_0(980)$ -band (860-1100 MeV). Since all of the events in the peak remain, the peak can be identified with the $f_1(1285)$. To determine

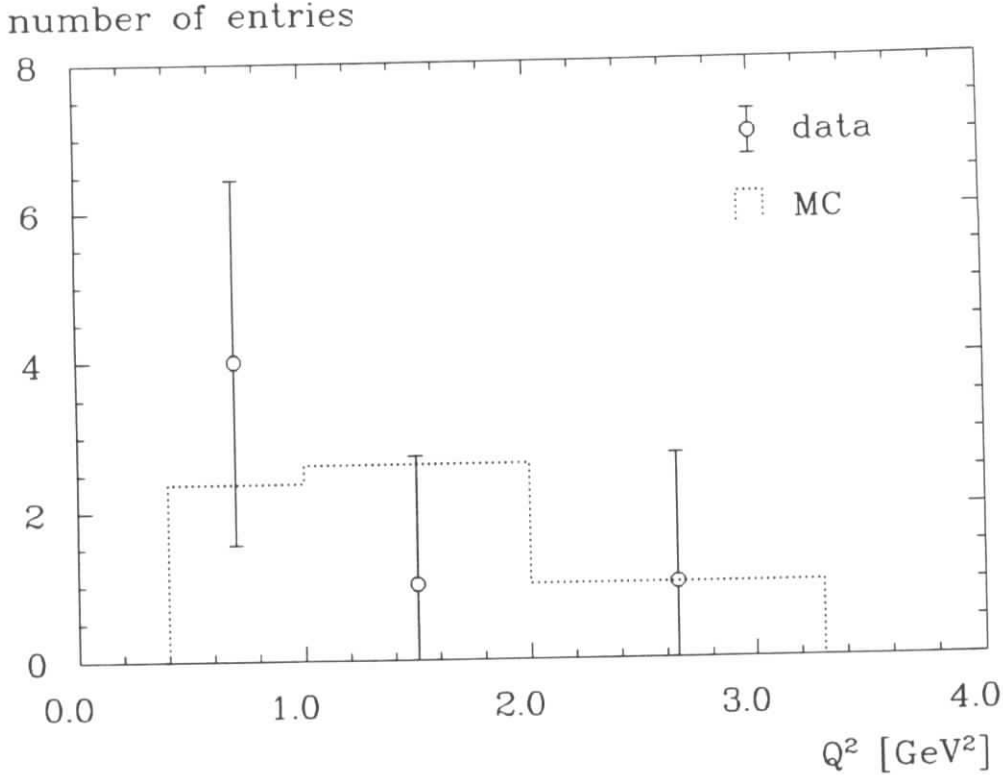


Figure 9.2: Q^2 -distribution of the $f_1(1285)$ -events in the forward calorimeter. The MC distribution (dotted) is normalized to the number of data events.

the number of $f_1(1285)$ -candidates in the spectrum, the background shape is estimated from the neighbouring bins. Depending on the number of bins used for this determination, between 6 and 9 signal events are found, yielding 7.5 ± 3.5 $f_1(1285)$ -candidates after background subtraction.

From this number the coupling strength can be calculated in the frame-work of the Cahn model. MC events have been produced according to the two cross sections σ_{TT} and σ_{LT} in the ratio predicted by this model. Due to the different Q^2 -dependencies ($\sigma_{TT} \propto Q^4$ and $\sigma_{LT} \propto Q^2$) the LT -cross section will be dominant for small values of Q^2 up to $2W^2$. Assuming a ρ -pole form factor, for every LT -event 0.36 TT -events are found in the acceptance region of the forward calorimeter, while in the end cap calorimeter region this ratio is 1:2.5 ($LT:TT$). No event with a tag in the end cap calorimeter is however observed in data, leading to a systematic uncertainty which depends on the Q^2 -region used for the evaluation of the coupling strength. If the coupling strength is determined only in the region of the forward calorimeter a value of $\bar{\Gamma} = 5.2 \pm 2.4$ keV is found, where the error is the statistical error including the effects of the background subtraction. The distribution of events in the forward calorimeter is shown in fig. 9.2. The data events are plotted with their error bars in three Q^2 -bins in the range from 0.4 to 3.3 GeV² with their error bars, while the MC events are shown as a dotted line histogram normalized to the number of data events. The overall agreement between the data points and the MC curve is found to be fair.

If instead the coupling strength is determined in the full accessible acceptance range, a value of $\bar{\Gamma} = 3.6 \pm 1.7$ keV is found, where the error has the same meaning as above. The two values can be combined to a single value, because none of the two methods is superior

to the other:

$$\tilde{\Gamma}_{\gamma\gamma}^{Cahn}(f_1(1285)) = 4.4 \pm 2.1(stat.) \pm 1.2(syst.) \text{ keV} \quad (9.1)$$

The total systematic error arises from the averaging of the two individual results including a variation of the background subtraction method (+25% and -20%), the error in the luminosity determination (3%), track (4%) and photon (8%) reconstruction efficiencies, trigger simulation (6%) and the error on the branching ratio (12%).

This result agrees within errors with the numbers found by the other collaborations: $9.4 \pm 2.5 \pm 1.7$ keV (MarkII), $4.8 \pm 1.0 \pm 1.0$ keV (TPC/2 γ) and $3.6 \pm 0.6 \pm 0.8$ keV (JADE, prelim.). The published values from TPC/2 γ and JADE have been multiplied by 2 to be in accord with the Cahn convention. The statistical average including our result gives $\tilde{\Gamma} = 4.2 \pm 0.5$ keV with and $\tilde{\Gamma} = 5.3 \pm 0.9$ keV without the preliminary JADE result.

Chapter 10

Summary

In this thesis the formation of the pseudoscalar mesons η and η' and of the axial vector meson $f_1(1285)$ has been studied in tagged and untagged two-photon reactions with the CELLO detector.

In the untagged mode the production of the pseudoscalar meson η' was studied in the $\pi^+\pi^-\gamma$ final state. The radiative width was determined to be

$$\Gamma_{\gamma\gamma}(\eta') = 3.62 \pm 0.15 \pm 0.47 \text{ keV}.$$

Using this value a world average of $\langle\Gamma_{\gamma\gamma}\rangle = 4.0 \pm 0.1 \text{ keV}$ has been calculated based on statistical errors only. The discrepancies found in the world data can mainly be attributed to too small systematical errors given by some of the low statistics experiments and to problems in the branching ratios of the totally neutral decay modes $\gamma\gamma$ and $\eta\pi^0\pi^0$ of the η' .

One major source of background in the $\pi^+\pi^-\gamma$ -final state is the incompletely reconstructed decay of the $a_2(1320)$ into $\pi^+\pi^-\pi^0$. A combined fit to the η' and a_2 mass spectrum yields a radiative width for the $a_2(1320)$ of

$$\Gamma_{\gamma\gamma}(a_2(1320)) = 0.97 \pm 0.09 \pm 0.20 \text{ keV}.$$

consistent with a previous measurement of this reaction by CELLO.

In the single tag mode the Q^2 -development of the pseudoscalar- $\gamma\gamma^*$ -transition form factor was measured. For the η' this measurement was performed in the decay modes $\eta' \rightarrow \rho\gamma$, $\eta' \rightarrow \eta_{\rightarrow\gamma\gamma}\pi^+\pi^-$ and $\eta' \rightarrow \eta_{\rightarrow\pi^+\pi^-(\pi^0/\gamma)}\pi^+\pi^-$. The Q^2 -development of the form factor is described by a pole-form $1/(1 + Q^2/\Lambda^2)$ with a mass of

$$\Lambda_{\eta'} = 0.794 \pm 0.044 \text{ GeV}$$

well in accord with other measurements in two-photon reactions and leptonic conversion decays as well as VDM-model and QCD-inspired predictions. From the Q^2 -development the radiative width of the η' can be inferred by an extrapolation to $Q^2 = 0$. The corresponding value of $3.98 \pm 0.52 \text{ keV}$ under the assumption of a ρ -pole is in good agreement with the value obtained directly from untagged events.

The corresponding measurement for the η was performed in the decay modes $\eta \rightarrow \pi^+\pi^-\pi^0$ and $\pi^+\pi^-\gamma$. Here as well the Q^2 -dependence can be described with a pole form for the form factor. The pole mass obtained by a fit is

$$\Lambda_{\eta} = 0.839 \pm 0.063 \text{ GeV}$$

compatible with a simple VDM ρ -pole and the two other measurements of this quantity in two-photon reactions and leptonic conversion decays.

The coupling of spin-1 mesons to two photons cannot be measured in the untagged mode. Their radiative width is zero at $Q^2 = 0$. Instead, a Q^2 -independent coupling strength $\tilde{\Gamma}$ can be determined in the single tag mode. This quantity was measured for the $f_1(1285)$ in the $\eta\pi^+\pi^-$ -final state to be

$$\tilde{\Gamma}_{\gamma\gamma}^{Cahn}(f_1(1285)) = 4.4 \pm 2.1 \pm 1.2 \text{ keV}$$

in the frame-work of the Cahn-model which relates the two possible independent cross sections σ_{LT} and σ_{TT} governing this process.

Bibliography

- [1] H.Euler, B.Kockel, Nat.Wiss. **23** (1935) 246
H.Euler, Ann.Phys. **26** (1936) 398
- [2] see [4,5,6] and references therein and for example
R.G.Roberts and M.R.Whalley, *Compilation of Data on $\gamma\gamma \rightarrow$ hadrons*, RAL-86-058
S.L.Cartwright, *Two-Photon Physics*, RAL-86-100
Proceedings of the VIII.International Workshop on Photon-Photon Collisions, Shoresh,
Israel, 1988, World Scientific
R.N.Cahn, *Two-Photon Physics*, LBL-28672
- [3] J.H.Peters, *Hadron Resonance Production in Two Photon Processes with the CELLO
detector*, Proceedings Intern.Symposium Hadron Interactions, Bechyně, Czechoslovakia,
1988, Ed. J.Fischer, P.Kolář, V.Kundrát
M.Feindt, DESY 88-157
M.Feindt, DESY 89-142
- [4] H.Kolanoski, *Two-Photon Physics at e^+e^- Storage Rings*, Springer Tracts in Modern
Physics, Vol.105, 1984
- [5] Ch.Berger and W.Wagner, Phys.Rep. **146** (1987) Vol 1 & 2
- [6] M.Poppe, Int.Journal of Mod.Phys. **A1** (1986) 545
- [7] V.M.Budnev et al., Phys.Rev. **15C** (1975) 181
- [8] C.F.v.Weizsäcker, Z.Phys. (1934) 612
E.Williams, Kgl. Danske Videnskab Selskap, Mat.-Fiz.Med No. 13 (1935)
- [9] C.N.Yang, Phys.Rev. **77** (1950) 242
- [10] F.E.Low, Phys.Rev. **120** (1960) 582
- [11] M.Feindt, Ph.D. thesis, University of Hamburg, Internal Report DESY-F14-88-02
- [12] M.Feindt, *A Partial Wave Analysis for Two Gamma Reactions*, in preparation
- [13] J.M.Blatt, V.Weisskopf, *Theoretical Nuclear Physics*, John Wiley, New York, 1952
(1981) 1808
- [14] R.N.Cahn, *Twos in Two Photon Physics*, Proceedings VIII. Intern.Workshop on Photon
Photon Collisions, Shoresh, Israel, 1988, World Scientific
- [15] R.N.Cahn, Phys.Rev. **D35** (1987) 3342

- [16] F.M.Renard, *Nuovo Cimento* **80A** (1984)
- [17] Particle Data Group, *Review of Particle Properties*, *Phys.Lett.* **B204** (1988)
- [18] TPC/2 γ Collaboration, H.Aihara et al., *Phys.Rev.* **D38** (1988) 1
 MarkII Collaboration, G.Gidal et al., *Phys.Rev.Lett.* **59** (1987) 2016
 JADE Collaboration, P.Hill et al., *Z.Phys.* **C42** (1989) 355
 CELLO Collaboration, H.J.Behrend et al., *Z.Phys.* **C42** (1989) 367
- [19] L.G.Landsberg, *Phys. Rep.***128**, (1985) 301
- [20] J.J.Sakurai, *Ann.Phys.***11** (1960) 1
 J.J.Sakurai and D.Schildknecht, *Phys.Lett.* **B41** (1972) 489
- [21] S.J.Brodsky and G.P.Lepage, *Phys.Rev.* **D24**
- [22] M.Feindt, private communications
- [23] K.M. Watson, *Phys.Rev.* **881** (1952) 1163
- [24] J.D. Jackson, *Nuovo Cimento* **34** (1964) 1644
- [25] S.L. Wu, DESY 84-028
- [26] see [25] and references therein
- [27] H.-J. Behrend et al., *Physica Scripta* **23** (1981) 610
 In the design and construction period groups from the following six institutes participated: Deutsches Elektronen-Synchrotron (Hamburg), Kernforschungszentrum und Universität Karlsruhe, Max-Planck-Institut für Physik und Astrophysik (München), all Germany and Laboratoire de L'Accélérateur Linéaire (Orsay), LPNHE (Paris) and Centre d'Etudes Nucléaires (Saclay) from France. Later on groups from the University of Glasgow, the II. Institut für Experimentalphysik (Universität Hamburg), Laboratoire de Physique Nucléaire et des Hautes Energies (Université de Paris), University of Rome and INFN (Rome) and from the Tel Aviv University joined.
- [28] J.Harjes, Diploma thesis, University of Hamburg, Internal Report DESY F14-87-06
- [29] B.Sack, Diploma thesis, University of Hamburg, 1984
- [30] U.Binder, Diploma thesis, University of Hamburg, 1984
- [31] H.-J.Behrend, *Comp.Phys.Comm.* **22** (1981) 365
- [32] J.Knapp, *New Liquid Argon Trigger*, CELLO note K081, 1984, unpublished
 K.Gamerding et al., *Status of the New Liquid Argon Trigger*, CELLO note K101, 1985, unpublished
- [33] K.Gamerding, H.Jung, *New Logic of the LAr FADC Trigger*, CELLO note K114, 1985, unpublished
- [34] G.Franke, *The CELLO event filter program*, CELLO note D035, 1985, unpublished
- [35] J.Ahme, Ph.D. thesis, University of Hamburg, 1988, Internal Report DESY FCE-89-01

- [36] M.Feindt, *Criteria Applied in the 1986 DST Select Job*, CELLO note D042, 1986, unpublished
- [37] M.Feindt, *MOTTE0/1 - Monte Carlo Integration for $\gamma\gamma$ -reactions (resonances and continuum) without approximations*, program description, unpublished
see also: M.Feindt, Internal Report DESY F14-88-02
- [38] M.Feindt, Diploma thesis, University of Hamburg, Internal Report DESY PLUTO 84-03
- [39] S.Kawabata, *Comp.Phys.Comm.* **41** (1986) 127
- [40] J.Friedmann, *SAGE - A General System for Monte Carlo Generation with Preferred Space Density Distributions*, SLAC Computation Group, Technical Memo 145, 1972
- [41] EGS: R.L.Ford, W.R.Nelson, SLAC-210, 1978
HETC: RISC Comp. Code Collection, Oak Ridge Nat.Lab., CCC-178
- [42] W.d.Boer, M.Iacovacci, CELLO Note R02, unpublished
S.Scholz, CELLO Note M185, unpublished
- [43] *VIOLA - A Program Package for Analysing CELLO data*, a joint effort of the DESY-F14 group, unpublished
- [44] J.H.Peters, *The $K_S^0 K_S^0$ final state in $\gamma\gamma$ Interactions*, Proceedings of the International Europhysics Conference on High Energy Physics, Uppsala, Sweden, 1987
CELLO Collaboration, H.J.Behrend et al., *Z.Phys.* **C42** (1989) 367
CELLO Collaboration, H.J.Behrend et al., *Z.Phys.* **C43** (1989) 91
- [45] M.Feindt, *CELPAT V811 program description*, unpublished
- [46] J.Ahme, M.Feindt, H.Fenner, J.Harjes and J.H.Peters *Aspects of Shower Reconstruction and Particle Identification at Low Energies in a Fine-grained Liquid Argon Calorimeter*, to be published in *Nucl.Instr.Meth.*
- [47] J.H.Peters, *REJECTEL Program description*, unpublished
- [48] V.Blobel, *LINABS, A Fit Program that Minimizes the Linear Distance of Data Points to a Straight Line*, Program description, unpublished
- [49] P.J.Bussey, private communications
- [50] MarkII Collaboration (SPEAR), G.S.Abrams et al., *Phys.Rev.Lett.* **43** (1979) 477,
P.Jenni et al., *Phys.Rev* **D27** (1983) 1037
- [51] JADE Collaboration, W.Bartel et al., *Phys.Lett.* **113B** (1982) 190
- [52] CELLO Collaboration, H.J.Behrend et al., *Phys.Lett.* **114B** (1982) 378,
Phys.Lett. **125B** (1983) 518 (E)
- [53] PLUTO Collaboration, Ch.Berger et al., *Phys.Lett.* **142B** (1984) 125
- [54] TASSO Collaboration, M.Althoff et al., *Phys.Lett.* **147B** (1984) 487

- [55] JADE Collaboration, W.Bartel et al., Phys.Lett. **160B** (1985) 421
- [56] TPC/ 2γ Collaboration, H.Aihara et al., Phys.Rev. **D35** (1987) 2650
- [57] MD-1 Collaboration, A.E.Blinov et al., Inst. for Nuclear Physics, Nowosibirsk, Preprint 87-92
- [58] ARGUS Collaboration, H.Albrecht et al., Phys.Lett. **199B** (1987) 457
- [59] MarkII Collaboration, G.Gidal et al., Phys.Rev.Lett. **59** (1987) 2012
- [60] Crystal Ball Collaboration, D.Antreasyan et al., Phys.Rev. **D36** (1988) 2633
- [61] TPC/ 2γ Collaboration, H.Aihara et al., Phys.Rev. **D38** (1988) 1
- [62] Crystal Ball Collaboration, D.Williams et al., Phys.Rev. **D38** (1988) 1365
- [63] J.Olsson, Proceedings VIII. Intern.Workshop on Photon Photon Collisions, Shoresh, Israel, 1988, World Scientific
- [64] N.A.Roe, Ph.D. thesis, SLAC-338
ASP Collaboration, N.A.Roe et al., Phys.Rev. **D41** (1990) 17
- [65] R.N.Cahn, Proceedings XIV Intern. Symposium Lepton and Photon Interactions, Stanford, USA, 1989 ,(Lawrence Berkeley Laboratory Preprint LBL-28672)
G.Gidal, MarkII Collaboration, private communications
F.Butler, Ph.D. thesis, LBL-26465(rev.)
- [66] G.Gidal, private communications
- [67] F.Butler, Ph.D. thesis, LBL-26465
- [68] B.v.Uitert, Ph.D. thesis, University of Utrecht, RX-1140
- [69] K.H.Karch, private communications
- [70] J.A.M.Vermaseren, Nucl.Phys. **B229** (1983) 347
- [71] G.Bonneau, M.Gourdin and F.Martin, Nucl.Phys. **B54** (1973) 573
- [72] J.Field, Nucl.Phys. **B168** (1980) 477, Nucl.Phys. **B176** (1980) 545 (E)
- [73] S.J.Yellin, Proceedings VIII. Intern.Workshop on Photon Photon Collisions, Shoresh, Israel, 1988, World Scientific
- [74] CELLO Collaboration, H.J.Behrend et al., Z.Phys. **C46** (1990) 583
- [75] GAMS Collaboration, D.Alde et al., Z.Phys. **C36** (1987) 603
- [76] Crystal Ball Collaboration, K.H.Karch et al., DESY 90-068, to be published in Phys.Lett.B
- [77] S.J.Lumsdon, private communications
- [78] TPC/ 2γ Collaboration, H.Aihara et al., Phys.Rev.Lett. **64** (1990) 172

- [79] D.Bauer, TPC/ 2γ Collaboration, private communications
- [80] Lepton-G Collaboration, R.I.Dzhelyadin et al., Phys.Lett. **88B** (1979) 379
and ref.[6] in [19]
- [81] references [64,62] and
Crystal Ball Collaboration, A.Weinstein et al., Phys.Rev. **D28** (1983) 2896
JADE Collaboration, W.Bartel et al., Phys.Lett. **160B** (1985) 421
TPC/ 2γ Collaboration, H.Aihara et al., Phys.Rev. **D33** (1986) 844
- [82] P.Bussey, J.H.Peters et al., *A Measurement of the π^0 , η and η' Electromagnetic Form Factors*, CELLO Collaboration, Contributed Paper to the 25th. Intern. Conference on High Energy Physics, Singapore 1990
- [83] Lepton-G Collaboration, R.I.Dzhelyadin et al., Phys.Lett. **94B** (1980) 548
- [84] TPC/ 2γ Collaboration, H.Aihara et al., Phys.Lett. **209B** (1988) 107
TPC/ 2γ Collaboration, H.Aihara et al., Phys.Rev. **D38** (1988) 1
- [85] J.Ahme, Proceedings VIII. Intern.Workshop on Photon Photon Collisions, Shresh, Israel, 1988, World Scientific

Acknowledgement

This thesis is based upon data taken with the CELLO detector at DESY. I thank all members of the collaboration for the exiting atmosphere of a running experiment and the subsequent time of analysing the data. I am grateful to my professor Hartwig Spitzer who gave me all the freedom necessary to perform the scientific enterprise which resulted in this thesis. I am especially thankful that his financial aid enabled me to visit so many conferences and workshops where I could learn about two-photon physics and talk about the work done in our group.

This work would not have been possible without the common effort of the Hamburg based two-photon physics group of CELLO, writing a totally new analysis program package VIOLA. Here, I want to mention Johannes Ahme, Michael Feindt, Hartmut Fenner and Jens Harjes, whom I worked with over all the years, constantly improving our package upto its final version in 1989.

I especially thank Michael Feindt who, with his excellent knowledge of two-photon physics, was an inexhaustable source for all my questions. I would also like to mention Arie Beck and Aharon Levy from Tel Aviv who aroused my curiosity about the η' radiative width, and Peter Bussey from our Glasgow group whom I collaborated with on the subject of pseudoscalar form factors. Last but not least I want to express my thanks to Simon Lumsdon who read through my manuscript with the careful eye of a native speaker.

